Molecular Probes in Highly Irradiated Gas

Non-thermal rotational and vibrational emission in energetic environments

by

Ziwei E Zhang

(Under the Direction of Phillip C. Stancil)

Abstract

Observations and analysis of molecular emission have long provided valuable insights into the interstellar medium (ISM). Hot (highly excited) molecules are commonly observed in intense UV-irradiated regions, e.g., photodissociation regions (PDRs), circumstellar envelopes (CSEs), and surface layers of protoplanetary disks (PPDs). The excitation properties of molecules directly reveal the physical conditions of the gas and thus are unique probes of these energetic environments. Particularly, low-density environments with intense UV radiation may be in non-local thermal equilibrium (NLTE), in which high excitation molecular analysis is especially of interest. For such studies, a quantitative understanding of microprocesses (e.g., collisional rate coefficients of molecular excitation, radiative transfer, etc.) is needed, while being previously limited. In this thesis, I discuss NLTE simulations of high excitation molecular emission in UV-pumped gas with state-of-the-art theoretical calculations and simulation techniques. Furthermore, a few applications of this simulation approach in realistic astrophysical environments, e.g., PDRs and circumstellar envelopes, are highlighted. This work is essential to the interpretation of highly (rotationally and vibrationally) excited molecular emission from high-resolution observational data (e.g., Spitzer, Herschel, SOFIA,

ALMA, and soon from JWST), as well as opening up the near- to mid-infrared window for NLTE molecular analysis.

INDEX WORDS: ISM: molecules, photodissociation region (PDR), molecular data, stars: AGB and post-AGB

Molecular Probes in Highly Irradiated Gas

Non-thermal rotational and vibrational emission in energetic environments

by

Ziwei E Zhang

B.S., Northeast Normal University, Changchun Jilin, 2011

A Dissertation Submitted to the Graduate Faculty

of The University of Georgia in Partial Fulfillment

of the

Requirements for the Degree

Doctor of Philosophy

Athens, Georgia

2019

© 2019

Ziwei E Zhang

All Rights Reserved

Molecular Probes in Highly Irradiated Gas

Non-thermal rotational and vibrational emission in energetic environments

by

Ziwei E Zhang

Approved:

Major Professor: Phillip C. Stancil

Committee: Loris Magnani
Inseok Song

Electronic Version Approved:

Suzanne Barbour
Dean of the Graduate School
The University of Georgia
August 2019

Acknowledgments

I hereby acknowledge the help and contribution from my colleagues and collaborators. Particularly, I would like to give special thanks to my advisor, Phillip Stancil, and group members (Renata Cumbee, Yier Wan, Kyle Walker, Sally Cummings, Benhui Yang, to name a few). This group has been the lighthouse and harbor of my research journey. Additionally, I would like to thank Gary Ferland and Peter van Hoof for valuable discussions.

I would also like to thank my family and friends for their love and support. My parents, Xiurong Xu and Da Zhang, have always given me strength and confidence.

This work was partially supported by Hubble Space Telescope grant HST-AR-13899.001-A, NASA grants NNX12AF42G, NNX15AI61G and NNX16AF09G. Softwares utilized: RADEX (van der Tak et al. 2007) and Cloudy (Ferland et al. 2017).

Table of Contents

Page

Acknowledgments iv

List of Tables vii

List of Figures viii

Chapter

1 Introduction and Literature Review 2

1.1 Molecular Astrophysics 2

1.2 Highly UV-irradiated astrophysical environments 3

1.3 Physical Models 7

1.4 Contents of this thesis 12

2 Ro-vibrational analysis of SiO in UV-irradiated Environments . 14

2.1 Introduction 15

2.2 Rovibrational SiO Data Construction 17

2.3 NLTE modelling 22

2.4 Conclusion 41

3 Revisiting Non-Local Thermodynamic Equilibrium Rovibrational Excitation of CO in UV Irradiated Environments 43

3.1 Introduction 44

3.2 Data Construction 45

3.3 Modelling of astrophysical environments 49

3.4 Summary and Discussion 70

4 Properties of Highly Rotationally Excited H_2 in Photodissociation Regions . . . 72
4.1 Introduction . . . 73
4.2 H_2 Collisional Data . . . 73
4.3 Uniform NLTE Simulation . . . 76
4.4 H_2 Excitation in PDRs . . . 80
4.5 Summary . . . 86
5 Conclusion and Outlook . . . 87
5.1 Conclusion . . . 87
5.2 Outlook . . . 89
Bibliography . . . 91

List of Tables

1.1 Uniform Environment Modelling Parameters. 10

1.2 Physical parameters for Cloudy Leiden PDR benchmark models.[a] 10

2.1 Rovibrational SiO Data Summary. 18

2.2 Intense SiO Lines in Leiden PDR Model Continuum. 29

2.3 Parameters for NLTE VY CMa Model.[a] 36

3.1 CO collisional rate coefficient data. 46

3.2 Parameters for NLTE IRC +10216 Model.[a] 66

4.1 H_2 LAMDA data. 74

4.2 H_2 - H_2 rotational data update in Cloudy ($v = 0$). 74

4.3 PDR Density - Radiation Grids. [a] 81

4.4 Best-fit Cloudy Model Parameters from Kaplan et al. (2017). 84

List of Figures

1.1 Highly UV-irradiated Astrophysical Environments. 6

1.2 General PDR Structure. 7

1.3 LTE vs. NLTE. 11

2.1 SiO Data Comparison A. 19

2.2 SiO Data Comparison B. 20

2.3 SiO Einstein A Coefficients 21

2.4 SiO Diagnostic Line Ratios A 24

2.5 SiO Diagnostic Line Ratios B 25

2.6 SiO Full Rovibrational Spectrum 26

2.7 SiO Rotational Spectrum 26

2.8 SiO Fundamental Band 27

2.9 Full SiO Line Spectrum for Leiden PDR Models. 30

2.10 SiO Rotational Diagram for Leiden PDR Models. 31

2.11 Continuum Spectra for Leiden PDR F models with SiO Emission. 32

2.12 Continuum Spectra for Leiden PDR V models with SiO Emission. 33

2.13 SED of VY CMa. 37

2.14 SiO Rotation Diagram for VY CMa. 38

2.15 Species Abundances in VY CMa 39

2.16 SLED for VY CMa. 40

3.1 CO Full Line Spectra Comparison. 47

3.2 CO Excitation Comparison (Data update). 48

3.3 CO Full Rovibrational Line Spectra. 50

3.4 CO-H Rovibrational Line Spectrum. 50

3.5 CO Diagnostic Line Ratios A 51
3.6 CO Diagnostic Line Ratios B 52
3.7 PDR Continuum Spectra and CO Emission. 55
3.8 CO Rotation Diagram for Cloudy Leiden PDR models. 56
3.9 PDR Temperature - Radiation Grid Rotation Diagrams. 59
3.10 PDR Density - Radiation Grid Rotation Diagrams. 60
3.11 PDR Temperature - Radiation Grid Diagnostic Line Ratios A. 61
3.12 PDR Temperature - Radiation Grid Diagnostic Line Ratios B. 62
3.13 PDR Density - Radiation Grid Diagnostic Line Ratios. 63
3.14 Continuum Spectrum for IRC +10216. 67
3.15 Zoomed-in view for molecular emission in IRC +10216. 68
3.16 CO Rotation Diagram for IRC +10216. 69
4.1 Full Rovibrational Line Spectra of H_2 75
4.2 Rotation Diagrams for H_2 in the Vibrational Ground State ($v = 0$). 77
4.3 Zoomed-in Rovibrational Line Spectra of H_2. 78
4.4 H_2 Diagnostic Line Ratios. 79
4.5 The Effect of High Rotational H_2 - H_2 Collision Data Update. 82
4.6 Orion Bar Figures. 85

"To see a world in a grain of sand

And a heaven in a wild flower

Hold infinity in the palm of your hand

And eternity in an hour"

- William Blake, *Auguries of Innocence*

"寄蜉蝣于天地

渺沧海之一粟

哀吾生之须臾

羡长江之无穷"

- 苏轼, 赤壁赋

Chapter 1

Introduction and Literature Review

1.1 Molecular Astrophysics

It was not long ago that our knowledge of the interstellar medium (ISM) was limited to simple atomic species. Along with the development of observational astronomy since the 1930s, we have been able to detect various chemicals in space, from molecules to dust grains, starting a new chapter in astrophysics. Molecular astrophysics is mainly concerned with the study of emission or absorption by molecules. Since the 1960s, numerous molecular rotational transitions have been detected with ground-based submillimeter and millimeter telescopes. More comprehensive molecular astrophysical studies have grown exceedingly after space-based observatories (such as ISO, Spitzer, Herschel, and SOFIA) opened up the infrared window (Tielens 2005, 2013). These observations provided us valuable information about the physics and chemistry in astrophysical environments, varying from cold interstellar gas to the extremely energetic gas around active galactic nuclei (AGNs).

There are more than 200 known interstellar molecules (including isotopologues), ranging from small molecules (such as H_2 and CO) to large ones (such as polycyclic aromatic hydrocarbon, i.e., PAHs). These molecules have large numbers of observable transitions that provide important physical (e.g., collisional excitation), chemical (e.g., formation and destruction), and dynamical (e.g., hydrodynamics) information of the gas.

Particularly, taking advantage of modern observational techniques (e.g., ALMA and soon-to-be-launched JWST), we are able to use molecules to study micro-processes in the ISM, which is the ideal laboratory for molecular physics. These studies investigate the specific interactions, such as ionization and collision, between micro-species. The resulting emission

unveil the physical and chemical structures and processes for complex astrophysical objects, such as star-forming regions and circumstellar envelopes, thus furthering our understanding of the key astrophysical events within.

Such developments also lead to the establishment of new branches of astronomy, including astrochemistry (focusing on chemical reactions) and astrobiology (focusing on water and organic chemistry).

1.2 Highly UV-irradiated astrophysical environments

In many astrophysical environments, gas is highly irradiated, hence molecules are highly excited both rotationally and vibrationally. Radiatively pumped molecules cascade down, resulting in emission that cover a wide multi-wavelength band. Observations of these emission were instrumentally limited to a few rotational transitions at radio. With the recent developments in observation in the infrared and submillimeter, we are able to have a more detailed view of such sites of interest, e.g., photodissociation regions (PDRs), circumstellar envelopes (CSEs) of evolved stars, protoplanetary disks (PPDs), and planetary nebulae (PNe). (Examples shown in Figure 1.1.) JWST will especially enable us to detect the near- and mid-infrared emission from warm molecules, which motivates the investigation of molecular vibrational excitation (0.6-10 μm).

1.2.1 Photodissociation Regions

A photodissociation region (PDR), or photon-dominated region, is the interface between an H II region and a cold molecular region, where gas is mostly neutral but the chemical and physical processes are driven by far UV (FUV) radiation ($\sim$ 8 eV $< h\nu <$ $\sim$ 13.6 eV) (Hollenbach & Tielens 1999). These regions dominate the infrared and submillimeter emission of the galaxy, and show important characterizing features for the ISM. Today, the definition of a PDR has been broadened to most of the atomic and molecular interstellar gas,

where FUV plays an important role in regulating the physics and chemistry (Hollenbach & Tielens 1997; Röllig et al. 2007).

The increasing interest of PDRs revolves around star formation regions, circumstellar envelopes and outflows, PPDs and other UV irradiated environments, extending to more diverse and complex objects and regions. Laboratory astrophysicists hold great curiosity on PDRs, as they are ideal to study the interaction between FUV radiation and neutral gas. Figure 1.2 is a demonstration of the general PDR structure adapted from Hollenbach & Tielens (1999), including hydrogen, carbon and silicon species (molecules form orderly from the UV source depending on their dissociation mechanism and energy). CO and SiO are the main gas-phase carriers of carbon and silicon in PDRs, therefore are important indicators of elemental abundances. While H_2 is the main infrared molecular emitter. Observations of multiple molecular species could help reveal the detailed physical structure of the cloud. As the UV flux penetrates the gas, molecules are excited both rotationally and vibrationally. Hence, multi-wavelength observation of multiple transitions, from infrared to radio, of particular abundant molecules (such as H_2 and CO) could unfold the layered structure of the PDR and unveil the on-going micro-processes.

1.2.2 Evolved Stars

Evolved stars, namely asymptotic giant branch (AGB) stars here, are of great interest on the end of the stellar life-cycle, considering they are one of the main stellar producers of interstellar dust and gas. Generally, they have low to intermediate initial masses ($\sim 0.5 - 8$ $M_\odot$, mass limit could vary depending on definition specifics) and contribute largely to infrared emission in the galaxy. (See more in Tielens (2005); Matsuura et al. (2013); Höfner & Olofsson (2018); De Beck et al. (2019).)

The study of AGB stars is important for understanding dust composition and evolution in general, as well as chemistry related to grains. CSEs around evolved stars are complex in both composition and structure, while are also experiencing on-going pulsations, shocks,

and induced vigorous chemistry. The primary chemistry in AGB CSEs is determined by the C/O abundance ratio, namely O-rich (C/O $<$ 1, M-type), C-rich (C/O $>$ 1, carbon stars), and S-type (C/O $\sim$ 1). AGB CSEs are also one of the major astrophysical molecular repositories, ranging from diatomics to large complex hydrocarbon molecules. For instance, SiO and vibrationally excited CO are shock tracers, revealing the physical information of the shocked materials, such as temperature and density (Wong et al. 2016; Khouri et al. 2016). Multi-wavelength CO emission provide reliable constraints of gas mass-loss rate for AGB stars (De Beck et al. 2010; Khouri et al. 2016; Ramos-Medina et al. 2018; Khouri et al. 2018). Hydrocarbon molecules, such as C_2H_4 and C_2H_2, are also commonly observed at the mid-infrared and are used to study the inner zone of the envelope where intense stellar radiation sets off exceptionally active chemistry (Fonfría et al. 2008; Fonfría et al. 2017).

One of the goals of this thesis is to help fill the theoretical near- to mid-infrared gap of AGB star studies with high rovibrational molecular excitations, preparing us for future observation missions (such as JWST and SPICA).

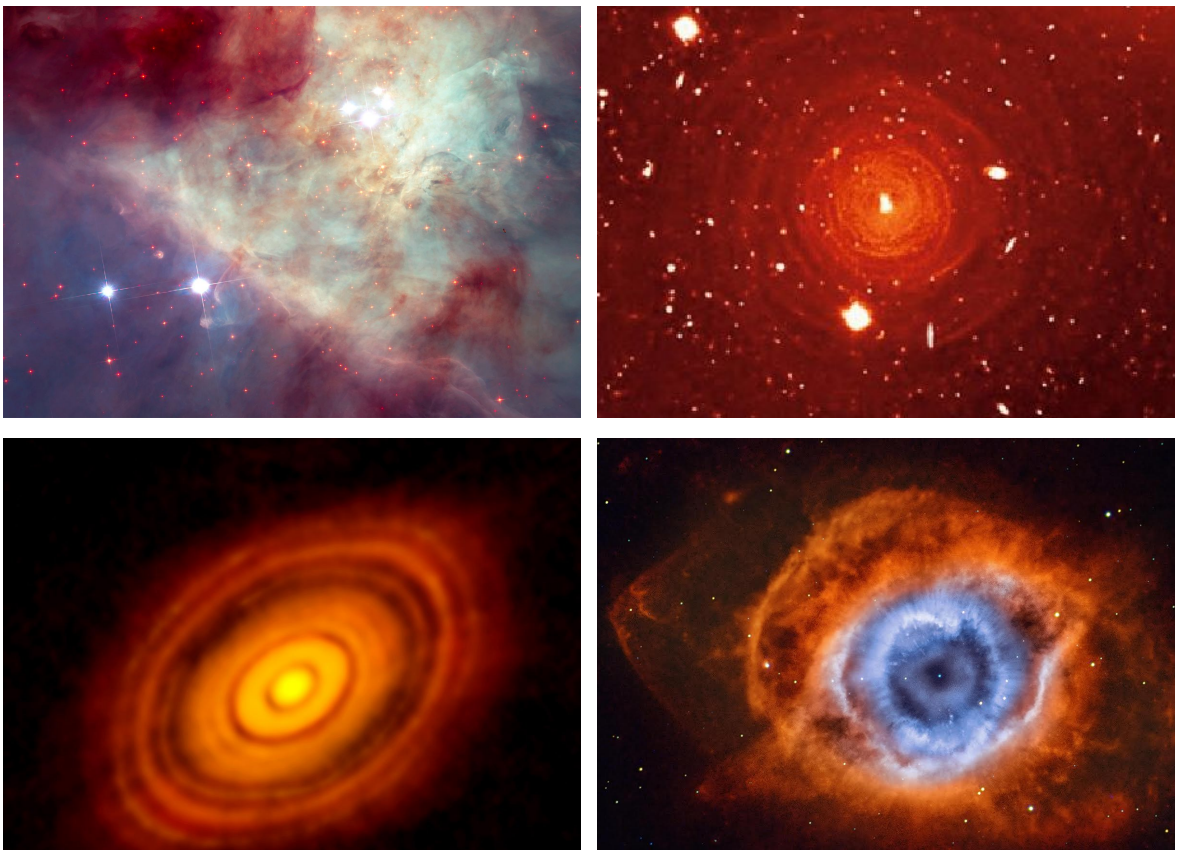

Figure 1.1: Highly UV-irradiated Astrophysical Environments.

Examples of highly irradiated astrophysical environments, including PDRs (Hubble image of the Orion Bar [a], evolved stars (VLT image of carbon star IRC +10216 from Leão et al. (2006)), PPDs (ALMA image of HL Tau [b]), and PNe (image of Helix Nebula [c]).

[a] NASA, ESA, K. Luhman (Penn State University), and M. Robberto (STScI)
[b] ALMA (NRAO/ESO/NAOJ); C. Brogan, B. Saxton (NRAO/AUI/NSF)
[c] Andrew Campbell, APOD

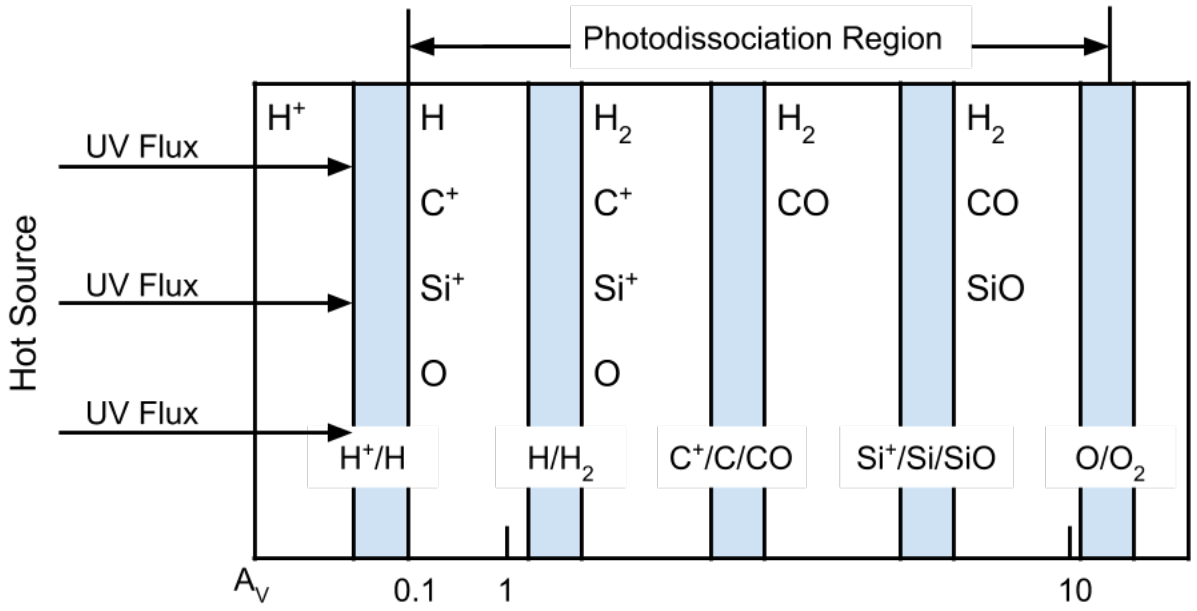

Figure 1.2: General PDR Structure.

General PDR structure modified from Hollenbach & Tielens (1999). Hot source on the left irradiates the PDR with UV radiation. CO and SiO are the main gas-phase carriers of carbon and silicon, while H_2 is the main infrared molecular emitter.

1.3 Physical Models

1.3.1 Non-Local thermal equilibrium simulations

Molecular excitation provides important probes for understanding the physical and chemical conditions of the ISM. Traditionally, the gas is considered to be in Local Thermal Equilibrium (LTE). The population for each rovibrational level is given by a Boltzmann distribution (e.g., Goldsmith & Langer (1999)),

$$N_u = \frac{N}{Z} g_u e^{-E_u/kT}, \tag{1.1}$$

which leads to the following:

$$\ln\left(\frac{N_u}{g_u}\right) \propto -\frac{E_u}{kT}, \tag{1.2}$$

where N is the total column density, Z is the rotational and vibrational partition function, g_u the statistical weight ($g_u = 2J + 1$), E_u the level energy, k the Boltzmann constant, and T the kinetic temperature. Plots for relationship between N_u and E_u, the so called rotation diagrams or population diagrams, are useful to evaluate the molecular excitation and the kinetic temperature of the cloud.

Figure 1.3 is a set of H_2 rotation diagrams at 2000 K, with varying densities (models simulated with rovibrational collisional rates up to $v = 14$). From Equation 1.2, one can deduce that a linear trend will be formed in LTE rotation diagrams (kinetic temperature equals to excitation temperature), shown in green with density of 10^{10} cm^{-3}. This often holds for sufficiently large density, in which molecular excitation is thermalized and collisionally dominated. With limited observation data, total density and kinetic temperature could be approximated with this method (e.g., LTE assumption is used to analyze the observational results of star-forming region OMC-1 in Blake et al. (1987)).

However, most astrophysical environments (such as gas with low density and high radiation) are in non-LTE (NLTE) and their molecular rotation diagrams present complex structures with multiple temperature components (low density cases in red and yellow in Figure 1.3). To accurately assess molecular excitations in these environments, we need to take consideration of all relevant transitions and the individual level populations need to be evaluated. Theoretical NLTE studies require atomic and molecular data, such as excitation energies, collisional rate coefficients and Einstein A values (van Dishoeck 2017), for a large range of levels. Currently, spectral analyses are limited to lower rotational states for most molecules (Schöier et al. 2005), due to the lack of experimental and computational data. Effort has been made to calculate and extrapolate collisional rate coefficients to include higher rotational and vibrational states for molecules such as CO and HCN in various environments (Neufeld 2012; Bruderer et al. 2015). In this thesis, we focus on the high excitation NLTE

simulation of SiO, CO and H_2, with updated collisional rates from new quantum calculations and scaling methods.

1.3.2 NLTE Astrophysical Modelling

In this work, we utilize RADEX (van der Tak et al. 2007) and Cloudy (Ferland et al. 2017) to analyze molecular properties in warm astrophysical environments. Both codes solve for NLTE level populations and work with molecular collision data in the LAMDA database (Schöier et al. 2005).

RADEX is a NLTE spectral simulation package that calculates atomic and molecular emission for a uniform cloud, while including radiative and collisional processes. Given excitation data for relevant molecular species, it could be utilized to analyze molecular excitation properties (including emission) of a homogeneous medium, considering one molecule at a time. The NLTE approach also provides physical constraints (such as density and kinetic temperature) of the gas. For the high excitation molecular analysis with RADEX in the following chapters, we take the assumptions in Table 1.1 (if not otherwise stated). Such settings would keep the models within the simulation limits (for instance, $-0.1 \lesssim \tau$ (optical depth) $\lesssim 100$), so that the spectral predictions will be reliable.

Cloudy is a spectral synthesis package designed to solve for a wide variety of conditions in complex astrophysical environments, including radiative transfer effects (such as line trapping and pumping), with state-of-the-art atomic and molecular physics. It has an extensive data system, including the LAMDA, Chianti (Del Zanna et al. 2015) and Stout (Lykins et al. 2015) databases, which are continuously updated, for modelling emission and cooling from atoms, molecules, and ions. It self-consistently solves for species abundances, ionization balance, and thermal balance, while including effects due to the interstellar dust grains.

For PDR modelling with Cloudy in the following chapters, our model parameters are based on Leiden benchmark models (Röllig et al. 2007). These models are well-established for PDR simulations and give a range of associated representative physical and chemical

conditions. The two sets of benchmark models cover a range of density and FUV field, with plane-parallel geometry (isothermal) and different treatments of PAHs. In F models (F for “fixed"), gas and dust temperatures are set constant, thus the local thermal balance is neglected. While in V models (V for “variable"), temperature is obtained by solving for the thermal balance. Table 1.2 lists key distinguishable parameters for the two sets of Cloudy PDR models. More information regarding chemistry networks and mechanisms could be found in Ferland et al. (2017).

Table 1.1: Uniform Environment Modelling Parameters.

Parameter	Value
Column Density (cm^{-2})	10^{12} (optically thin)
Cosmic Microwave background	2.73 K ($z = 0$)
Collision Partner	$H_2/H = 1$ $H/He = 10$ ortho-H_2/para-$H_2 = 3$
Geometry	Uniform Spherical (Isothermal)
Turbulent Line Width (km/s)	1.0

Table 1.2: Physical parameters for Cloudy Leiden PDR benchmark models.[a]

Model	Geometry	n (cm^{-3}) (Density)	T_{gas} (K)	T_{grain} (K)	PAH	χ [b] (FUV Field)
f1	semi-infinite,	10^3	50	20	No	10
f2	plane-parallel	10^3				10^5
f3		$10^{5.5}$				10
f4		$10^{5.5}$				10^5
v1	semi-infinite,	10^3	Variable,	Variable,	Yes	10
v2	plane-parallel	10^3	Self-consistent	Self-consistent		10^5
v3		$10^{5.5}$				10
v4		$10^{5.5}$				10^5

[a] For more details, see Röllig et al. (2007) and Ferland et al. (2017)
[b] In units of FUV Draine field, $\chi = 1.71G_0$, where $G_0 = 1$ is a Habing (Draine 1978), (Habing 1968).

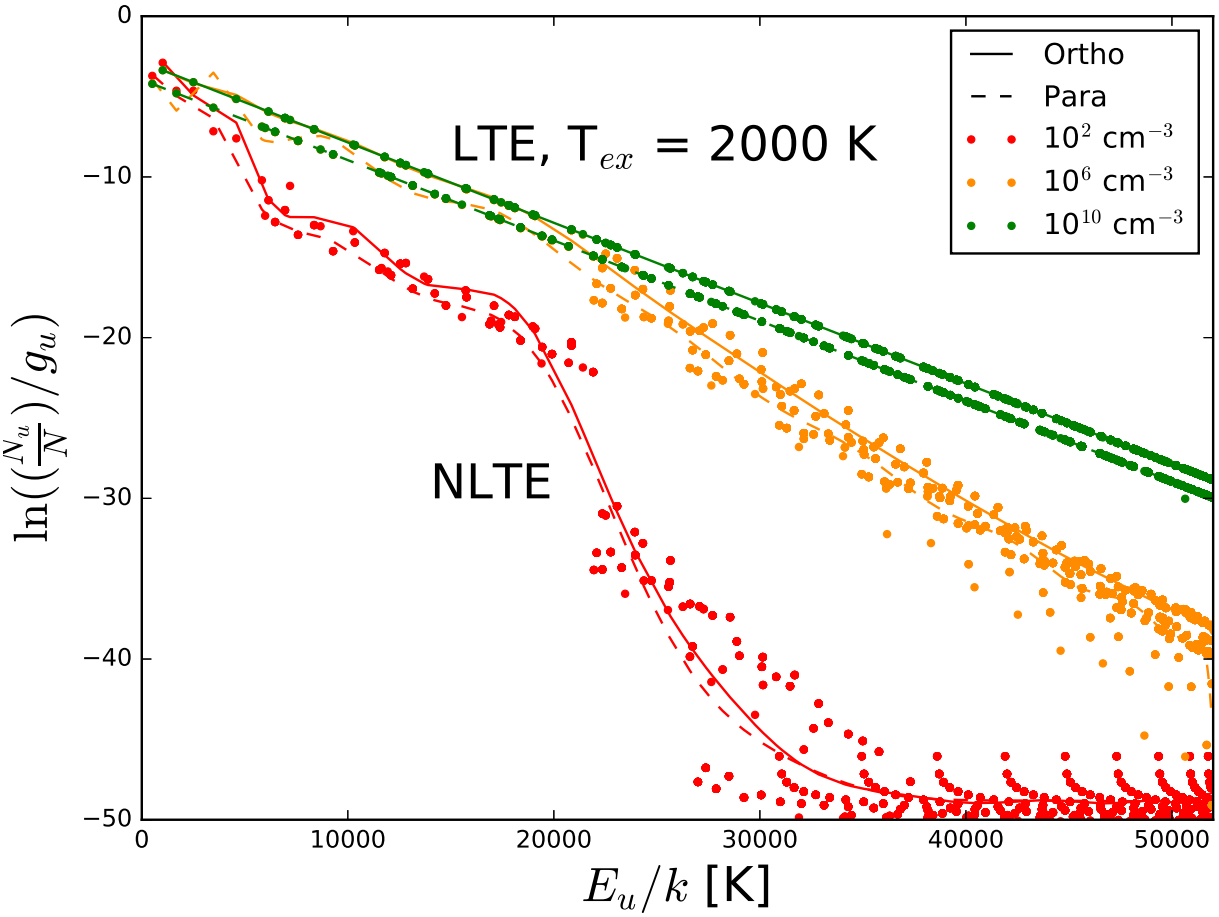

Figure 1.3: LTE vs. NLTE.

H_2 rotational diagram at 2000 K (models simulated with rovibrational collisional rates up to $v = 14$), with varying densities.

1.4 Contents of this thesis

This work focuses on NLTE spectral simulations of hot (highly excited) molecules in intense UV-irradiated regions, with high excitation molecular collisional data. The excitation properties (both rotational and vibrational) of molecules reveal the physical conditions of the gas and are effective probes of energetic environments, such as PDRs, CSEs, and the surface layer of PPDs. For a quantitative understanding of micro-processes (e.g., collisional molecular excitation, radiative transfer, etc.), we applied state-of-the-art simulation techniques and accurate collisional rate coefficient data. Realistic models for complex astrophysical environments, e.g., PDRs and CSEs, are highlighted.

- Chapter 2

  SiO emission lines are important probes of chemical processes in diverse astrophysical environments, commonly observed in shocks associated materials (e.g., in the outflows of young stellar objects, both low- and high-mass, and in the envelopes of evolved stars). Modelling SiO emission for conditions of NLTE requires collisional rate coefficients due to H_2, H, and He impact, with the first of these of limited availability. Unknown collisional rate coefficients are often estimated from known systems. For the case of SiO-H_2, rate coefficients have previously been adapted from a different collider, He, based on a reduced-mass scaling approach. We construct comprehensive SiO collisional rate coefficients data with multiple colliders (H_2, He and H) and rovibrational transitions up to $v = 5$ and $J = 39$. A reduced-potential scaling approach is used to estimate unknown collisional data. We investigate the rotational and rovibrational SiO emission in various astrophysical environments, including PDRs and the envelope of the O-rich AGB star VY Canis Majoris.

- Chapter 3

  Being the second most abundant molecule in the ISM, CO has been well observed and studied as a tracer for many astrophysical processes. Highly rovibrationally excited

CO emission is used to reveal features in intense UV-irradiated environments such as H II regions and PDRs. Collisional rate coefficients for vibrationally excited CO were previously unavailable, thus limiting the NLTE simulation for these environments. We revisit NLTE CO excitation properties with comprehensive collisional data, including rovibrationally excited states (up to $v = 5$ and $J = 40$) colliding with H_2, H, and He. We then conduct CO molecular analyses in various NLTE astrophysical environments. In one-dimensional models, warm CO line emission and rovibrational diagnostic line ratios, with respect to density and temperature, are studied. We also investigate molecular properties in more complex environments, such as PDRs and the outflow of carbon star IRC +10216.

- Chapter 4

  H_2 is the dominant molecular species in the vast majority of interstellar environments and it plays a crucial role as a radiative coolant. In PDRs, it is one of the primary emitters in the near- to mid-infrared, which are due to lines originating from highly excited rovibrational levels. Previously, collisional data for rotational levels $J \geqslant 9$ are sparse, particularly for H_2-H_2 collisions. Utilizing new calculations of high rotational collisional rate coefficients for para- and ortho-H_2 colliding with H_2 (up to the maximum value for $v = 0$: $J = 31$), we investigate the excitation properties of H_2 in a range of astrophysical environments, with the focus on PDRs.

- Chapter 5

  Conclusion and outlook of this work.

Chapter 2

Ro-vibrational analysis of SiO in UV-irradiated Environments[1]

[1]Zhang, Ziwei E., Cumbee, Renata. S., Stancil, Phillip. C., and Ferland, Gary. J., 2018. Accepted by *Molecular Astrophysics*. Reprinted here with permission of publisher.

2.1 Introduction

Being one of the first detected molecules in the ISM, SiO has been an important probe of physical and chemical processes in warm molecular regions (Wilson et al. 1971; Ziurys et al. 1989). In many astrophysical environments, SiO is highly excited both rotationally and vibrationally. Here we construct comprehensive collisional rate coefficients data for spectral analysis of SiO due to H_2, H and He collisions, with a reduced-potential scaling method. (Table 2.1 shows the SiO data update details. See Section 2.2 for data construction.) With the new data set, we perform a NLTE rovibrational analysis of SiO in various astrophysical conditions.

Shown in Figure 1.2, SiO is the the main gas-phase carrier of Si in PDRs (Schilke et al. 2001), and its emission is often found to imply warm temperatures due to extreme conditions such as shocks and intense UV radiation. Dependency on density and temperature for SiO is due to the gas-phase silicon chemical reactions which were discussed in detail previously by Herbst et al. (1989) and Langer & Glassgold (1990). Throughout the PDR, the SiO abundance varies with extinction, it becomes the dominant gas-phase Si carrier at higher A_V, typically when $A_V > 6$ (Sternberg & Dalgarno 1995; Hollenbach & Tielens 1999; Tielens 2005).

One of the intriguing aspects of PDR studies is their application to young stellar objects (YSOs), where SiO emission lines play important roles when studying primary and secondary outflows, as well as jets, which are formed in different stages of the YSO evolution (Tan et al. 2014). They are mostly found in enhanced density regions such as the leading edges of shocks. In the early stage of YSO evolution, SiO is often found to be highly collimated along the jets (Arce et al. 2007; Shang et al. 2007). In general, SiO is the best indicator for jets (its abundance is considered to be enhanced by disk wind and shocks), providing a close-up view when studying molecular outflows around both low- and high-mass YSOs, while other tracers, such as CO, suffer from contamination in swept-up cavities (Gueth et al. 1998; Leurini et al. 2013; Tan et al. 2014). Both low and high rotational transition lines have

been observed in massive star formation regions such as Orion KL for J = 1-0, J = 2-1, and J = 8-7 (Beuther et al. 2005), IRAS 17233-3606 (Leurini et al. 2013) for J = 5-4 and J = 8-7, and the high-mass protocluster NGC 2264-C (López-Sepulcre et al. 2016). With high temperature and density, SiO masers could also be formed in extremely high velocity protostellar winds close to the protostars (Glassgold et al. 1989). Previous studies mainly suggested SiO is an ideal tracer for protostellar activity (van Dishoeck & Blake 1998; Nisini et al. 2007; Nguyen-Lu'o'ng et al. 2013).

SiO is one of the signature molecules detected in O-rich AGB stellar envelopes. In the recent study on O-rich AGB stars with *Herschel*/HIFI, highly excited rotational emission lines from vibrationally excited levels for different molecules were detected, with the highest transitions of SiO up to v = 1, J = 15-14 and v = 1, J = 23-22 in R Dor and W Hya (Justtanont et al. 2012). For the case of IK Tauri, one of the most investigated O-rich AGB stars, recent studies suggested SiO is depleted in the envelope, likely related to dust formation (Gobrecht et al. 2016). It is also expected to be highly excited near the source, right after it was formed, which makes it a good probe of near-photospheric activity. (Decin et al. 2010; Gobrecht et al. 2016). Meanwhile, SiO holds a key position in studying dust formation in AGB envelopes: silicates start forming from gas-phase SiO and other components at ∼1000 K (Millar 2016; Van de Sande et al. 2015). In this chapter, we attempt a spectral analysis including highly excited rovibrational transitions in both near- and mid-infrared bands for the O-rich AGB star, VY Canis Majoris.

Currently, the SiO LAMDA format data file includes rate coefficients from one collider: H_2, adapted from He, based on a reduced-mass scaling approach (Schöier et al. 2005; Dayou & Balanca 2006). Our newly constructed SiO collisional rate coefficient data set is applied in the investigation of SiO emission and abundance in UV-irradiated regions, such as PDRs and AGB CSEs.

2.2 Rovibrational SiO Data Construction

Rovibrational analysis for SiO with RADEX and Cloudy requires the collisional rate coefficients in LAMDA data format (Schöier et al. 2005). The current LAMDA database includes pure rotational SiO data obtained with a reduced-mass scaling approach from He (Dayou & Balanca 2006; Schöier et al. 2005). Recently it has been suggested that scaling via the interaction potential energy surface (PES) well-depth and the reduced masses of the collisional systems (as shown in the following suggested function) is more reliable (Walker et al. 2014).

$$k^{Z}_{j\to j'}(T) = \left(\frac{\mu_Z \varepsilon_Z}{\mu_Y \varepsilon_Y}\right)^{C} k^{Y}_{j\to j'}(T). \tag{2.1}$$

Here, μ is the reduced mass and ε the van der Waals well depth of the potential energy surface. For SiO, $\varepsilon_{H_2} \approx 293$ (Yang et al. 2018), $\varepsilon_{He} \approx 26.596$ (Dayou & Balanca 2006), $\varepsilon_H \approx 11157$ cm^{-1} (Jimeno 1999) and we take $C = 0.5$.

Based on the SiO-H calculations ($v = 0-5, J = 0-39$) from Palov et al. (2002, 2006) and original SiO-H_2 LAMDA data file ($v = 0, J = 0-40$), we construct comprehensive rovibrational collisional rate coefficient data set (summarized in Table 2.1). SiO-He rovibrational rate coefficients are obtained by, 1) retrieving $v = 0$ data from LAMDA database (reduced-mass approach with a factor of 1.38) (Dayou & Balanca 2006; Schöier et al. 2005), 2) scaling $v = 1-5$ SiO-H data (Palov et al. 2002, 2006) with reduced-potential method and 3) including high temperature data from Balanca & Dayou (2017). We also apply reduced-potential scaling method to SiO-He ($v = 0$) and -H ($v = 1-5$) data to estimate SiO-H_2 rate coefficients.

In Figure 2.1 and Figure 2.2, we compare SiO-H_2 data from reduced-potential scaling method in this work with recent theoretical calculation from Yang et al. (2018), as well as from Dayou & Balanca (2006), Turner et al. (1992) and reduced-mass scaling data (Schöier et al. 2005) in the original LAMDA file. Reduced-potential scaling data presents good agreement with state-of-the-art calculations, thus showing the validity of such method.

Einstein A coefficients adapted from Barton et al. (2013) are shown in Figure 2.3. For the vibrational ground state, A values increase with J. It is unlikely for population inversion to occur with only $v = 0$ states present, making it impossible for radiative transfer analysis for SiO masers using previous data. The peaks around lower Js indicate pure vibrational transitions at these states are quite probable, leading to the same trend of piling-up effects in the NLTE rotation diagrams (Leiden F and V models in 2.3.2).

The complete LAMDA data file is available on the UGA molecular excitation database[2] and Cloudy rovibrational database.

Table 2.1: Rovibrational SiO Data Summary.

Data	Colliders	J	v
SiO-H_2 LAMDA data (Reduced-mass scaling)	H_2	0-40	0
SiO data updated (Reduced-potential method)	H[a]	0-39	0-5
	H_2 [b]	0-39	0-5
	He[c]	0-39	0-5

[a] Palov et al. (2002, 2006).
[b] $v = 0$ data scaled from SiO-He with reduced-potential method, $v = 1 - 5$ data scaled from SiO-H with reduced-potential method.
[c] $v = 0$ data retrieved from LAMDA database (Dayou & Balanca 2006) (Schöier et al. 2005), $v = 1 - 5$ data scaled from SiO-H with reduced-potential method and high temperature data from Balanca & Dayou (2017).

[2] www.physast.uga.edu/amdbs/excitation/

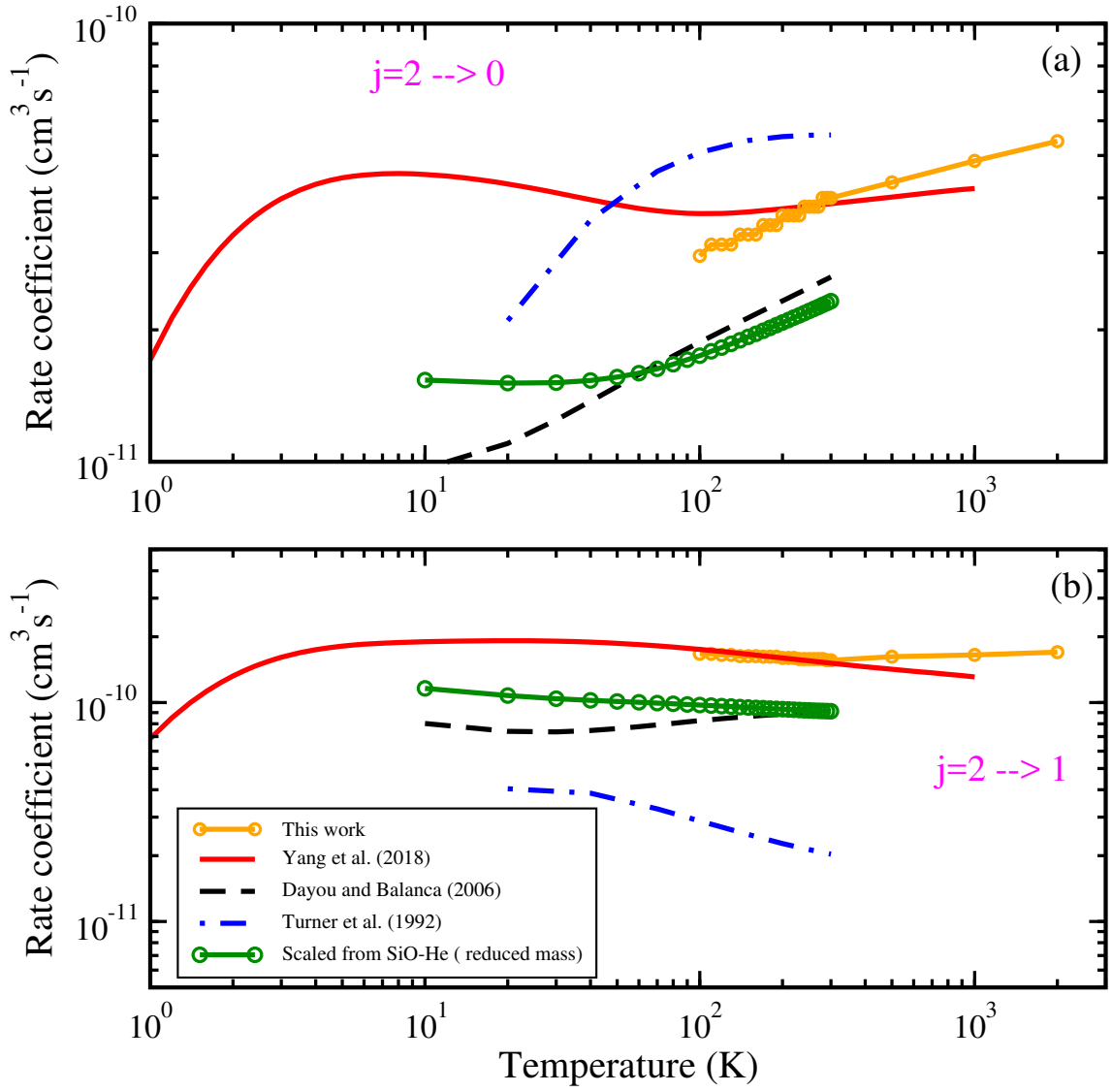

Figure 2.1: SiO Data Comparison A.

Comparison of SiO-H_2 data ($v = 0, J = 2 \rightarrow 0$ and $v = 0, J = 2 \rightarrow 1$) in this work using reduced-potential scaling with theoretical calculations from Yang et al. (2018), Dayou & Balanca (2006), Turner et al. (1992) and reduced-mass scaling data (Schöier et al. 2005).

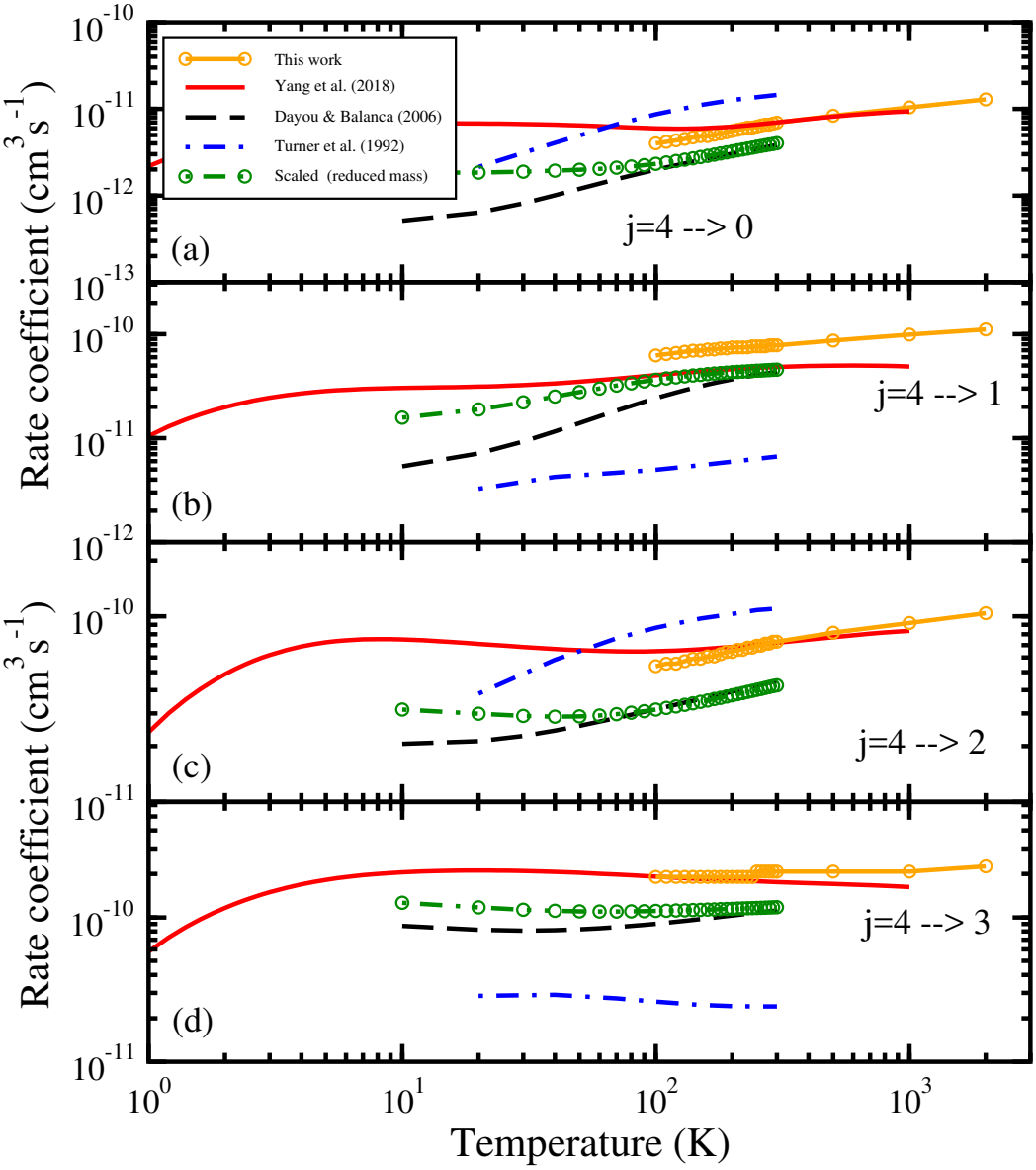

Figure 2.2: SiO Data Comparison B.

Comparison of SiO-H_2 data ($v = 0, J = 4 \rightarrow 0$, $v = 0, J = 4 \rightarrow 1$, $v = 0, J = 4 \rightarrow 2$ and $v = 0, J = 4 \rightarrow 3$) in this work with theoretical calculations from Yang et al. (2018), Dayou & Balanca (2006), Turner et al. (1992) and reduced-mass scaling data (Schöier et al. 2005).

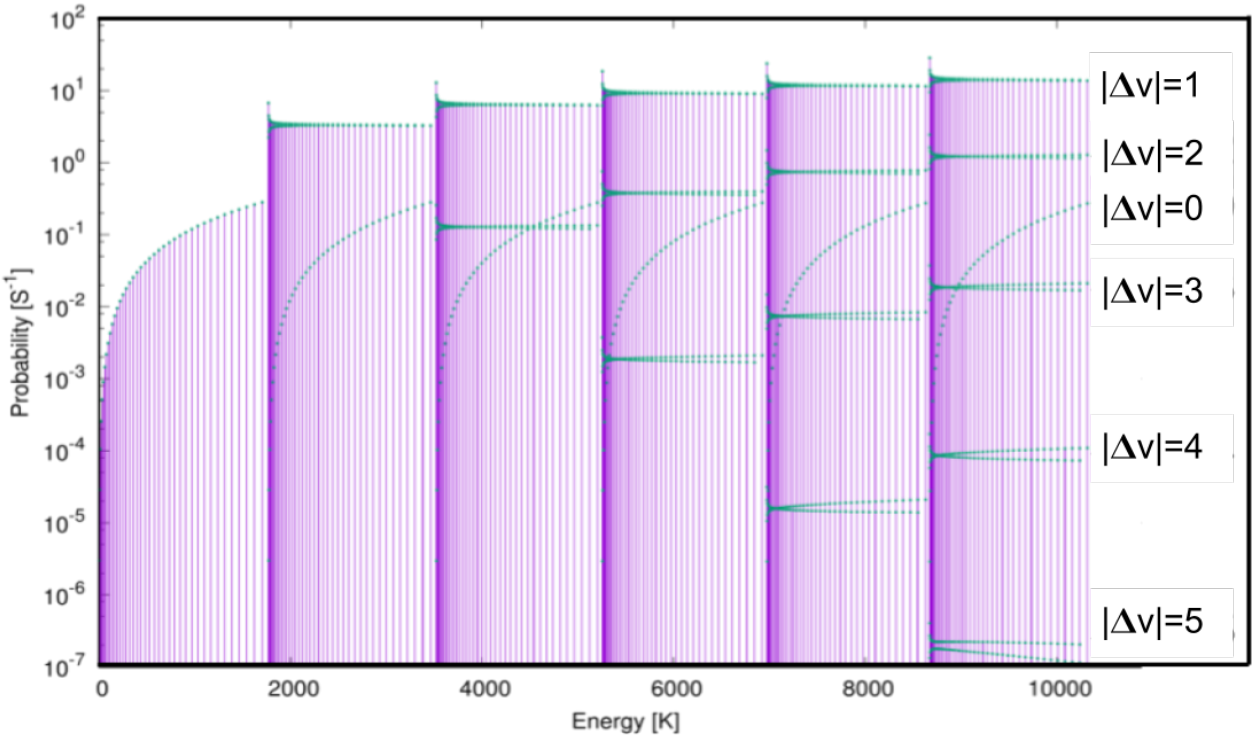

Figure 2.3: SiO Einstein A Coefficients

Einstein A coefficients as a function of upper level energy adapted from Barton et al. (2013), transitions marked with green points.

2.3 NLTE modelling

To analyze SiO rovibrational emissions, we first use RADEX (van der Tak et al. 2007) to model simple homogeneous environments, studying relevant quantities such as gas temperature and densities with line ratio diagnostics. With Cloudy (Ferland et al. 2017), we consider more complex environments including various physical and chemical processes. We conduct a comparison study on two sets of Leiden benchmark PDR models with different conditions for NLTE cases (Röllig et al. 2007). Lastly, we construct a model of the envelope for the well-studied O-rich AGB star, VY Canis Majoris, and compare modelling results with observation and other theoretical analysis (Matsuura et al. 2013).

2.3.1 RADEX modelling and Results (Uniform environments)

Using RADEX, we construct diagnostic plots and line spectra to study SiO excitation in homogeneous environments (for model parameters, see Table 1.1).

Diagnostic plots are a helpful and simple way to estimate density, temperature and other physical quantities from observed spectral data. Figures. 2.4 and 2.5 show line ratio diagnostic plots for different rovibrational transitions of SiO. Notice the line emissions from different vibrational states are rather comparable in relatively dense and warm environments, resulting in low line ratios, with higher vibrational levels expected to be more excited. Line ratios are very sensitive to temperature in certain density ranges, making them useful as temperature diagnostics. For rotational near-by transitions, line ratios between lower and higher level transitions are often around 1, suggesting higher rotational levels are considerably populated in such conditions, which is also indicated in the line spectra shown below. It is possible for masers to be formed with such population inversions (Glassgold et al. 1989). These diagnostic plots would be found most helpful at highly UV irradiated dense cloud surfaces (though we neglect UV radiation in our sample plots). Similar rovibrational diagnostic plots for observed emission lines, $v = 1, J = 15 - 14$ and $v = 1, J = 23 - 22$ observed in R

Dor (Justtanont et al. 2012), could be constructed with RADEX for theoretical modelling now with higher vibrational level rate coefficients available.

We also calculated line spectra to study relative intensities in various environment, shown in Figures 2.6 to 2.8. Full line spectra as in Figure 2.6 compare line emissions at different temperatures at 10^4 cm^{-3}. SiO is excited to higher vibrational states in all cases with increasing intensity along with the temperature increase. Observation window for these emission lines are marked at the top panel, extending to near- to mid-infrared for vibrational bands. In Figure 2.7, in the case of a high collider density of 10^8 cm^{-3} at 300 K, higher rotational excitation are significantly more intense than lower excitation, consistent with diagnostic plot results. Note the cut-off in pure rotational lines near 150μm is due to upper limit of $J = 39$ in our rotational basis. The fundamental band ($\Delta v = -1$) in warm environments (1000 K) gradually approaches LTE, while the intensity peaks of the R- and P-branches also shift to higher Js, with increasing density as in Figure 2.8. Certain lines are relatively intense even for collider density as low as 10^6 cm^{-3}, making them good candidates for future mid-infrared observations. The sensitivity with density of these emission lines also suggests related line ratios could be good diagnostics of density in warm molecular clouds, e.g., PDRs and PPDs.

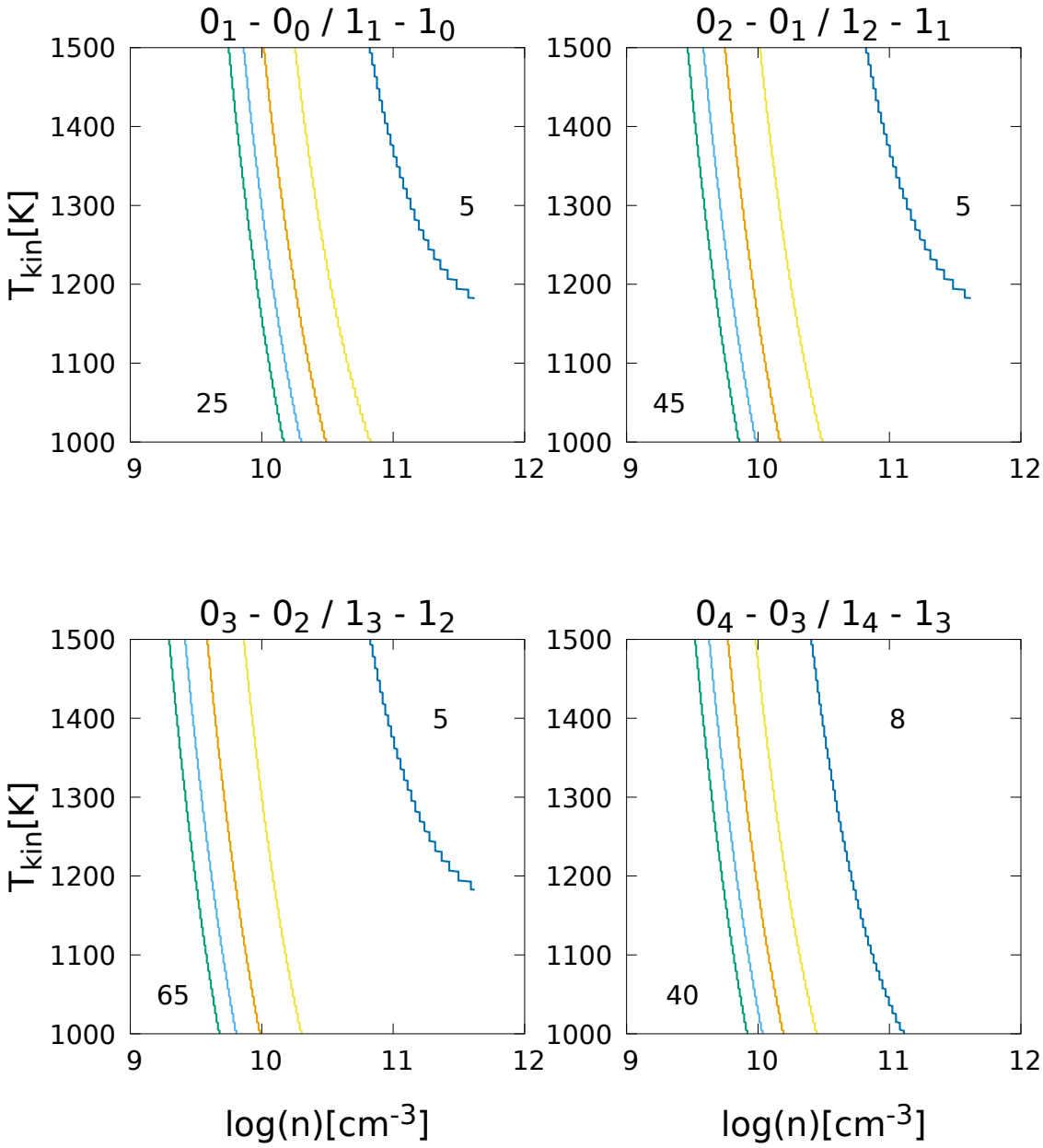

Figure 2.4: SiO Diagnostic Line Ratios A

Diagnostic line ratios as a function of kinetic temperature and gas density. ($v = 0/v = 1$, SiO rotational transitions in different vibrational states for a warm and dense environment.)

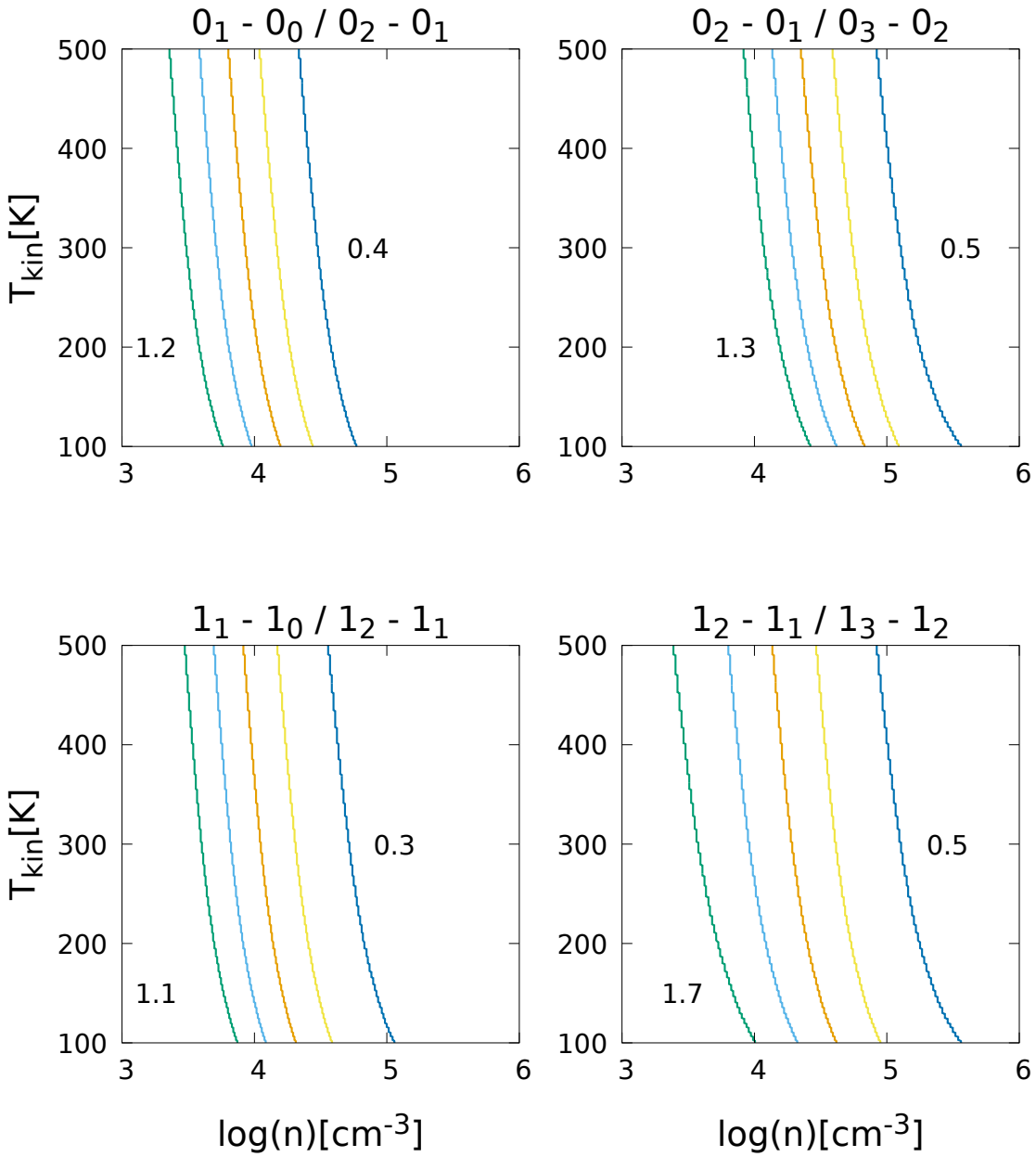

Figure 2.5: SiO Diagnostic Line Ratios B

Diagnostic line ratios as a function of kinetic temperature and gas density. (Rotational transitions in same vibrational states in a cooler environment, transitions in the vibrational ground state are shown in the top panel while bottom panel shows cases for $v = 1$.)

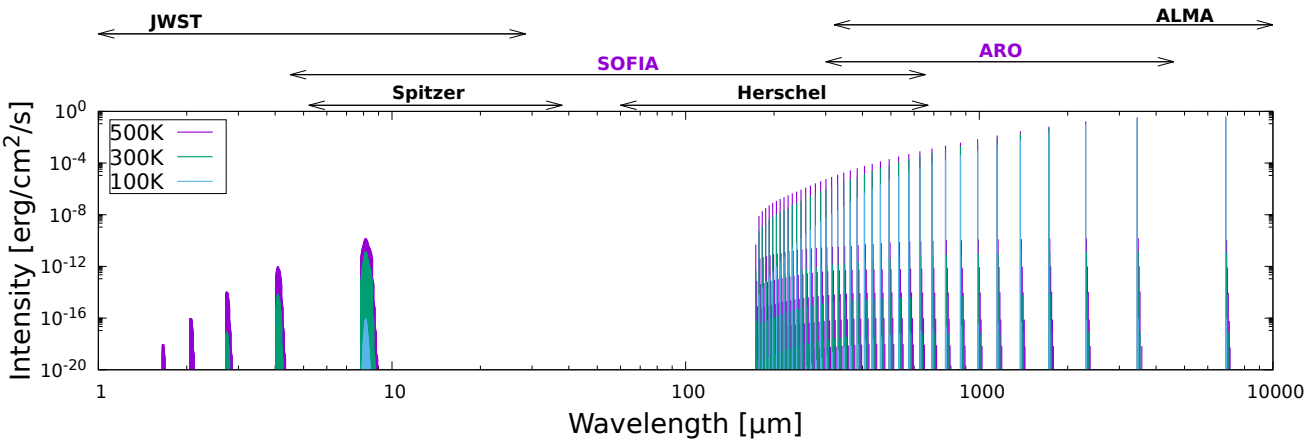

Figure 2.6: SiO Full Rovibrational Spectrum

SiO full line spectra with collider (H_2, H and He) density of 10^4 cm^{-3} at 100 K, 300 K and 500 K (indicated with colors). Telescope wavelength coverages are marked on the top.

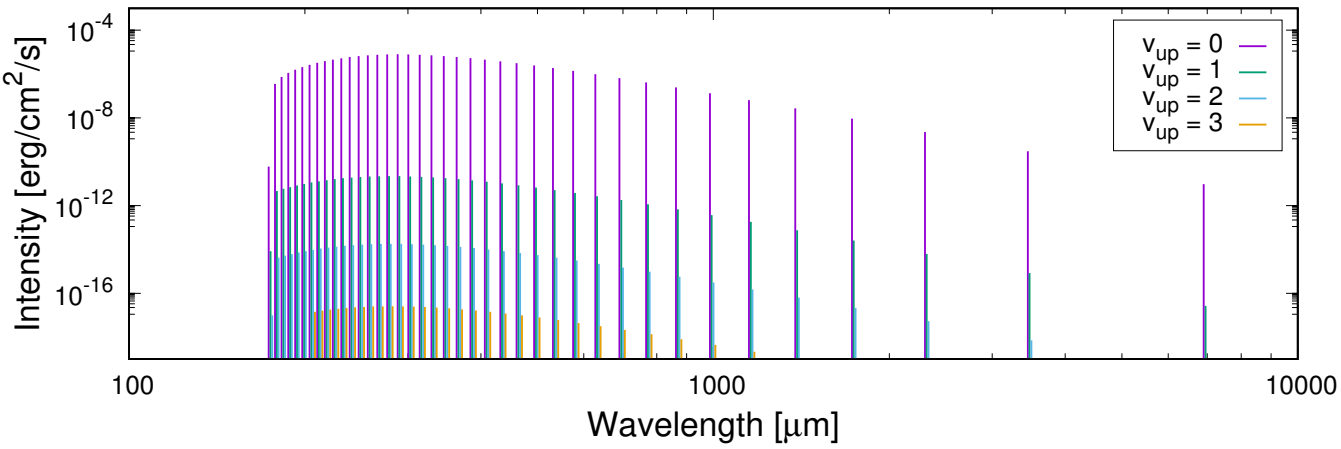

Figure 2.7: SiO Rotational Spectrum

SiO pure rotational spectrum with a total collider (H_2, H and He) density of 10^8 cm^{-3} at 300 K, different vibrational states indicated by color.

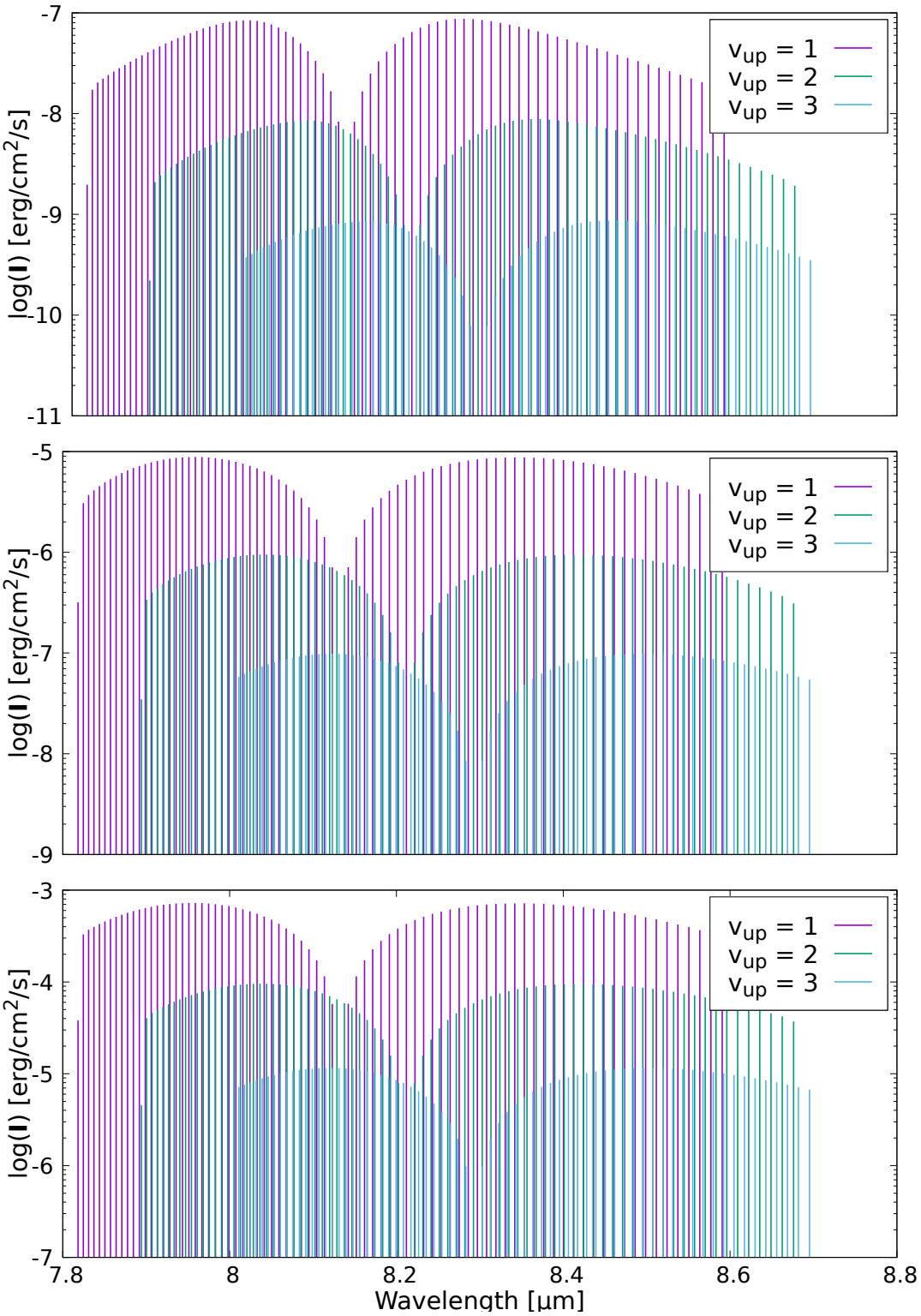

Figure 2.8: SiO Fundamental Band

SiO ro-vibrational fundamental spectrum for 1000 K, fundamental band (Δv=-1), with total collider (H_2, H and He) density of 10^6 cm^{-3} (top), 10^8 cm^{-3} (middle) and 10^{10} cm^{-3} (bottom). Different upper states are indicated by colors.

2.3.2 Cloudy PDR Modelling and Results

With Leiden benchmark models (see Table 1.2), we investigate rovibrational SiO emission and other properties in eight representative PDRs, in order to obtain a deeper perception of Si related chemistry and silicate formation. More information regarding chemistry networks and mechanisms could be found in Ferland et al. (2017).

We present a sample of SiO line spectra for the Leiden PDR models as shown in Figure 2.9. In most cases, SiO is excited up to at least $v = 2$, and often as high as $v = 5$ (the limit of our database), while pure vibrational transitions in the near-infrared and mid-infrared range have relatively strong emission. Both sets of models share the same trend: high UV radiation and density pump up high rovibrational states. Instead of having constant temperatures as in the F models, V models have self-consistent temperature profiles obtained by solving the heat equation. Source radiation is able to heat up the cloud, thus driving molecules to high rovibrational excitation states throughout the cloud. Such UV-induced high vibrational emissions can be especially seen in V2 - V4 models. It is worth noting that transitions in the fundamental band may be more intense than higher pure rotational transitions, useful when analyzing molecular excitation properties in PDRs.

Typically in PDRs, molecular rotation diagrams show two dominate rotation temperatures for lower Js (lower rotation temperature) and higher Js (much higher rotation temperature). For F models (Figure 2.10), with constant gas temperature, SiO mainly accumulates in the vibrational ground state, showing quasi-LTE behavior. Using a simple linear fit, the kinetic temperatures of 10 - 30 K could be obtained for F models. A more deliberate method to treat quasi-LTE cases is discussed in Goldsmith & Langer (1999), hence we only show the general population trends and a few reference temperatures here. Multiple components result for V models in the lower set of Figure 2.10, where we give a few reference linear fits. V2 and V4 models present two distinguished temperatures, which represent more realistic PDR environments with the high temperature ($\sim$ 200K) near the radiation source and the low temperature ($\sim$ 10K) further into the cloud. UV radiation partially contributes to high

J excitation and drives population up to higher vibrational states. Similar population trends appear throughout different vibrational states due to the dominance of the $\Delta v = 0$ cascade. The piling-up feature at lower Js is related to the trend of Einstein A coefficients for pure rotational transitions (See Section 2.2). It is also possible to deduce a vibration temperature using same J in different vibrational states, which will be explored more in Section 2.3.3.

To further investigate SiO rovibrational line emission in general PDR environments, we present two sets of continuum spectra for the Leiden PDR models in Figures 2.11 and 2.12. SiO transition lines are marked as dots. Due to the relative low density and temperature, we expected the abundance of SiO to be small due to unfavorable chemistry and high levels of depletion onto dust grains. However, both F and V models show clear SiO rotational lines (zoomed in bottom panel), dominant transitions indicated in the plots are listed in Table 2.2. Some of these emission lines, which have intensities a factor of 2-3 above the continuum, are maser candidates. Pure vibrational SiO lines are embedded in H_2 and He continuum (radiative recombination).

With the wide range of astrophysical sources that PDRs are associated with (such as PPDs, AGB stars and star forming regions), these analyses could be implemented in various environments and help to unveil the molecular behaviours.

Table 2.2: Intense SiO Lines in Leiden PDR Model Continuum.

Wavelength (μm)	Transition (v', J') $\rightarrow$ (v, J)
6895.28	(0, 1) $\rightarrow$ (0, 0)
3447.26	(0, 2) $\rightarrow$ (0, 1)
2303.18	(0, 3) $\rightarrow$ (0, 2)
1723.44	(0, 4) $\rightarrow$ (0, 3)
1511.46	(0, 6) $\rightarrow$ (0, 5)
987.79	(0, 7) $\rightarrow$ (0, 6)
766.75	(0, 9) $\rightarrow$ (0, 8)

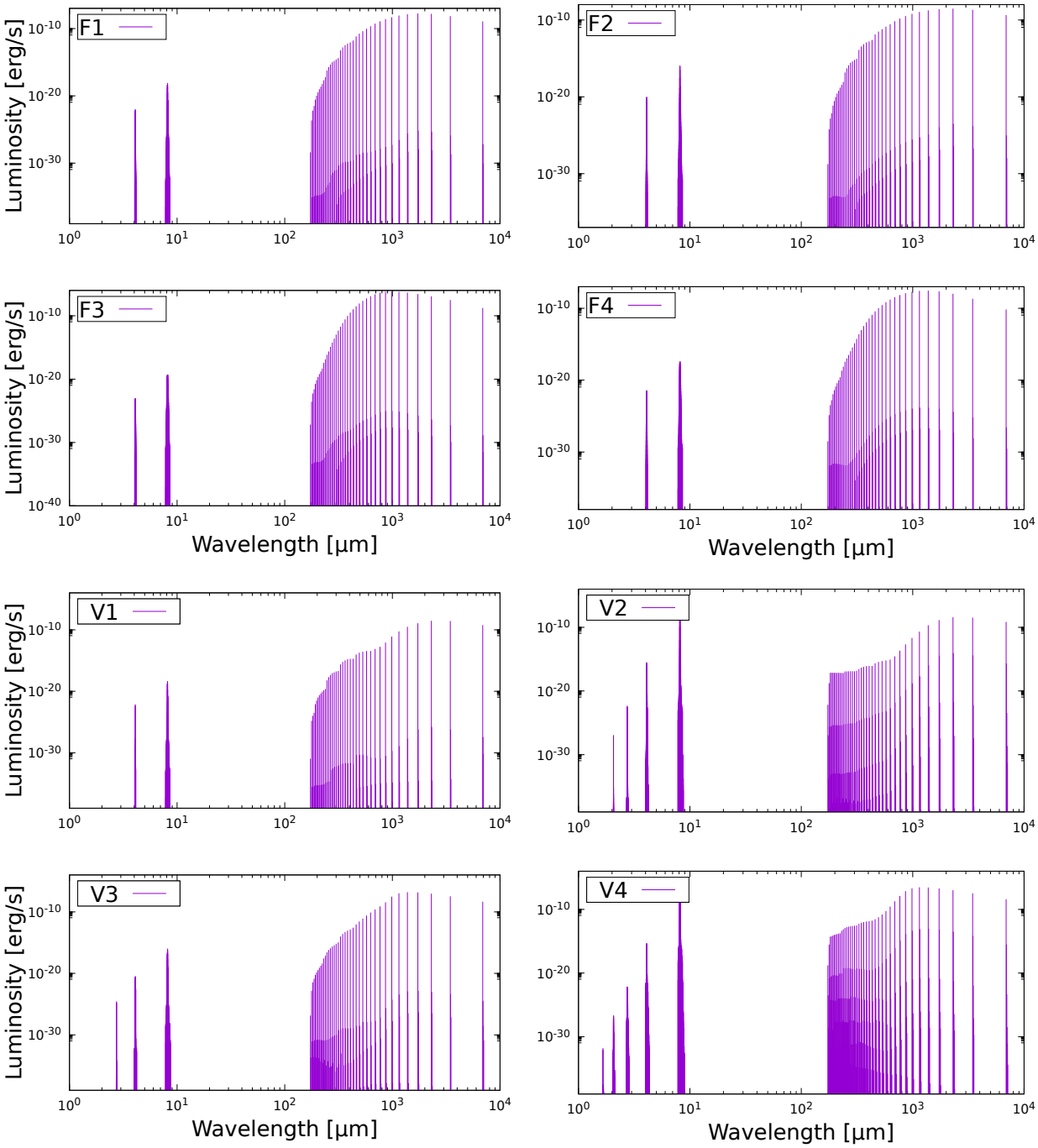

Figure 2.9: Full SiO Line Spectrum for Leiden PDR Models.

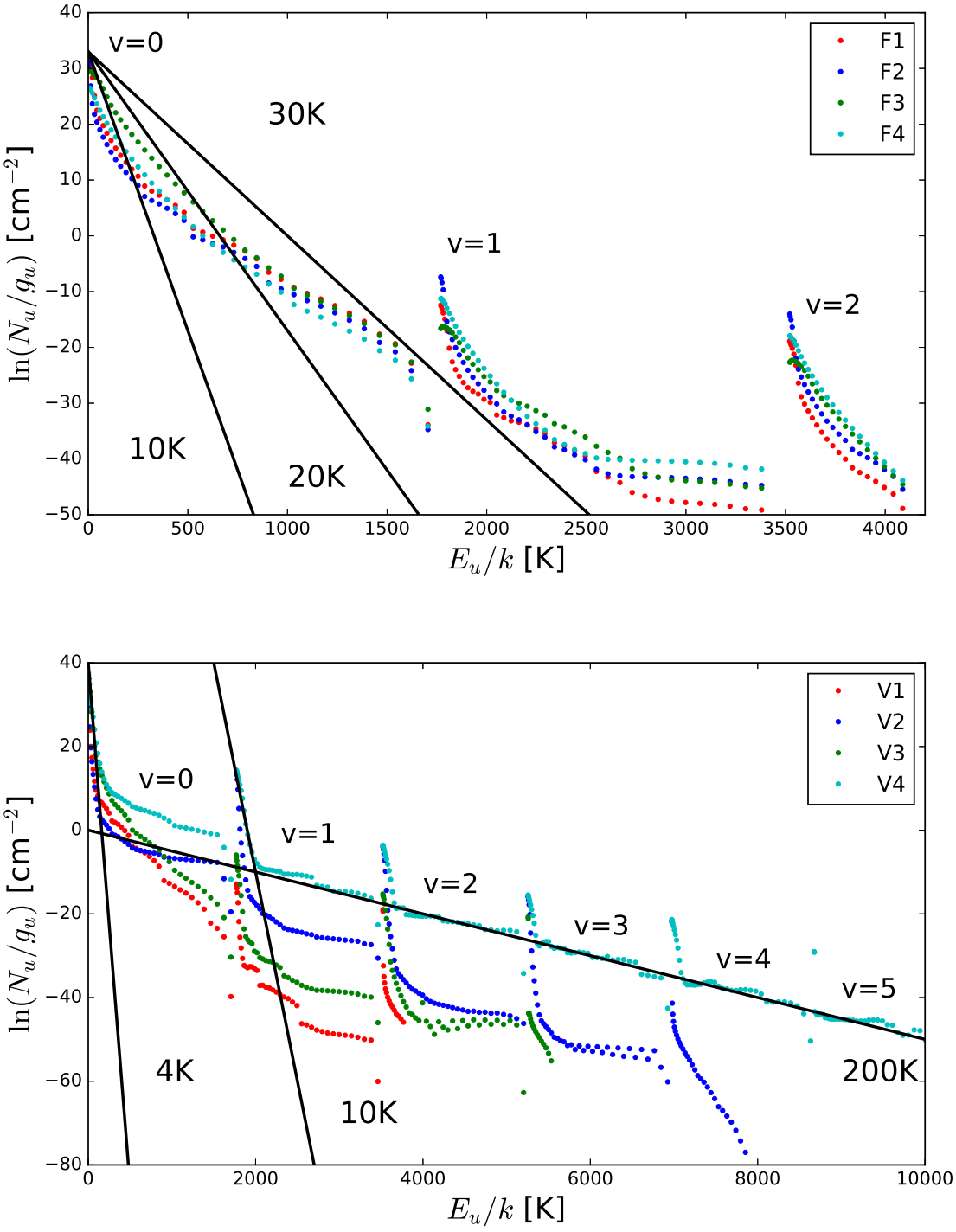

Figure 2.10: SiO Rotational Diagram for Leiden PDR Models.

Solid lines are reference linear fit rotation temperatures.

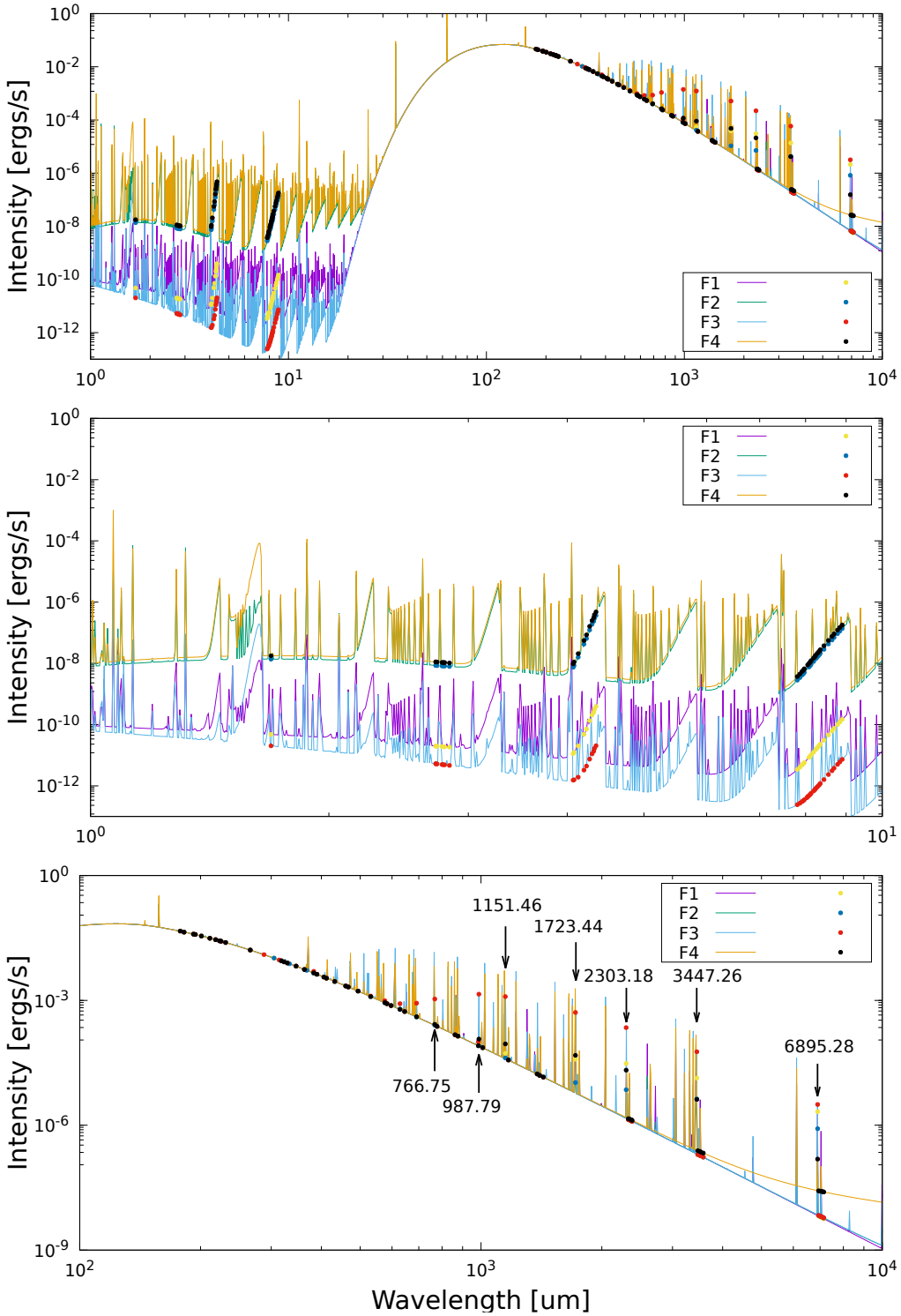

Figure 2.11: Continuum Spectra for Leiden PDR F models with SiO Emission.

SiO lines marked as points. Lines indicated (bottom) in rotational spectrum are listed in Table 2.2.

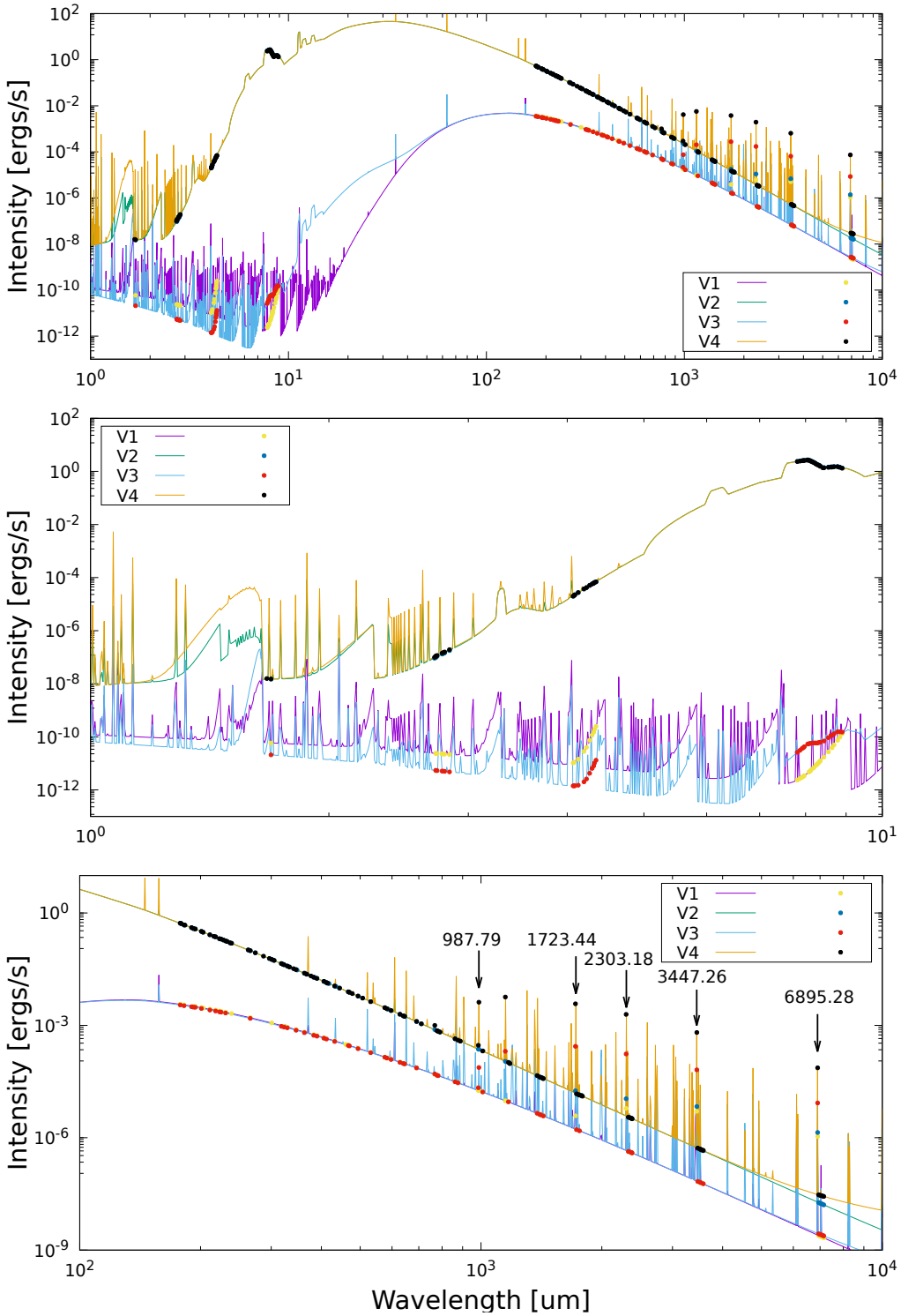

Figure 2.12: Continuum Spectra for Leiden PDR V models with SiO Emission.

SiO lines marked as points. Lines indicated (bottom) in rotational spectrum are listed in Table 2.2

2.3.3 VY Canis Majoris Model with Cloudy

VY Canis Majoris (VY CMa), one the of the brightest AGB stars, has been very well observed and studied (Polehampton et al. 2010; Alcolea et al. 2013; Shenoy et al. 2013). It is one of the earliest SiO maser sources detected. In the past, molecular analysis was only conducted for the vibrational ground state (Richter et al. 2013, 2016; Matsuura et al. 2013; Vlemmings et al. 2017). Higher vibrational state data, not only reveals properties of chemical structure and dust formation in intense conditions such as high radiation and temperature, but is also crucial for maser formation since population inversion is only possible with the existence of higher v states (discussed in Section 2.2).

In the following section, we construct a detailed NLTE CSE model for VY CMa, then compare our predictions of the spectral energy distribution (SED) and integrated line intensity with representative previous work from Matsuura et al. (2013), key model parameters are shown in Table 2.3 (Matsuura et al. 2013; Wittkowski, M. et al. 2012). We fit the SED to observations as shown in Figure 2.13 in order to estimate the dust and chemical composition, as well as other physical conditions. Predicted dust continuum with silicate absorption features ($\sim$10, 20 μm) agrees well with the ISO spectrum, while emission lines fit better with *Herschel* SPIRE spectrum (Matsuura et al. 2013). PACS spectrum (55-190 μm) shows more intense emission than our simulation, suggesting the potential need for rovibrational rate coefficients and NLTE analysis of other molecules that requires higher excitation conditions, such as CO, also not available in the LAMDA database.

As a result of high temperature and density, SiO in VY CMa is almost thermalized, as indicated in Figure 2.14. With linear fits, we deduced rotation temperatures for different vibrational states to be $\sim$350 K to $\sim$550 K with an increasing trend for higher v. We also obtain the vibration temperature for the six vibrational states available in our data, yielding 686 K for $J = 0$, $v = 0$-5. It is expected the vibration and rotation temperature would be approximately the same for full LTE cases, therefore, states within a given v are not in

complete LTE. These excitation temperatures are consistent with the range from Matsuura et al. (2013), in which SiO showed two temperature components ∼1000 K and ∼ 200 K.

The species abundances vary throughout the CSE as the temperature decreases and dust grains start to form. Hydrogen, carbon and silicon abundance profiles along the envelope are shown in Figure 2.15 as a function of physical depth (or radius from the center of the star) ($10^{15} - 10^{17.3}$ cm). Molecule abundances decrease following the -2 density power law, while SiO is depleted significantly around $10^{15.8}$ cm, where dust condensation and non-equilibrium chemistry set in. The temperature at the inner envelope is < 300 K (temperature profile shown in light blue shade), much lower than the deduced SiO excitation temperature, indicating SiO is radiatively pumped.

Figure 2.16 displays the rotational spectral line distribution for VY CMa. Spectral line energy distribution (SLED) are diagrams with integrated line fluxes per statistical weight as a function of initial excitation energy. They are direct ways to demonstrate rovibrational emission intensities and gas excitation properties, while also containing information about departure from thermal equilibrium. The pattern resembles Figure 2.3 for Einstein A coefficients with groups indicating pure rotational transitions and vibrational transitions of respective Δv. Rotational transitions in the vibrational ground state are shown in the bottom panel of Figure 2.16, with observational data marked as diamonds. The Cloudy prediction gives a better agreement at higher excitation than for lower J, while both show features of NLTE conditions. The strong lower J observed flux suggest there may be other excitation sources for SiO other than stellar (e.g., the interstellar radiation).

Table 2.3: Parameters for NLTE VY CMa Model.[a]

Model parameters	Values
Geometry & Dynamics	Static Sphere
R_{inner}: Inner radius (cm)	10^{15}
R_{outer}: Outer radius (cm)	$10^{17.3}$
T: Stellar temperature (K)	3580 (Blackbody)
L: Luminosity ($L_{\odot}$) [b]	2.3×10^5
n: Density (cm^{-3}) [c]	1.585×10^9
l: Distance (pc)	1170
d_{min}: Minimum dust size (μm)	0.001
d_{max}: Maximum dust size (μm)	0.01
Ω_b: Estimated beam area ($arcsecond^2$)	4

[a] Gas-phase chemical abundance: ISM.
Dust composition: 10% astronomical silicate and graphite.
See more in Van Hoof et al. (2004); Martin & Rouleau (1991).
[b] Power law index: -2.5 for ratio 1 at 0.02 Ryd.
[c] Power law index: -2.

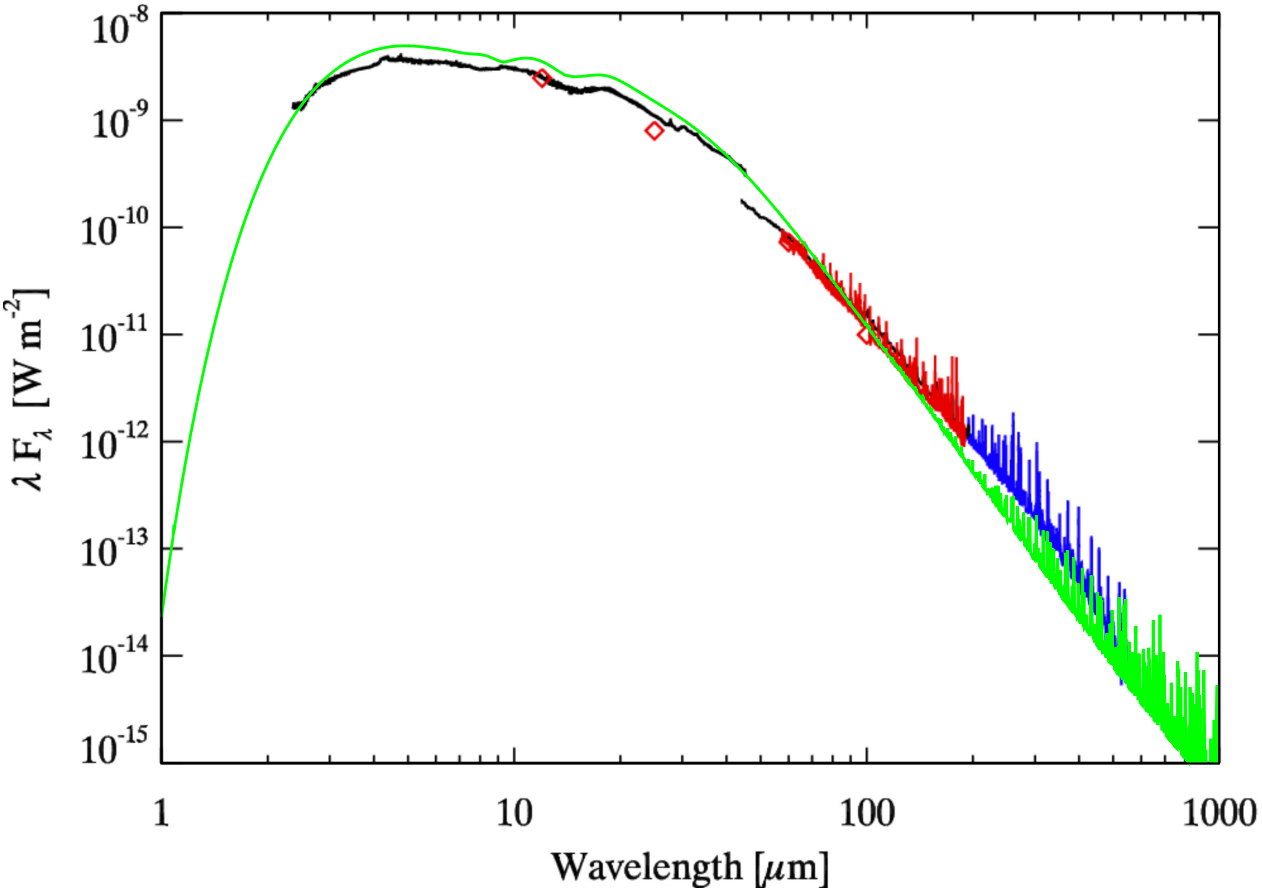

Figure 2.13: SED of VY CMa.

The infrared SED of VY CMa with observations from Matsuura et al. (2013), including SPIRE FTS spectrum (blue), PACS spectrum (red), ISO spectrum (Sloan et al. 2003; Polehampton et al. 2010) (black) and IRAS point source catalogue fluxes (Beichman et al. 1988) (red diamonds). Best-fit model with Cloudy spectrum is shown in green.

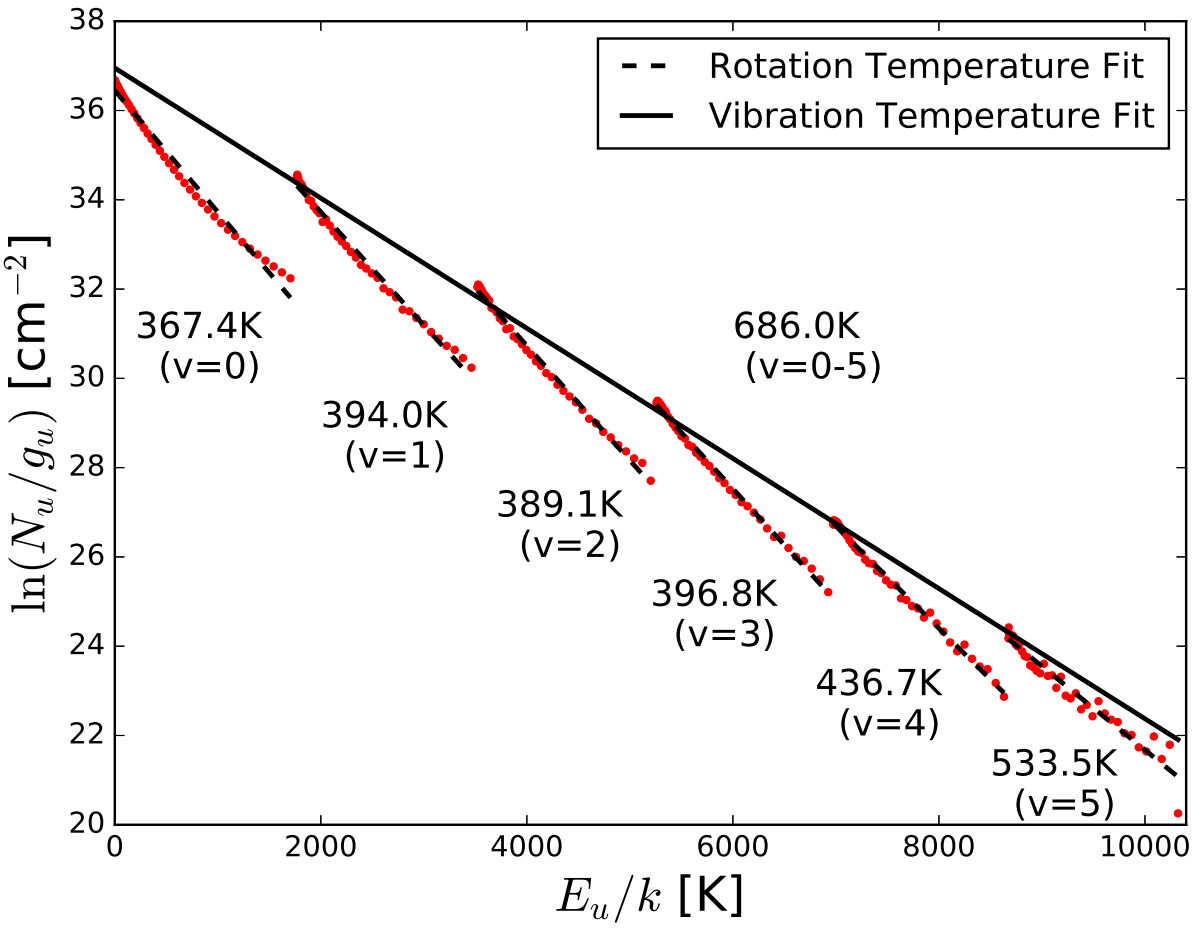

Figure 2.14: SiO Rotation Diagram for VY CMa.

SiO rotation diagram for VY CMa, rotation and vibration temperatures are deduced with linear fits as indicated.

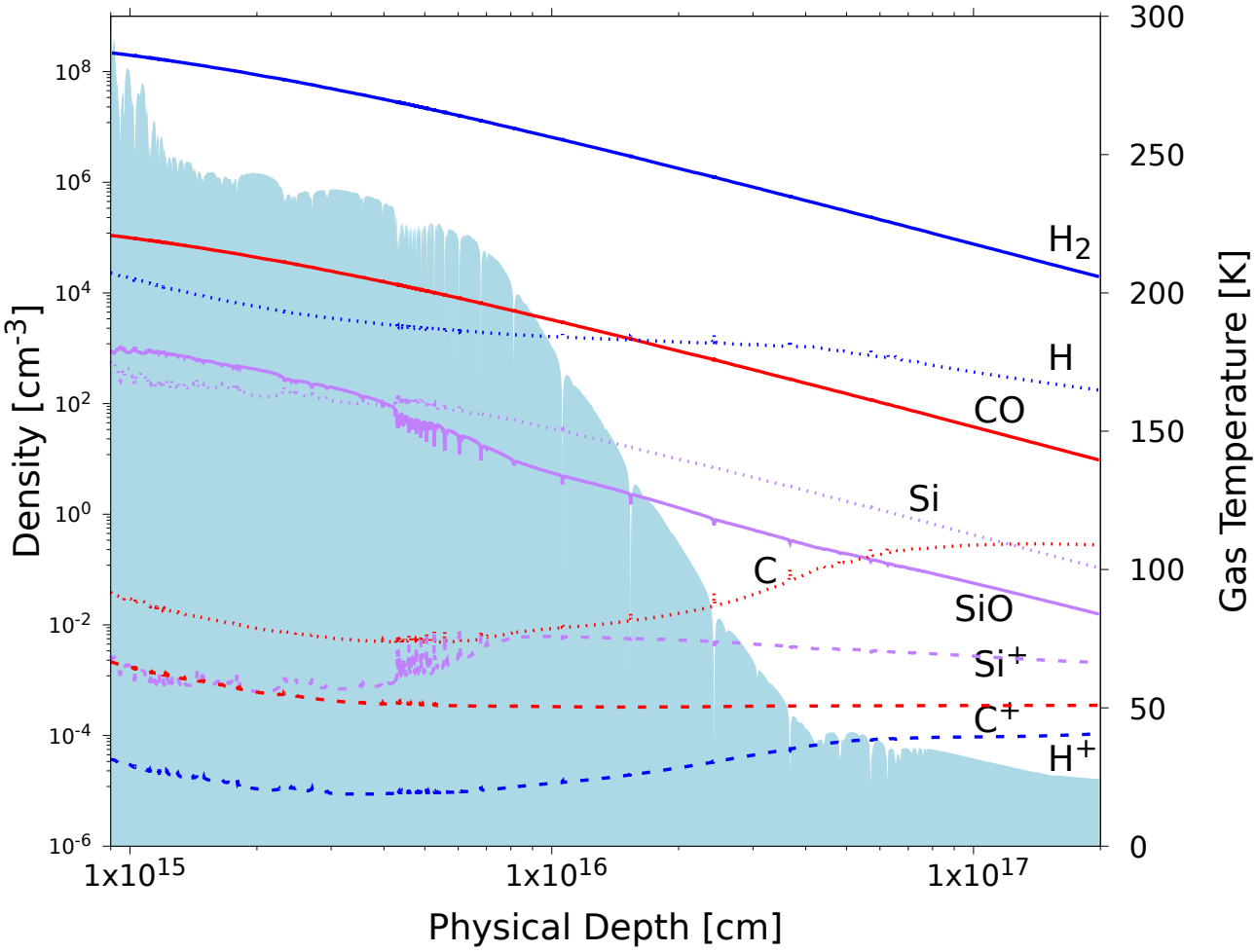

Figure 2.15: Species Abundances in VY CMa

Species abundances and kinetic temperature (light blue shade) as a function of physical depth in VY CMa, radiation source on the left. Hydrogen species in blue, carbon species in red and silicon species in purple.

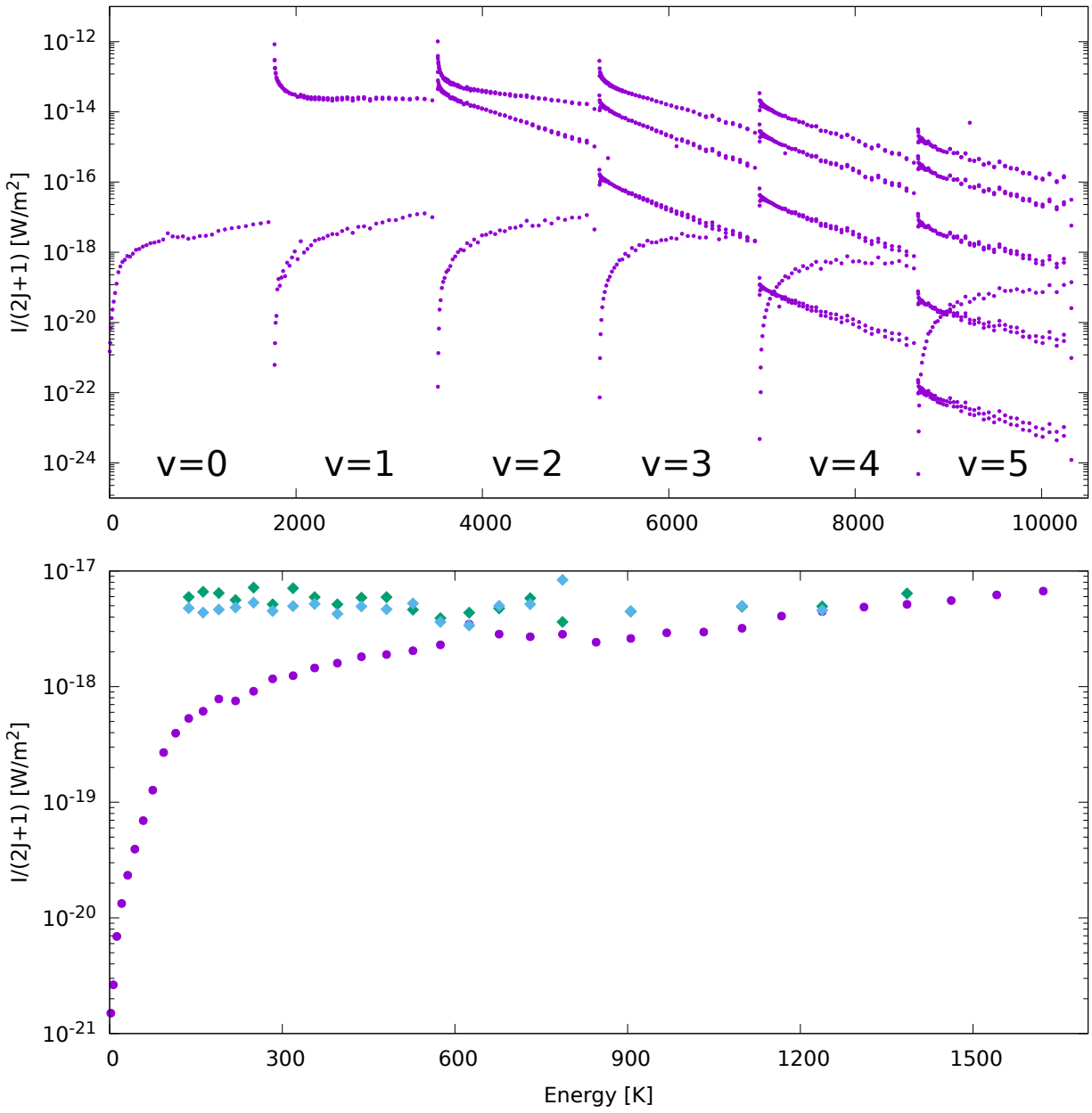

Figure 2.16: SLED for VY CMa.

Spectral line energy distribution for VY CMa for v = 0-5, J = 0-39 (top) and vibrational ground state (bottom). Herschel SPIRE data marked as diamonds for two different observations: OD 123 (green) and OD 317 (blue) (Matsuura et al. 2013).

2.4 Conclusion

Collisional rate coefficient are one of the fundamental parameters for NLTE analysis of irradiated interstellar environments. With the developments of astrophysical modelling, the need for theoretical calculations has been growing over the past few decades. However, there is still a shortage for such data for high rovibrational transitions due to the theoretical and experimental limitations. Vibrational transition data are especially needed for UV-irradiated regions, such as CSEs and YSOs, where molecules are pumped by radiation. Here we enhance the available collisional data for SiO to include: i) three colliders H_2, H and He; and ii) vibrational levels, while applying a reliable scaling method for missing rate coefficients. The effects of our comprehensive data are studied for various environments with the spectral simulation codes RADEX and Cloudy. As the collisional data has become more comprehensive, we expect to have a better understanding of SiO, as well as the chemistry and excitation of other molecules in PDRs and other important astrophysical environments.

In single species homogeneous environments with RADEX, we presented line emission evolution with gas property and diagnostic line ratios, showing significant vibrational excitation for high density and temperature.

We analyzed SiO emission and population with two sets of Cloudy PDR models. Spectral analysis show higher rovibrational SiO emission and potential masers, showing the advantage of including higher vibrational levels in our comprehensive data. F models with constant temperature show quasi-LTE behaviour in rotation diagrams, while V models with self-consistent temperature profile show two main temperature components (typical for PDRs).

Another advantage with rovibrational data is in studying highly excited environments, such as the CSE for AGB stars. Our model for VY CMa suggests SiO rovibrational levels are highly populated and excited throughout the entire envelope, approaching LTE, with both spectral and level population analysis. Our predicted SED fits previous observation well, while rotation diagram shows consistent excitation temperatures. More detailed modelling

and higher spatially resolved observation are needed to reveal the precise structure and composition, as well as molecular excitation and dust formation properties.

Our predicted results show promising applications for future NIR to submm observation and related exploration. Explicit SiO-H_2 collisional calculations are in progress (Yang et al. 2018) as the current work uses a reduced-potential scaling method to deduce the rate coefficients from SiO-H_2 and -He data. We expect to apply rovibrational rate coefficients data for other molecules, to get a better understanding of the structure and properties of UV-irradiated regions.

Chapter 3

Revisiting Non-Local Thermodynamic Equilibrium Rovibrational Excitation of CO in UV Irradiated Environments[1]

[1]Zhang, Ziwei E., Yang, Benhui, Walker, Kyle M., Forrey, Robert C., N. Balakrishnan, and Stancil, Phillip C. Submitted to *The Astrophysical Journal*, Oct 22, 2018.

3.1 Introduction

Molecular excitation properties are important indicators for astrophysical conditions of the ISM, while CO plays a long-standing crucial role in related studies, due to its large abundance and observational advantages. CO provides ideal diagnostics used to probe large H II regions and PDRs. In recent observations of H II regions, RCW 32 and M8, CO line ratios revealed the structures and dynamics of these objects, while highly rotational excited transitions were used to deduce other physical properties, such as temperature and density (Enokiya et al. 2017; Tiwari et al. 2018). As for vibrational excitation, CO fundamental band emissions are observed and analyzed in the outflow of Orion Peak 1 and Peak 2, with two rotation temperature components ($\sim$ 200-400 K) and ($\sim$ 3000 K) in González-Alfonso et al. (2002), showing effects of shocks. Near-infrared CO spectroscopy of the extended source G318.05+0.09 also revealed its complex structure, including a compact H II region, YSO outflows, and possible supernova ejecta (Onaka et al. 2016).

PDR studies are relevant to recent star- and planet-formation models. In PPDs, molecules are rovibrationally excited, due to intense UV-radiation, hence molecular excitation properties are used to monitor protostellar activity and unveil structures. Highly vibrationally excited CO is found in the inner rim of the disks ($\sim$ 1 AU), while lower-rotational CO lines are commonly observed from the outer disk surfaces ($\sim$ 100 AU) (Kamp et al. 2018; Harsono et al. 2013). For YSOs, rovibrationally excited CO often shows multiple temperature components as a result of varying physical conditions. From the *Herschel*-PACS legacy program, Karska et al. (2017) concluded that for low-mass protostars, lower rotation temperature ($\sim$ 300 K) corresponds to outflow cavity shocks or disk winds, while higher temperatures ($\sim$ 720 K) are associated with irradiated shocks. CO is also one of the best molecules to trace PPD mass and thus the primary molecule used in large PPD surveys (Molyarova et al. 2017; Barenfeld et al. 2017; Ansdell et al. 2018; Schwarz et al. 2018). Furthermore, the $\Delta v = 2$ CO emission overtone is observed in YSOs (Lyo et al. 2017).

Meanwhile, for evolved stars and post-stellar activity, molecules are highly abundant and excited with rich on-going chemistry. Rovibrationally excited CO is observed in both O- and C-rich AGB stars, such as W Hya (Vlemmings et al. 2017) and R Dor (Van de Sande et al. 2017), and used to analyze physical and chemical properties of CSEs (Doan et al. 2017; Kervella et al. 2018; Danilovich et al. 2015). As a bridge molecule, CO is especially of interest for investigating both carbon and oxygen chemistry in AGB stars.

In this chapter, we revisit rovibrational CO excitation, using NLTE modelling with RADEX (van der Tak et al. 2007) and Cloudy (Ferland et al. 2017). To conduct such a study, we construct comprehensive CO *rotational* and *vibrational* collisional rate coefficient data which were previously unavailable. Taking advantage of these data, we perform NLTE spectral analyses of CO in UV-irradiated environments. Models with high astrophysical complexity, such as various PDRs and the extreme carbon star IRC +10216, are also presented.

3.2 Data Construction

For molecular excitation data, we work with the LAMDA Database (Schöier et al. 2005), which provides molecular collisional rate coefficient data for simulating radiative transfer processes in NLTE environments. Currently, CO collisional rate coefficient data is incomplete on the LAMDA database, including only one collider, H_2, in the vibrational ground state. CO rovibrational excitation rate coefficients due to H_2 collisions are also lacking on the BASECOL database (Dubernet et al. 2013). Previous rovibrational CO excitation studies mainly rely on scaling of existing data with various approximation methods (e.g., Thi et al. (2013)), hence limiting the theoretical modelling. Recent advances in quantum calculations give us the opportunity to update CO collisional rate coefficient data up to $v = 5$ and $J = 40$, with three colliders (H_2, H, and He), typically over the temperature range 10-3000 K (details shown in Table 3.1). Calculations for collision rate coefficients were stopped at certain rotational states due to the excessive computational expense for higher Js. There is very little coupling between vibrational manifolds for the gas temperatures considered here.

Transitions will generally move up and down by rotational transitions within a vibrational state. Therefore, the accuracy of the level populations is not compromised except for the very top rotational levels of each vibrational state. In Figure 3.1, we compare band coverages of rovibrational CO collisional rate coefficient data in this work and pure rotational data from Neufeld (2012) (J up to 80) and Yang et al. (2010) (J up to 40), with line spectra. It is emphasized that the rates from Neufeld (2012) are an extrapolation from Yang et al. (2010). We also compare rotation diagrams with rovibrational data and high rotational data in Figure 3.2. Considering the models presented in the lower panel of Figure 3.1, the neglect of the rotational states for $J > 40$ results in a variation in the line flux for $J = 30 \rightarrow 29$ to $J = 40 \rightarrow 39$ ranging from 0.43% to 78.94%, which is comparable to the uncertainties in the actual collisional rate coefficients. The worst case corresponds to the weakest line from the state at the top of our rotational basis.

This available rovibrational collisional data set provides a unique opportunity to study high excitation properties for CO and its application to various astrophysical environments. Demand for high excitation molecular data is continuously growing with the developments in both observation and simulation, especially with the soon-to-be launched JWST. We expect to construct rovibrational excitation data for other molecules, such as CS and CN, in order to create more complete and realistic astrophysical models.

Table 3.1: CO collisional rate coefficient data.

Data	Colliders	J	v
CO-H_2 LAMDA data[a]	H_2	0-40	0
CO LAMDA data updated	H_2 [a,b,c]	0-40	0
		0-20	1-5
	H[d,e]	0-40	0-4
		0-30	5
	He[f]	0-14	0

[a] Yang et al. (2010), [b] Yang et al. (2015),
[c] Castro et al. (2017), [d] Walker et al. (2015),
[e] Song et al. (2015), [f] Cecchi-Pestellini et al. (2002).

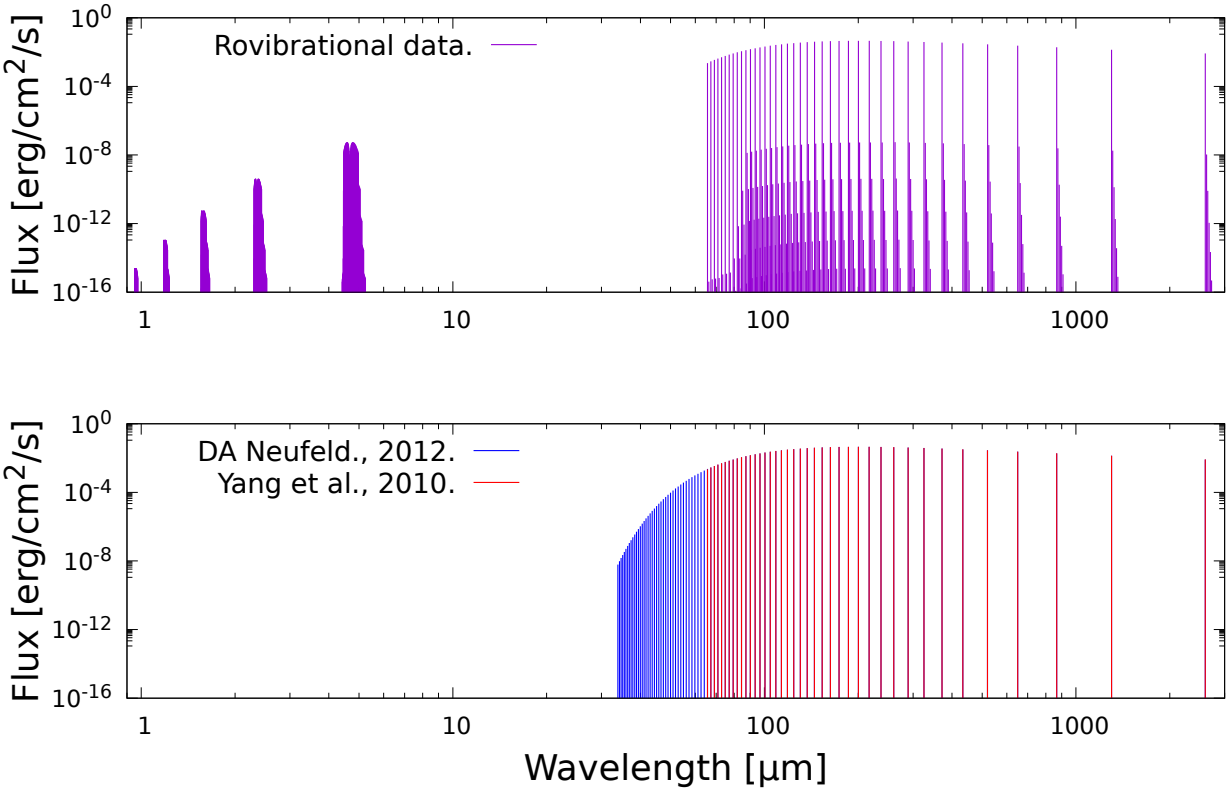

Figure 3.1: CO Full Line Spectra Comparison.

CO full line spectra comparison with rovibrational collisional rate coefficients in this work (top), rotational data from Neufeld (2012) and Yang et al. (2010) (bottom). Conditions: optically thin, isothermal geometry, collider (H_2, H, and He) density of 10^8 cm^{-3}, column density of 10^{12} cm^{-2} and kinetic temperature of 1000 K.

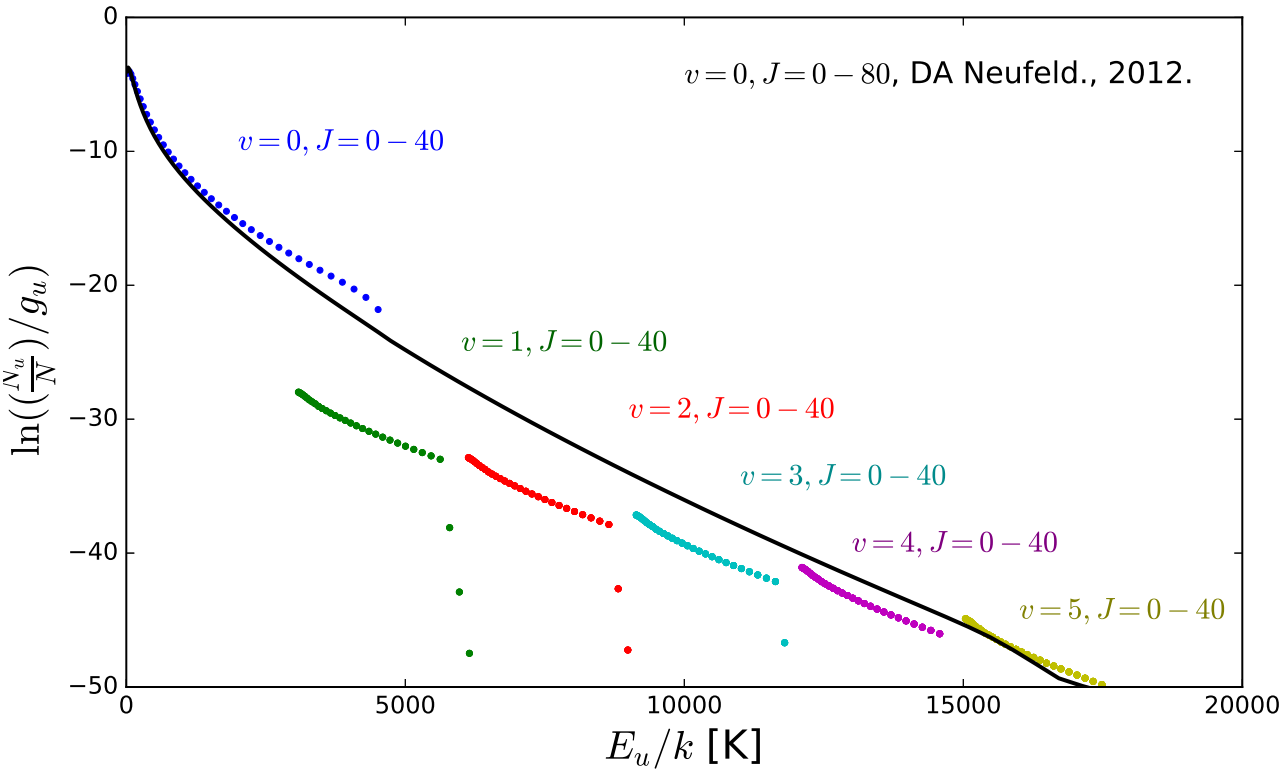

Figure 3.2: CO Excitation Comparison (Data update).

CO rotation diagrams with rotational data from Neufeld (2012) (black solid line) and rovibrational data in this work (colored dots). Condition: optically thin, isothermal geometry, collider (H_2, H, and He) density of 10^4 cm^{-3}, column density of 10^{12} cm^{-2} and kinetic temperature of 1000 K.

3.3 Modelling of astrophysical environments

3.3.1 Spectral Modelling with RADEX

To illustrate CO rovibrational excitation properties with updated collisional rate coefficients, we show one-dimensional NLTE models in homogeneous conditions using RADEX (van der Tak et al. 2007). In the following models, we take the assumptions from Table 1.1, if not otherwise stated.

In high density regions (10^8 cm^{-3}) demonstrated in Figure 3.3, CO is highly rovibrationally excited, up to $\Delta v = 5$, with spectra extending from the near-infrared to the mm range. It is worth noting that the CO fundamental vibrational band intensity could be comparable with high rotational line emission under these given conditions. The pure rotational line spectrum is cut off ~ 65 μm, due to the truncation at $J = 40$ in the data. Figure 3.4 zooms in on the CO fundamental band ($\Delta v = 1$) with density of 10^5 cm^{-3} at 1000 K, colliding with H. For both upper vibrational states, the relative intensities peaks near intermediate J values.

Being a traditional tracer for H_2, CO line ratios are good probes for both H I and H II regions (Enokiya et al. 2017; Tiwari et al. 2018). CO rovibrational line ratios are especially ideal diagnostics in compact and warm regions, which could be attributed to its high excitation energy. Sample line ratio diagnostic plots are shown in Figures. 3.5 and 3.6, as a function of kinetic temperature and collider density. For rotational transitions in the same vibrational level, higher J probes high densities and kinetic temperatures where line ratios become sensitive to temperature with increasing density (approaching LTE). Line ratios between vibrational levels (e.g., for $v = 1$ and $v = 0$, $J = 10 - 14$) are relatively large and more sensitive to density.

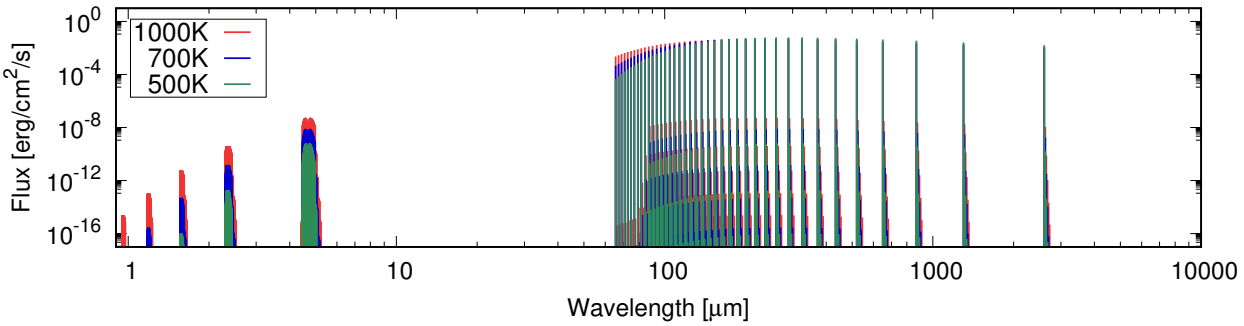

Figure 3.3: CO Full Rovibrational Line Spectra.

CO full line spectra with collider (H_2, H, and He) density of 10^8 cm^{-3} at 500 K, 700 K, and 1000 K (indicated with colors).

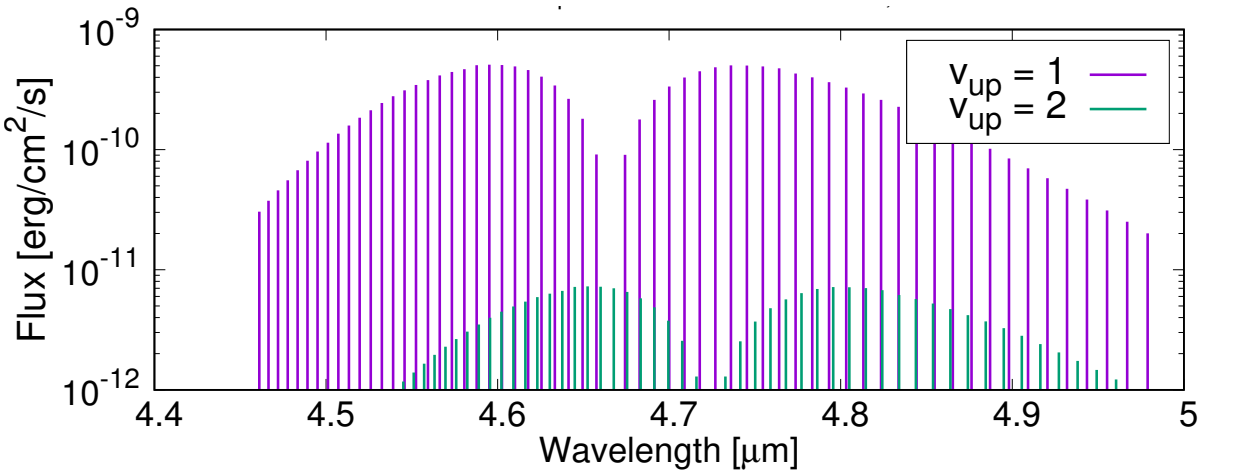

Figure 3.4: CO-H Rovibrational Line Spectrum.

CO-H rovibrational line spectrum, fundamental band ($\Delta v = 1$), with H density of 10^5 cm^{-3} at 1000 K. (Upper vibrational level is indicated with colors.)

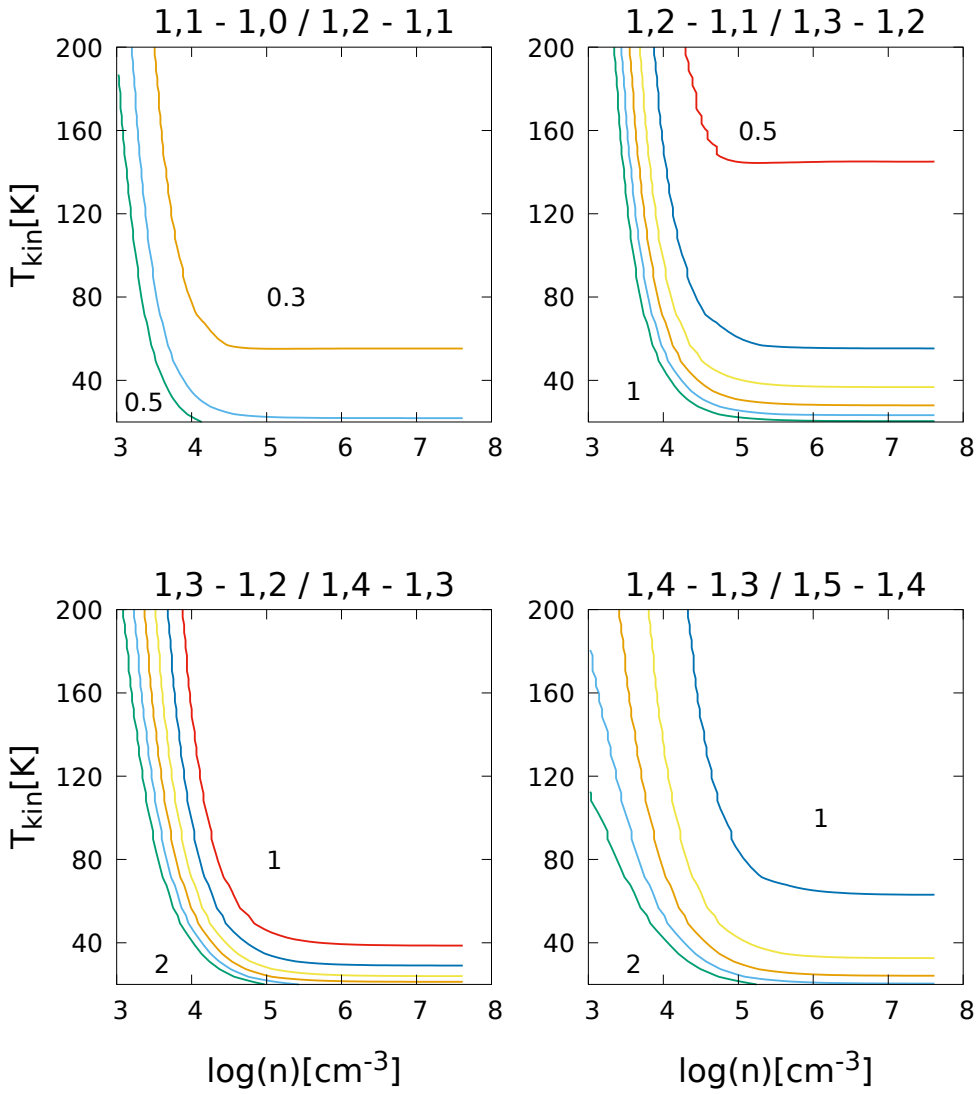

Figure 3.5: CO Diagnostic Line Ratios A

Diagnostic line ratios as a function of kinetic temperature and gas density. (Vibrationally excited ($v = 1$) transitions for a cool environment.) (Notation: $v, J - v', J'$.) Line ratios are as labeled with linear spacing.

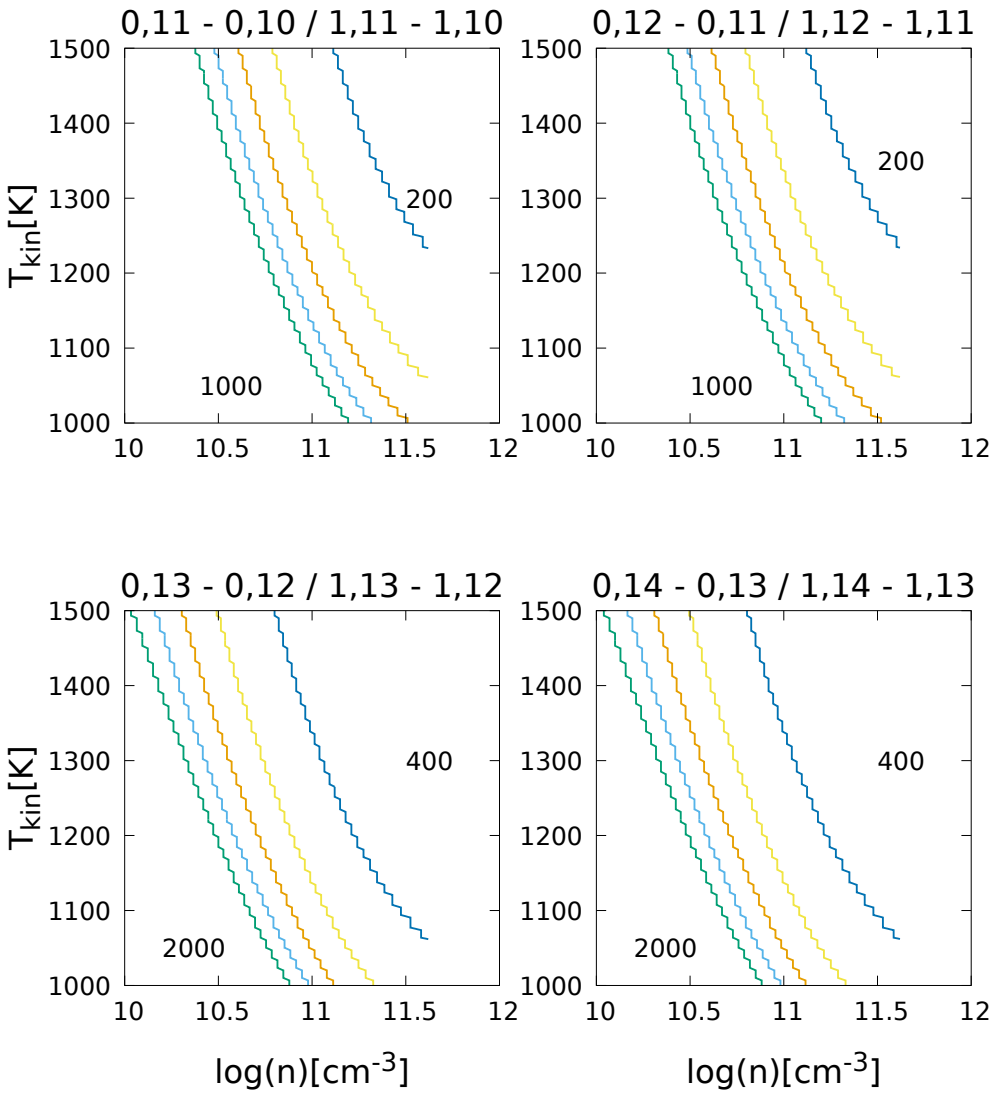

Figure 3.6: CO Diagnostic Line Ratios B

Diagnostic line ratios as a function of kinetic temperature and gas density. (Rovibrational diagnostic line ratios (as indicated) for a warm dense environment.) (Notation: $v, J - v', J'$.) Line ratios are as labeled with linear spacing.

3.3.2 Cloudy modelling of PDRs

3.3.2.1 Leiden Benchmark Models

Molecular collision is one of the main processes responsible for line emission in PDRs (Hollenbach & Tielens 1999), hence we conducted a Cloudy PDR CO survey with rovibrational excitation. Giving a range of representative physical conditions (see Table 1.2), Cloudy Leiden PDR benchmark models were previously utilized to probe various associated ISM properties (Röllig et al. 2007; Zhang et al. 2018).

We explore the two sets of PDR models with both spectra and populations, using the updated CO collisional data. In Figure 3.7, we compare continuum spectra for these models with several strong CO emission lines marked in the zoomed-in view (bottom panel) for the V models. The dust peak near 100 μm is constrained in F models due to the constant gas and dust temperatures, while dust continua show more variances in V models due to self-consistent temperature profiles. In both cases, the CO rotation band is pronounced and may be orders of magnitude above the continuum.

CO rotation diagrams are presented in Figure 3.8, with linear-fit rotation temperatures given as references. With the restricted temperatures, CO excitation is mostly limited within the first two vibrational states for F models. Generally they fit a quasi-LTE pattern (Goldsmith & Langer 1999), except for F4 which consists of two temperature components: lower $\sim$ 40 K and higher $\sim$ 200 K. With constrained gas and dust temperature, the high temperature component for F4 is a consequence of radiative pumping. In the case of V models, with self-consistent temperature profile obtained by solving the heat equation, most vibrational states show multiple temperature components (hotter ones near the radiation source and cooler ones deeper into the PDR). The intense radiation field pumps high rovibrational state populations (up to $v = 5$) in V2 and V4, resulting in a high rotation temperature $\sim$ 500 K.

These results are comparable with our previous rovibrational study on SiO (Zhang et al. 2018). However, being considerably more abundant, CO gives an advantageous view for

estimating physical properties (e.g., for V2 model, CO is excited up to $v = 5$, while SiO only up to $v = 4$ in Zhang et al. (2018)). Pure rotational band emission peaks at mid-range J states for V models due to the cascade from higher vibrational levels following UV pumping from a collisionally hotter $v = 0$ population. Conversely, the intermediate J values for F models follow a quasi-LTE distribution due to a cooler $v = 0$ population at $\sim$ 40 K. In Section 3.3.2.2, we further investigate CO properties in various PDR conditions.

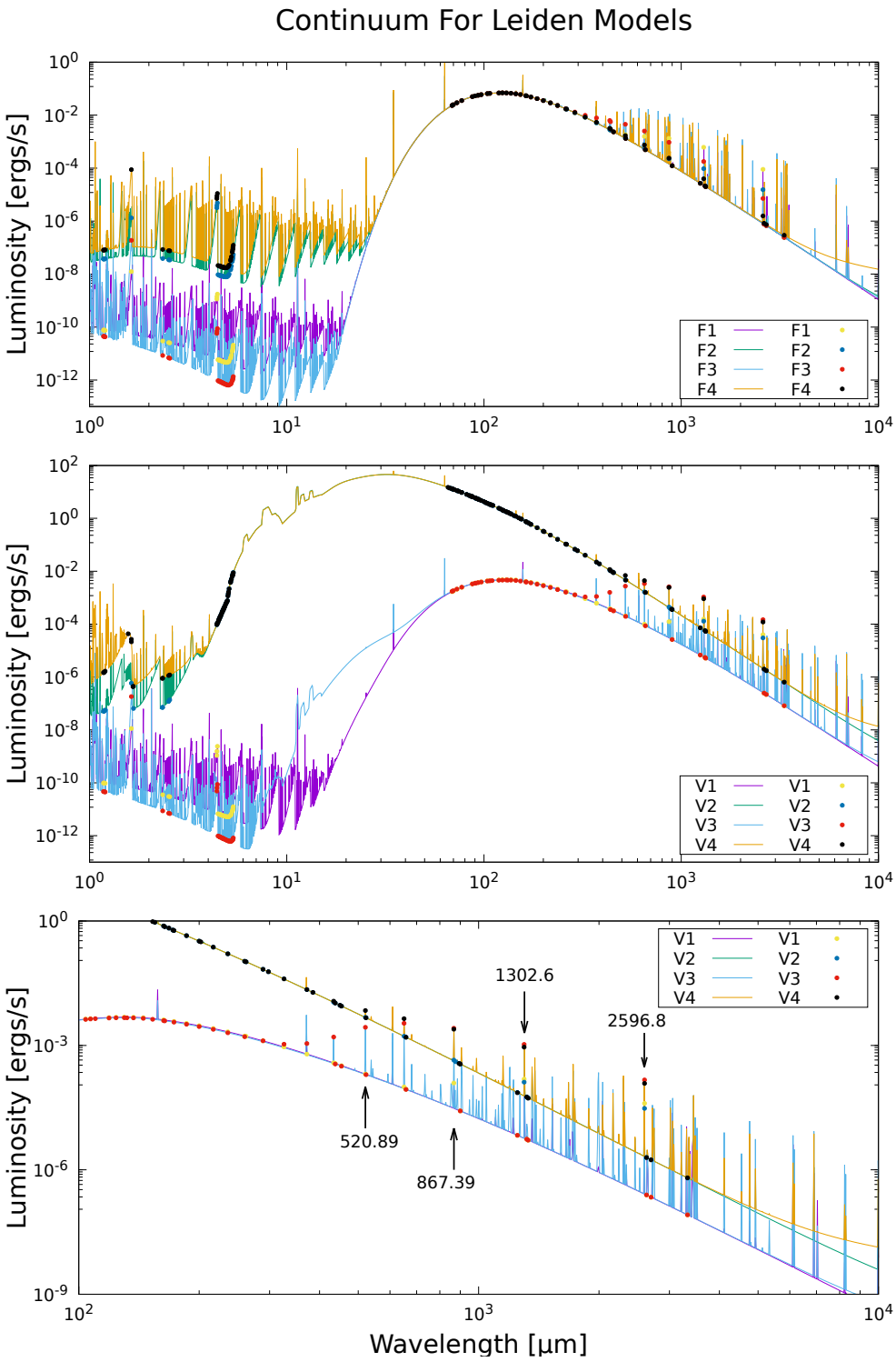

Figure 3.7: PDR Continuum Spectra and CO Emission.

PDR continuum spectra for Cloudy Leiden benchmark models, CO emission lines are marked as dots, several examples shown with wavelengths in the bottom panel are (in the notation of $v, J \rightarrow v', J'$): 2596.8 μm (0, 1 $\rightarrow$ 0, 0); 1302.6 μm (0, 2 $\rightarrow$ 0, 1); 867.39 μm (0, 3 $\rightarrow$ 0, 2); 520.89 μm (0, 5 $\rightarrow$ 0, 4). Other line features are due to various atomic and molecular species.

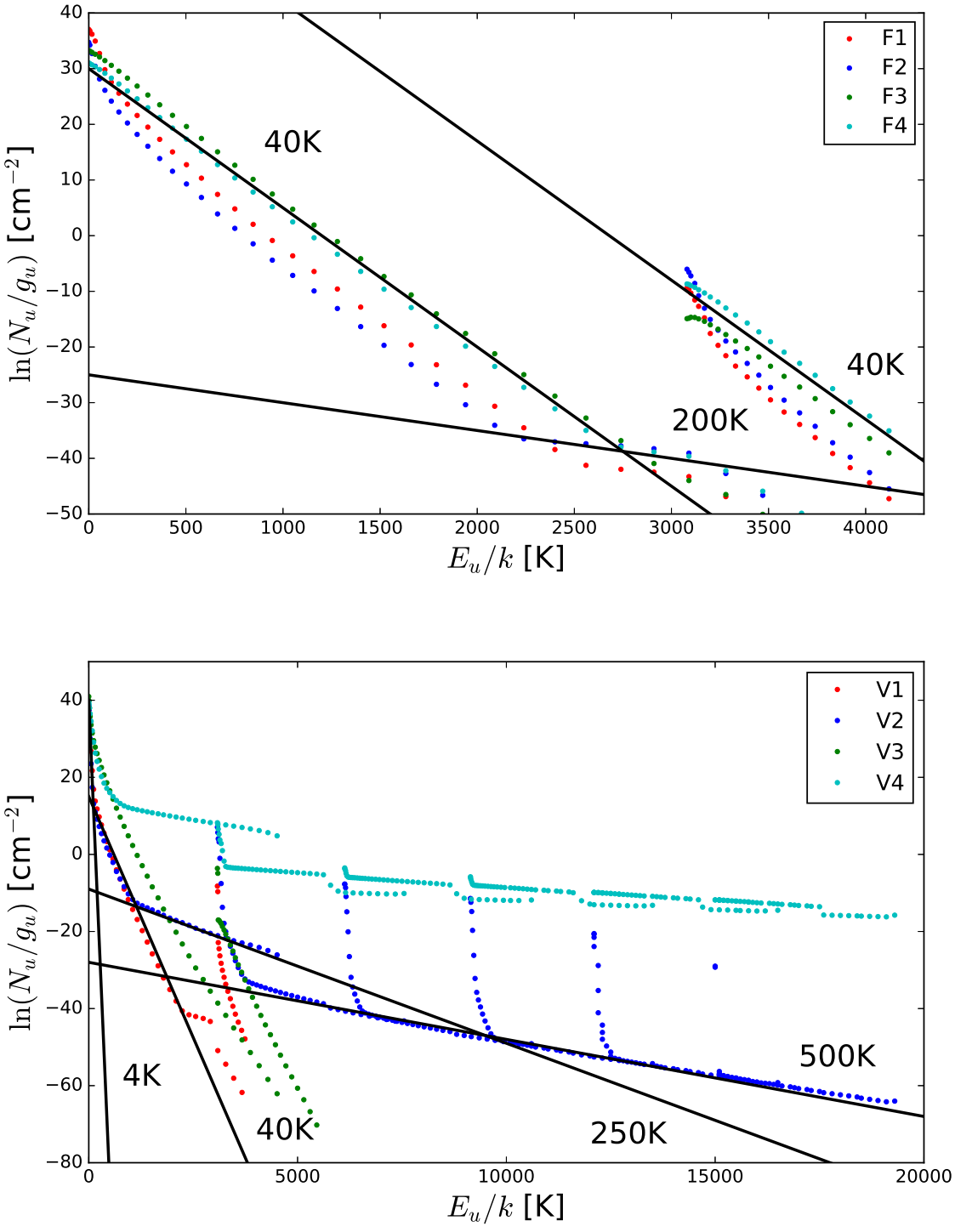

Figure 3.8: CO Rotation Diagram for Cloudy Leiden PDR models.

CO rotation diagram for Cloudy Leiden PDR models. Reference LTE models are indicated with solid lines.

3.3.2.2 Cloudy PDR Grids

In order to further investigate molecular excitation properties in UV-irradiated environments, here we present radiation-temperature and radiation-density grid results for PDR models using Cloudy. CO diagnostics have been presented by other authors, for example for PPDs (Kamp et al. 2011), but has far as we are aware, these are limited to rotational transitions in $v = 0$.

In Figures. 3.9 and 3.10, we extended Leiden benchmark PDR models (shown in Section 1.3.2) with parameter grids (temperature- and density-radiation), and give rotation diagrams for both CO and SiO (see Chapter 2). CO is more abundant and formed closer to the radiation front than SiO in PDRs and therefore may sample different regions.

Figure 3.9 is a set of rotation diagrams varying gas temperature (20 - 100 K) and FUV radiation (units of 10 - 10^5 Draine) with uniform density of $10^{5.5}$ cm^{-3} and dust temperature of 20 K (corresponding to Leiden PDR F models). CO presents level population trends closer in agreement with reference LTE temperature profiles than SiO, with excitation up to $v = 3$. With lower rovibrational excitation energy, SiO is excited up to $v = 5$ with multiple temperature components. Overall, constant temperature constrains the excitation energy and radiation pumps the individual levels.

Corresponding to Leiden PDR V models, Figure 3.10 is a set of rotation diagrams with gas density of $10^{3.5}$ - $10^{7.5}$ cm^{-3} and FUV radiation of 10 to 10^5 Draine, with self-consistent temperature profiles. At low density ($10^{3.5}$-$10^{4.5}$ cm^{-3}) and intense radiation field (10^4-10^5 Draine), CO excitation is highly sensitive to the radiation intensity and shows two temperature components for each vibrational level, indicating diagnostic power of rovibrational excited CO in such environments. Both molecules approach LTE with increasing density and radiation (lower limit around $10^{6.5}$ cm^{-3} and 10^4 Draine).

We also constructed CO rovibrational diagnostic spectral line ratios and show example sets in Figures. 3.11, 3.12 (PDR F models, Figure 3.9) and 3.13 (PDR V models, Figure 3.10). Zooming in to low radiation intensity range (10 - $\sim 10^2$ Draine field, Figures. 3.11 and

3.12), CO emission line ratios can serve as good diagnostics for radiation intensity. While with more intense radiation ($\sim 10^2$ - $\sim 10^3$ Draine field, Figures. 3.11 and 3.12), the gas approaches LTE with low temperatures (constrained by constant temperature models) and line ratios become temperature probes. Line ratios for radiation and density (Figure 3.13) show more complex structures within the demonstrated ranges, which may be more versatile for specific conditions. For instance, line ratios for rotational lines in $v = 2$, are largest for a combination of intense irradiation and low density, while for low-lying rotational transitions in $v = 0$, the line ratios are insensitive to radiation field.

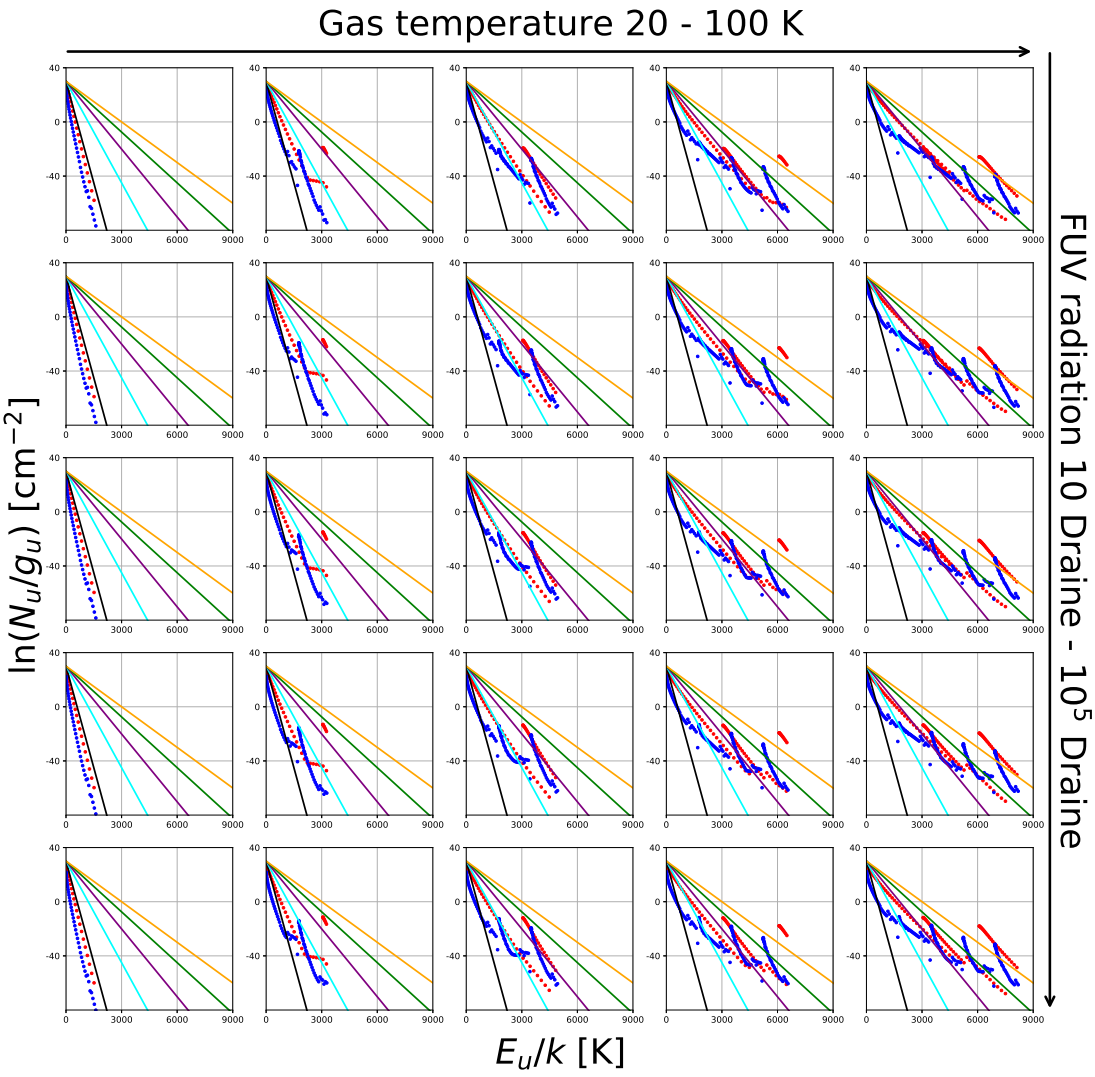

Figure 3.9: PDR Temperature - Radiation Grid Rotation Diagrams.

CO (red symbols) and **SiO** (blue symbols) rotation diagrams for PDRs with constant gas temperature 20 K - 100 K and FUV 10 - 10^5 Draine field (other parameters correspond to Leiden PDR F models). LTE reference distributions marked as 20 K, 40 K, 60 K, 80 K, and 100 K, bottom to top.

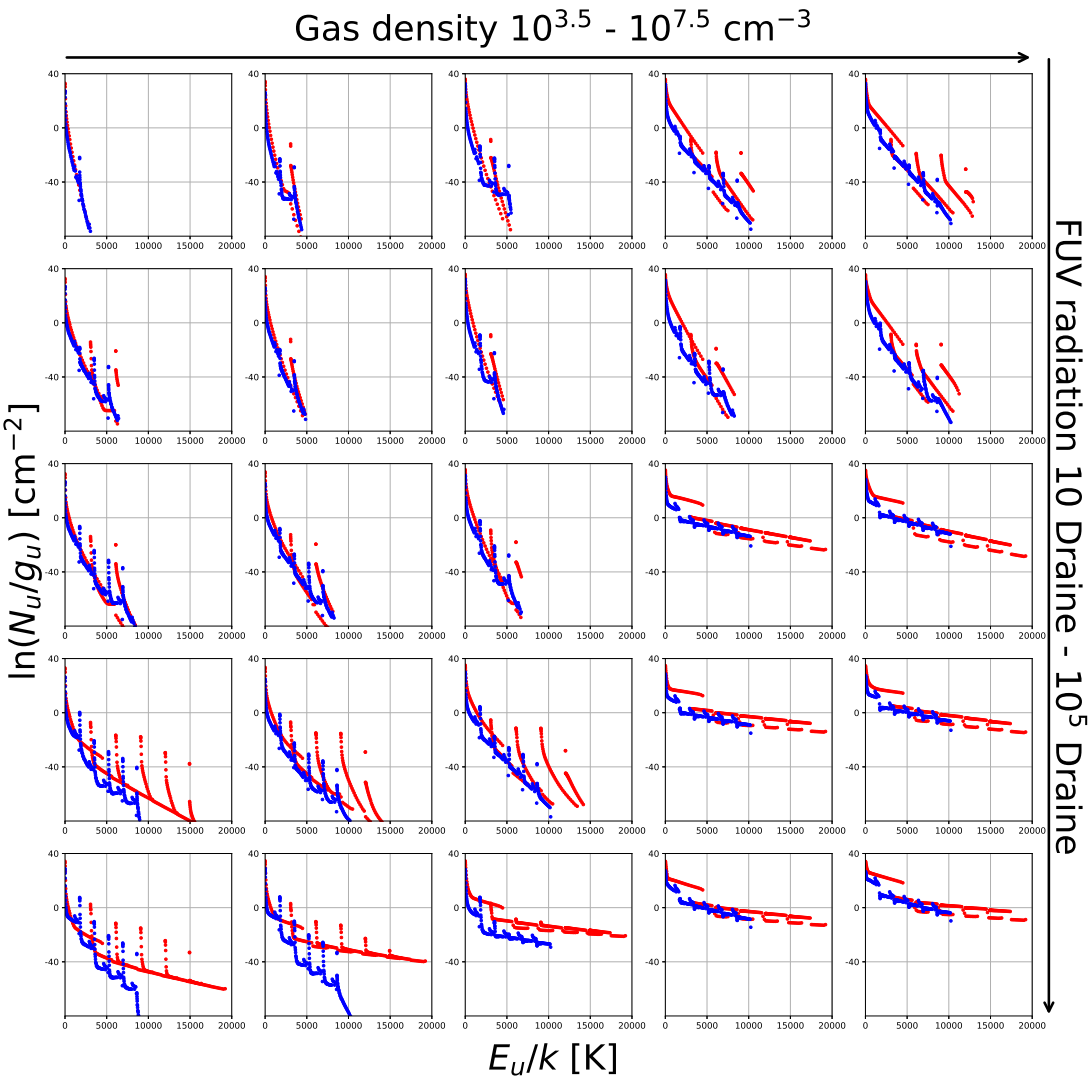

Figure 3.10: PDR Density - Radiation Grid Rotation Diagrams.

CO (red symbols) and SiO (blue symbols) rotation diagrams for PDRs with constant gas density $10^{3.5}$ - $10^{7.5}$ cm^{-3} and FUV 10 - 10^5 Draine field (other parameters correspond to Leiden PDR V models).

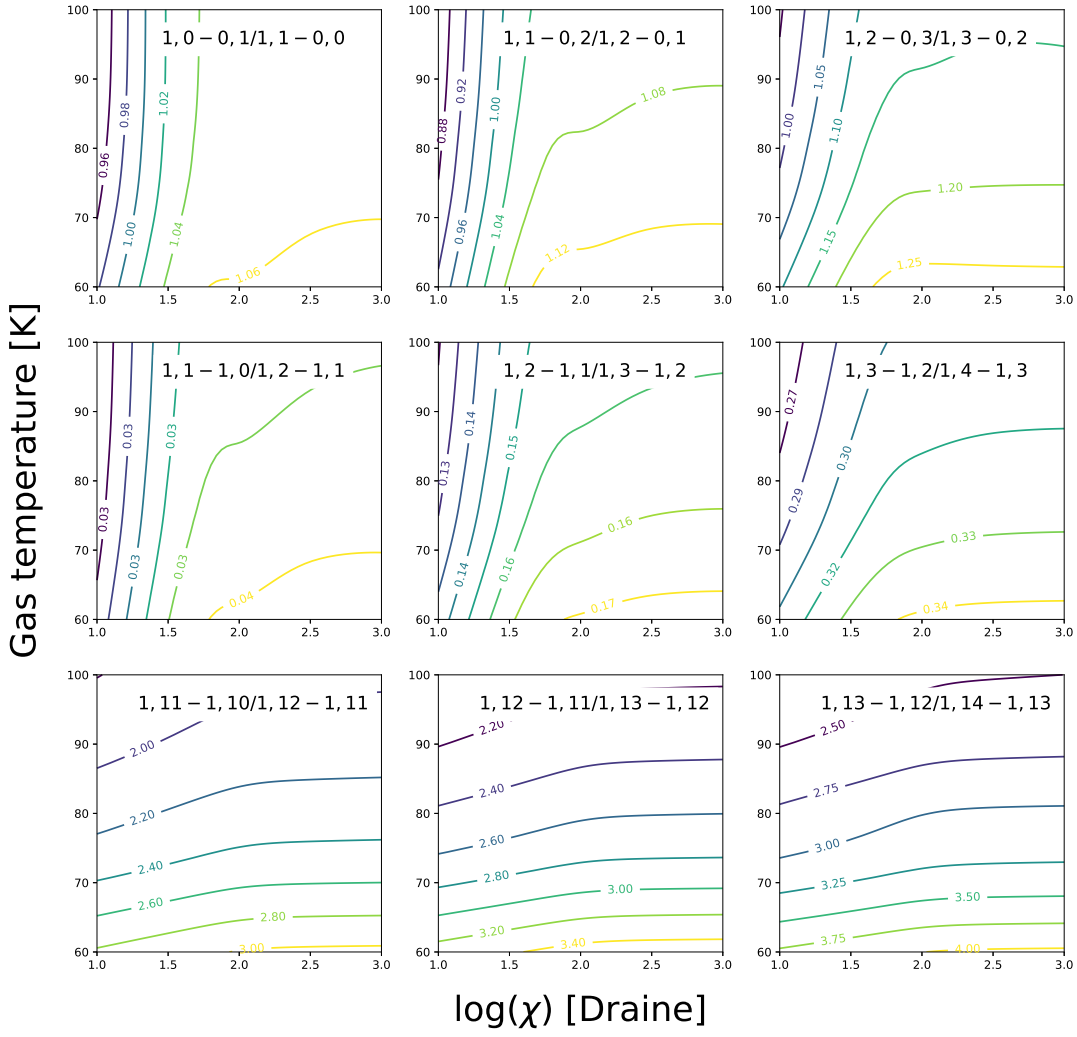

Figure 3.11: PDR Temperature - Radiation Grid Diagnostic Line Ratios A.

CO line ratio as a function of FUV radiation and gas temperature (60 K - 100 K) in PDRs (Notation: $v, J - v', J'$.). Other parameters similar to Leiden PDR F models.

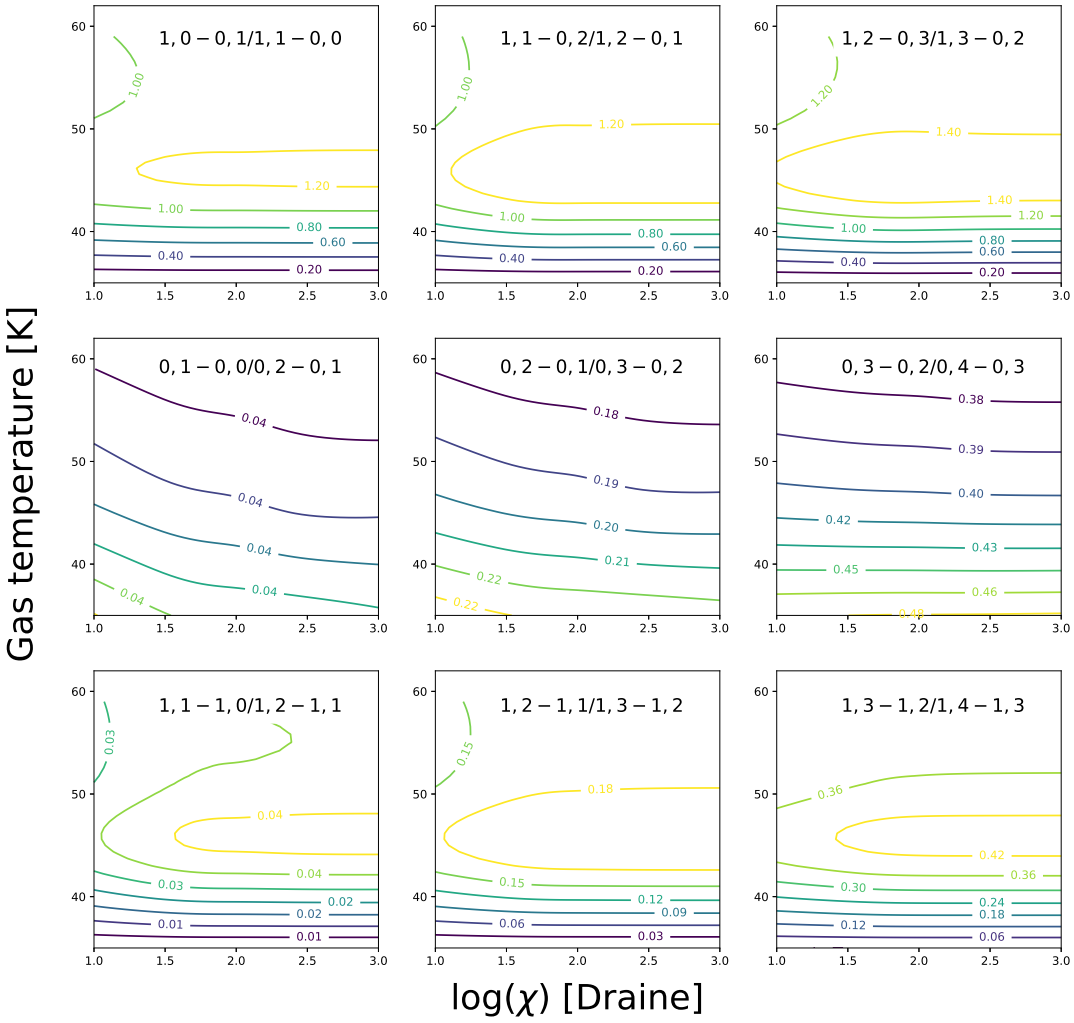

Figure 3.12: PDR Temperature - Radiation Grid Diagnostic Line Ratios B.

CO line ratio as a function of FUV radiation and gas temperature ($\sim$ 40 K - $\sim$ 60 K) in PDRs (Notation: $v, J - v', J'.$). Other parameters similar to Leiden PDR F models.

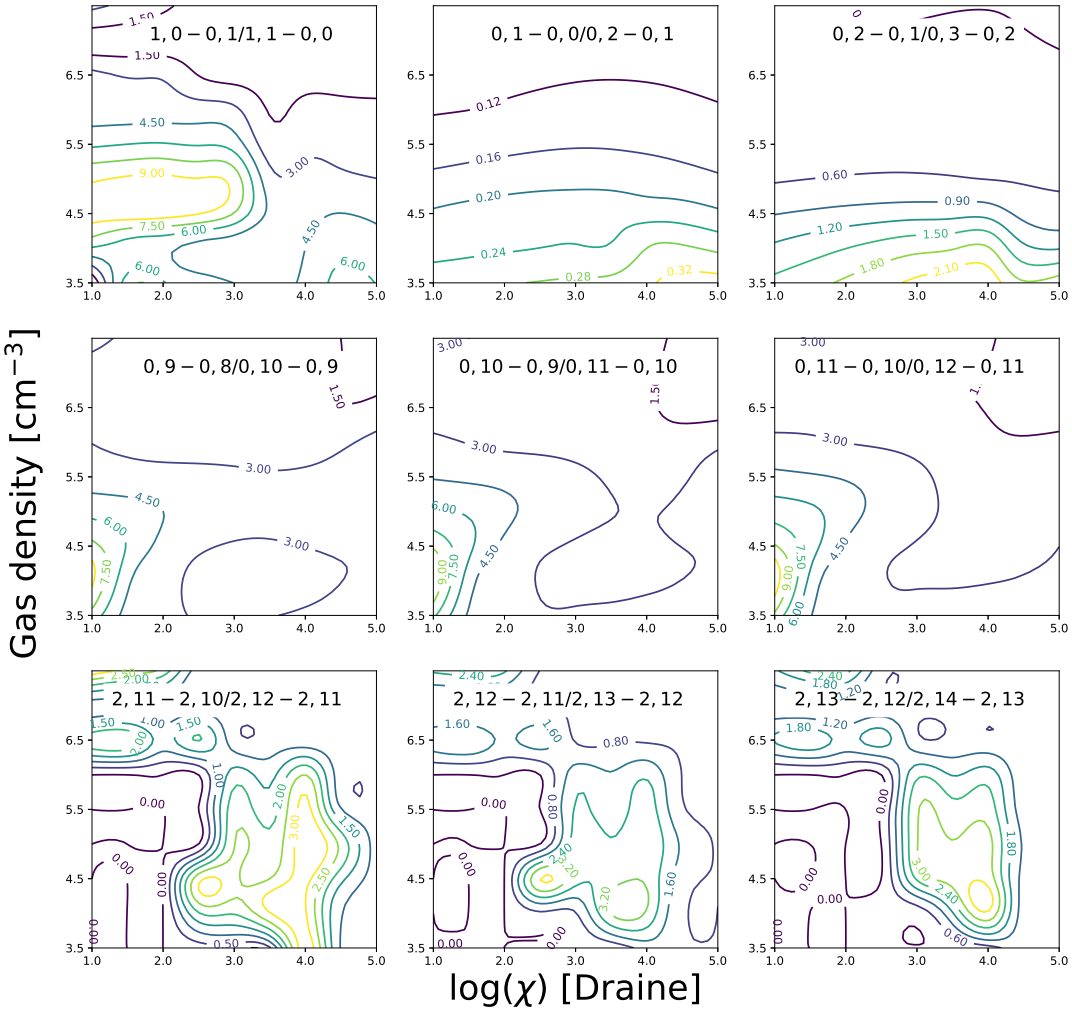

Figure 3.13: PDR Density - Radiation Grid Diagnostic Line Ratios.

CO line ratio as a function of FUV radiation and gas density in PDRs (Notation: $v, J - v', J'$.). Other parameters similar to Leiden PDR V models.

3.3.3 Cloudy modelling of IRC +10216

Given the strong chemical bond, in most AGB envelopes, CO is warm and abundant (Decin 2012; Ramos-Medina et al. 2018; da Silva Santos et al. 2018). While CO analyses being essential for all three types of AGB stars, we focus on the carbon star IRC +10216 in this work.

The well-studied IRC +10216 is embedded in a late-stage gaseous and dusty envelope. Its high flux in the infrared allows extensive inspection of chemical contents and dynamics. Recent detection of time-dependent molecular emission variance within the envelope suggested shock-related dissociation effects (Fonfría et al. 2018a,b). Adapting the new CO rovibrational collisional rate coefficient data set, we attempt to construct a time-independent NLTE Cloudy model including realistic physics and chemistry for IRC +10216, focusing on CO excitation. The chemistry network is discussed in detail in (Ferland et al. 2017). Model parameters are based on De Beck et al. (2010); Li et al. (2014) and Fonfría et al. (2017), and are shown in Table 3.2.

We obtained archival observation data from the NASA/IPAC Infrared Archive [2], including ISO-SWS spectrum (OBSID 19900101; 1996-06-02) (Cernicharo et al. 1999; Sloan et al. 2003) and Herschel-PACS spectra (OBSID 1342253754; OD 1257; 2012-10-21) (Cernicharo et al. 2014). Observational spectra and simulation results are shown in Figure 3.14.

The thick dust shell for this "extreme carbon star" present two unique features: ~ 11 μm could be contributed to SiC and other carbon molecular bands such as C_2H_2 (Yang et al. 2004), and ~ 30 μm is possibly MgS (Hony et al. 2002). Such features tend to appear among late-stage carbon stars, but are yet to be fully understood. In our current model, we do not include SiC and MgS dust grains due to the limited knowledge of these two features in carbon stars. Further discussion of the dust composition and hydro-carbon molecules in carbon stars is beyond the scope of this thesis. The interested readers can consult Messenger et al. (2013), Agúndez et al. (2012), and Fonfría et al. (2018b). Hence, we consider the simulated spectrum

[2] https://irsa.ipac.caltech.edu/frontpage/

to be a reasonable fit. With the high C/O ratio and late evolved-stage, it is expected that the majority of oxygen is locked in CO. Whether there is enough oxygen to be partially preserved in silicates is still under debate, thus we neglect silicates in our model as well. We marked a few CO line emissions in Figure 3.15, including vibrational excited lines (e.g.,$1, 3 \rightarrow 1, 2$ and $5, 4 \rightarrow 5, 3$). Vibrational CO excitation has been previously detected and discussed in Patel et al. (2009), suggesting radiative pumping. Rotational CO emission lines in the vibrational ground state (e.g.,$0, 4 \rightarrow 0, 3$) could be blended with stronger emission from other species.

CO excitation analysis could lead to better understanding of both carbon and oxygen chemistries in AGBs. From the CO rotation diagram Figure 3.16, we deduced the rotational temperatures for different vibrational states to cover the range $\sim$ 300-400 K with an increasing trend, and the vibrational temperature for $J = 0$ to be $\sim$ 440 K. The vibrational ground state appears to be composed of two temperature components: $\sim$ 260 K ($J \leq 25$) and $\sim$ 360 K ($J \geq 25$). The deduced excitation temperatures are consistent with a recent study on carbon-chemistry with rovibrationally excited C_2H_2 from Fonfría et al. (2018b). The CO rotation diagram indicates rotational LTE behavior for all vibrational levels (while not in rovibrational LTE, since rotation and vibration temperatures show $\sim$ 100 K difference), reflecting the high density and the circumstellar environment (e.g., intense radiation due to the star and reprocessed dust emission) within IRC +10216. Lack of rovibrational excitation consideration would limit the modelling of such extreme environments.

Table 3.2: Parameters for NLTE IRC +10216 Model.[a]

Model parameters	Values
Geometry & Dynamics	Static Sphere
Background	Galactic cosmic rays & Cosmic microwave
R_{inner}: Inner radius (cm)	$10^{15.1}$
T: Stellar temperature (K)	2330
L: Luminosity ($L_{\odot}$) [b]	1.13×10^4
n: Density (cm^{-3}) [c]	10^8
l: Distance (pc)	150
T_{end}: Temperature cut-off (K) [d]	180
d_{min}: Minimum dust size (μm)	0.001
d_{max}: Maximum dust size (μm)	0.025

[a] Gas-phase chemical abundance: ISM.
Dust composition: astronomical graphite (late-stage carbon star with a thick dusty shell), 1.5 times the default abundance.
For additional details see Van Hoof et al. (2004) .
[b] Power law index: -2.5 for ratio 0.1 at 0.01 Ryd.
[c] Power law index: -2. [d] Fonfría et al. (2017).

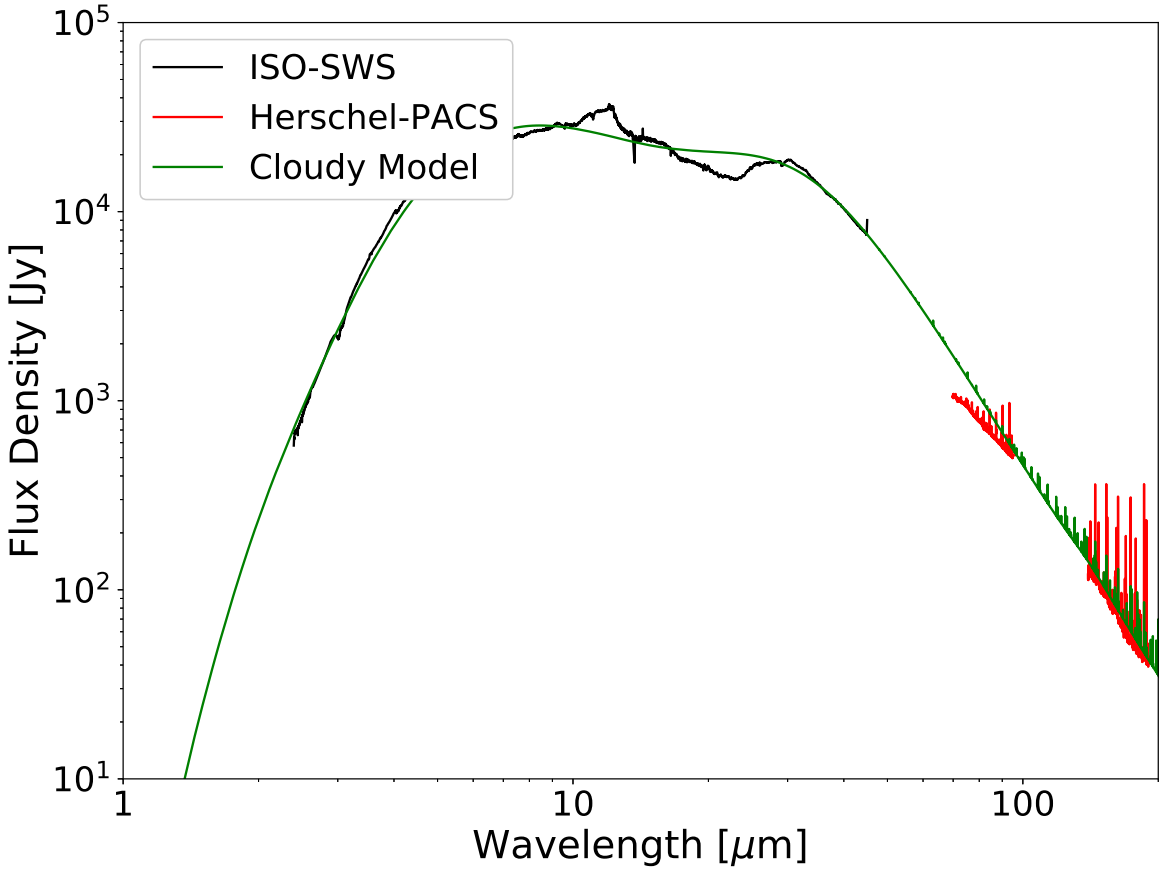

Figure 3.14: Continuum Spectrum for IRC +10216.

Simulated continuum spectrum of IRC +10216 (green), ISO-SWS spectrum (OBSID 19900101; 1996-06-02) (Cernicharo et al. 1999; Sloan et al. 2003): 2.39520 μm - 45.07800 μm (black), and Herschel-PACS spectra (OBSID 1342253754; OD 1257; 2012-10-21) (Cernicharo et al. 2014): 69.796 μm - 105.181 μm & 139.557 μm - 210.269 μm (red).

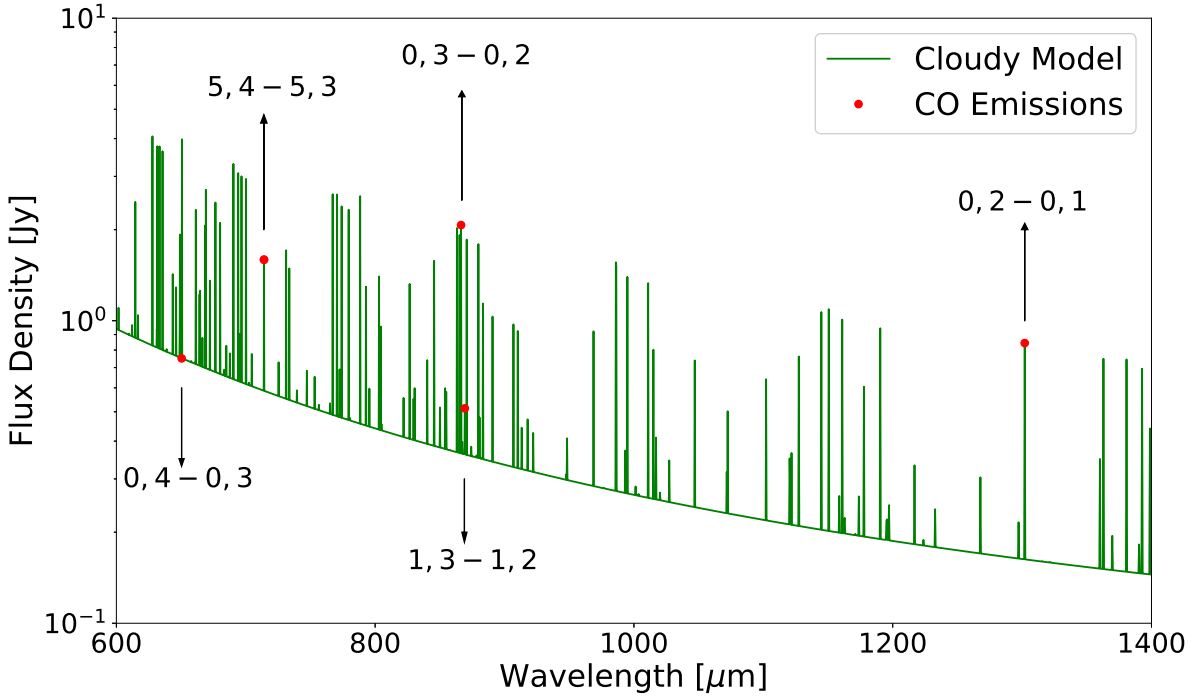

Figure 3.15: Zoomed-in view for molecular emission in IRC +10216.

Simulated continuum spectrum of IRC +10216 (green), with CO emission marked as red dots. (Transition notation: $v, J-v', J'$.) $1,3-1,2$ and $5,4-5,3$ (vibrationally excited) are intense, while $0,4-0,3$ (vibrational ground state) is blended.

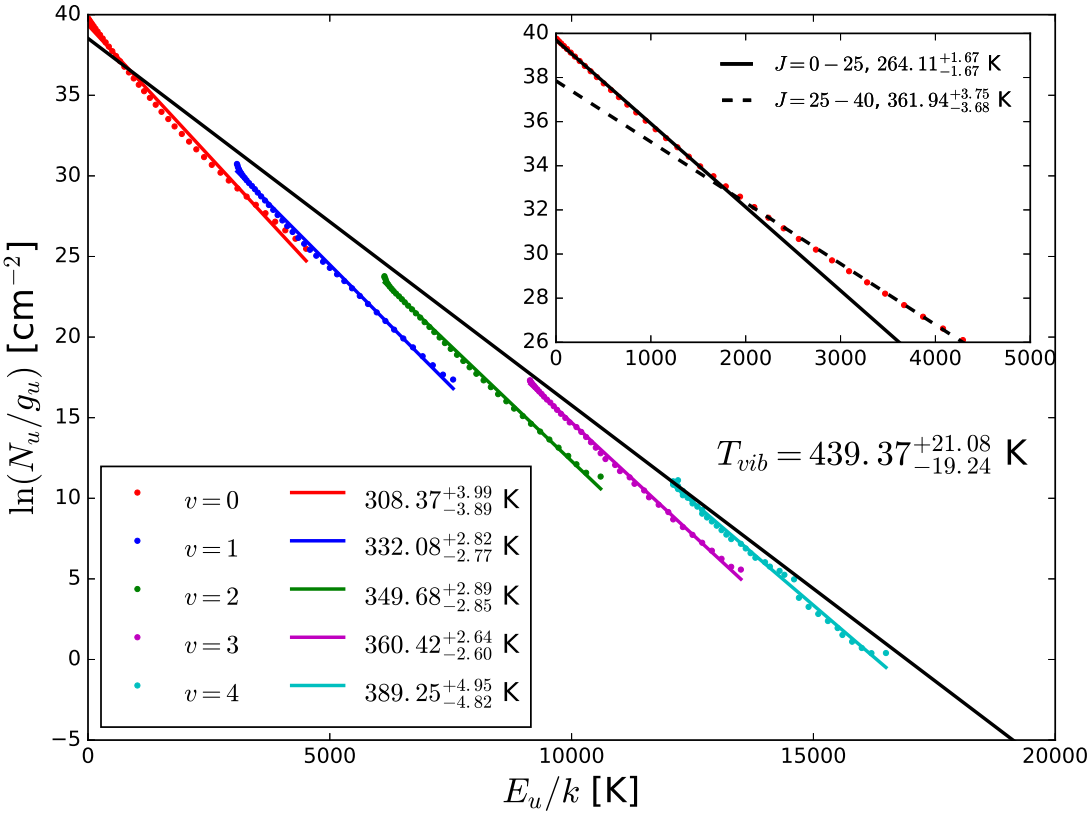

Figure 3.16: CO Rotation Diagram for IRC +10216.

CO rotation diagram for the carbon star IRC +10216. Deduced rotational and vibrational temperatures are indicated with solid lines. Rotational temperatures for different vibrational states is ~ 350 K and the vibrational temperature for $J = 0$ is ~ 440 K. Vibrational ground state (zoomed-in upper right) shows two temperature components: ~ 260 K ($J \leq 25$) and ~ 360 K ($J \geq 25$).

3.4 Summary and Discussion

Here we investigated rovibrational CO excitation in UV-irradiated environments, with comprehensive collisional rate coefficient data. With RADEX, we simulated simple environments and constructed line spectra and diagnostic plots. While with Cloudy, we looked into CO behaviour in PDRs and IRC +10216. Preliminary results are as follows:

- From state-of-the-art quantum calculations, we construct a CO rovibrational collisional rate coefficient data set up to $v = 5$ and $J = 40$, with three colliders: H_2, H, and He. The data are available in LAMDA and BASECOL format from the authors or from the UGA Molecular Excitation Database[3]. Such data allow for the theoretical study of molecular rovibrational excitation in NLTE environments. We plan to enhance the high excitation database by compiling rovibrational excitation data for other molecules of interest, such as CS and CN.

- Given sufficient physical conditions (such as density, temperature, and incident radiation), rovibrational band emission is intense and comparable to pure rotational lines. Line intensity ratios between different rovibrational states offer additional diagnostics.

- In PDRs, molecules are rovibrationally pumped by UV radiation. CO could be highly excited, resulting in intense line emission. In typical PDR environments, CO presents multiple temperature components ($\sim$200-500 K near the radiation source, and $\sim$40 K deeper into the cloud). With its substantial abundance, CO rovibrational excitation properties are an especially valuable probe of PDRs. With temperature, density, and radiation dependent grid models, we further investigated UV-irradiated regions and demonstrate the potential diagnostic power of rovibrationally excited CO (see Appendix). In these general PDRs, level populations are evidently radiatively pumped. While at low density and highly irradiated environments, CO excitation is explicitly sensitive to the density and radiation field of the gas, presenting strong NLTE effects.

[3] www.physast.uga.edu/amdbs/excitation/

- We constructed a detailed NLTE Cloudy model for the carbon star IRC +10216 including a self-consistent treatment of gas and dust temperature, chemistry, radiative transfer, and dust opacity. The resulting rovibrational CO excitation properties in its CSE were studied. CO is exceptionally excited, resulting in a consistent rotational temperature ∼350 K and vibrational temperature ∼440 K. Vibrationally excited line emission is identified in the continuum spectrum. Such models may help reveal more details of the structure and composition of the CSEs.

Chapter 4

Properties of Highly Rotationally Excited H_2 in Photodissociation Regions[1]

[1] Zhang, Ziwei E., Cummings, Sally J., Wan, Yier, Yang, Benhui, and Stancil, Phillip C. Submitted to *The Astrophysical Journal*, June 9, 2019.

4.1 Introduction

In the interstellar environments, molecular hydrogen is the dominant molecular species while being crucial for the thermal balances (Field et al. 1966; Carruthers 1970; Shull & Beckwith 1982; Shaw et al. 2005). Rotational, vibrational, and electronic H_2 emission or absorption have all been observed in the ISM, covering from UV to the infrared (Burton 1992; Flower 2007). Most H_2 emission originates from PDRs, where FUV radiation pumps hydrogen both electronically and rovibrationally. Relative line intensities are highly dependent on the physical conditions, such as density and incident radiation (Hollenbach & Tielens 1997). Therefore, H_2 provides important spectral diagnosis in PDR-related astrophysical contexts, such as star-forming regions (Evans 1999; O'dell 2001; McKee & Ostriker 2007). H_2 is also the primary molecular coolant in the early universe and contributes to early star formation (Lepp et al. 2002).

In highly UV-irradiated regions (such as PDRs), H_2 is in non-local thermal equilibrium (NLTE), where molecular excitation is not dominated by collisions and we need to account for all possible excitation levels. Theoretical studies regarding molecular excitation properties in NLTE conditions require collisional rate coefficients, while high rotational data for H_2 - H_2 collision was previously sparse. Recent theoretical calculations for H_2 collisional rates have been and will continue to further our understanding of molecular micro-processes in UV-pumped gas.

Taking advantage of new calculations for high rotational H_2 - H_2 collision rates up to the dissociation limit ($v = 0, J = 31$) (Wan et al. 2018), we investigate H_2 excitation properties in a range of astrophysical environments, with the focus on PDRs.

4.2 H_2 Collisional Data

Two H_2 collisional datasets are constructed for NLTE simulations. Previously, H_2 was only taken as the collision partner in the LAMDA database, and its collisional rate coefficients

were not available. We constructed comprehensive H_2 collisional rate data in LAMDA format with multiple colliders (H_2, He, H, and H^+) and extensions to high temperature (see Table 4.1). In particular, high rotational data (J up to 31) for H_2 - H_2 collisions is adapted from new quantum calculations (Wan et al. 2018). Example full rovibrational line spectra generated by this data set is demonstrated in Figure 4.1.

Table 4.2 lists the update of the Cloudy H_2 collisional rates database. (For more information about Cloudy, see Section 1.3 and Ferland et al. (2017).) Currently, Cloudy includes H_2 - H_2 collisional rates for $J < 9$ (Lee et al. 2008), with the g-bar approximation used for higher Js (van Regemorter 1962; Shaw et al. 2005).

For details on related quantum calculations, please refer to Wan et al. (2018), Lique (2015), Lee (2007), Lee et al. (2008), and Gerlich (1990). With these datasets, we conduct NLTE H_2 spectral analyses in: i) uniformed environments, ii) general PDRs, and iii) a detailed study of the Orion Bar.

Table 4.1: H_2 LAMDA data.

Collider	J cut-off	v cut-off
para-H_2[a]	31	0
ortho-H_2[a]	31	0
He[b]	3	14
H[c]	8	3
H^+[d]	9	0

[a] Wan et al. (2018),[b] Lee (2007), [c] Lique (2015)
[d] Gerlich (1990).

Table 4.2: H_2 - H_2 rotational data update in Cloudy ($v = 0$).

Data	J cut-off
Current (ORNL)[a]	8
Update[b]	31

[a] Lee et al. (2008) (36 temperatures points),
[b] Wan et al. (2018) (64 temperatures points).

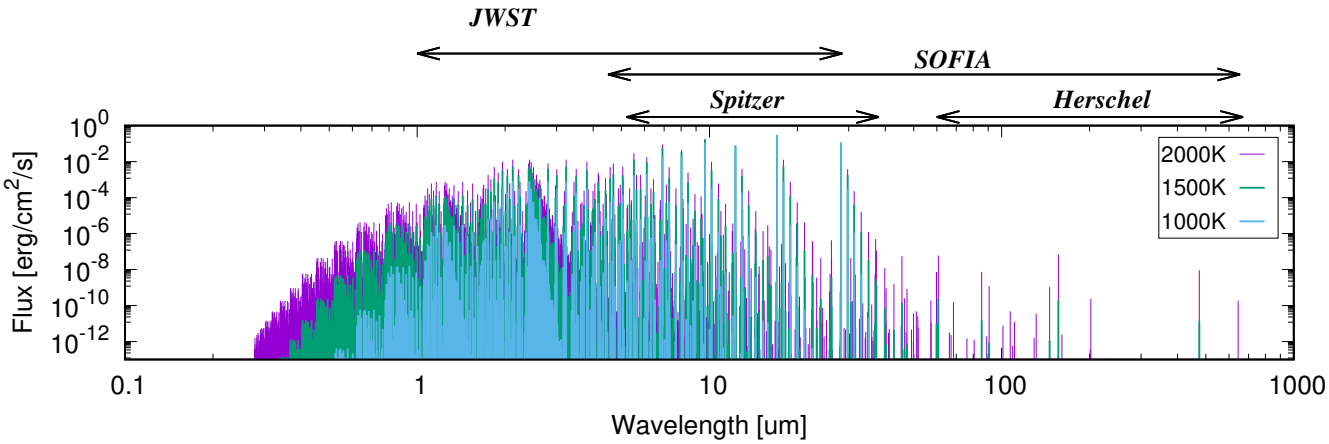

Figure 4.1: Full Rovibrational Line Spectra of H_2

Full rovibrational line spectra of H_2 in uniform environments, with multiple colliders (H_2, H, and He) and a density of 10^8 cm^{-3}. Gas temperature of 1000 K, 1500 K, and 2000 K are indicated with colors.

4.3 Uniform NLTE Simulation

For uniform conditions, we set up one-dimensional NLTE models with RADEX (van der Tak et al. 2007). The simulations in this section applies the rovibrational H_2 LAMDA dataset with the assumptions (if not otherwise stated) in Table 1.1.

In LTE environments, molecular level populations follow a Boltzmann distribution (Goldsmith & Langer 1999; Rybicki & Lightman 1979; Andrews 2010; Zhang et al. 2018). In Figure 4.2, we use rotation diagrams, to show the evolution of H_2 level populations ($v = 0$), with varying temperature and density. Para- (even J) and ortho-H_2 (odd J) are well separated and show parallel trends. Given sufficient density ($\sim 10^{10}$ cm^{-3}), the level populations approach LTE quickly with increasing temperature and often show uniform gradients which correspond to the gas temperatures. A few intermediate para rotational states are not shown, as their populations are extremely small (700 K and 1000 K). While at the relatively high temperature of 2000 K, level populations for low density conditions often split into two components, separating around $J = 18$. High J excitations are very sensitive to density, leading to the break of LTE trends, which may be attributed to the requirement for high H_2 excitation energy.

From Figure 4.1, we zoom in the predicted spectrum for three H_2 line emission bands: $\Delta v = 0$, $\Delta v = 1$, and $\Delta v = 2$, shown in Figure 4.3. For both rotational and vibrational spectra, the relative intensity peaks at mid-J. Such spectral predictions could provide us diagnostic information about the physical conditions, such as density and temperature, of the cloud. For instance, line emission ratios are an effective diagnostic technique used for observations. Figure 4.4 is a set of rotational line ratio plots as as a function of density and kinetic temperature, given the typical molecular cloud environments. Overall, line ratios are density probes in low density regions, and temperature probes in denser regions where the gas is approaching LTE. Ratios of higher J transitions, though having considerably larger values, show better diagnostic properties for hotter and denser environments.

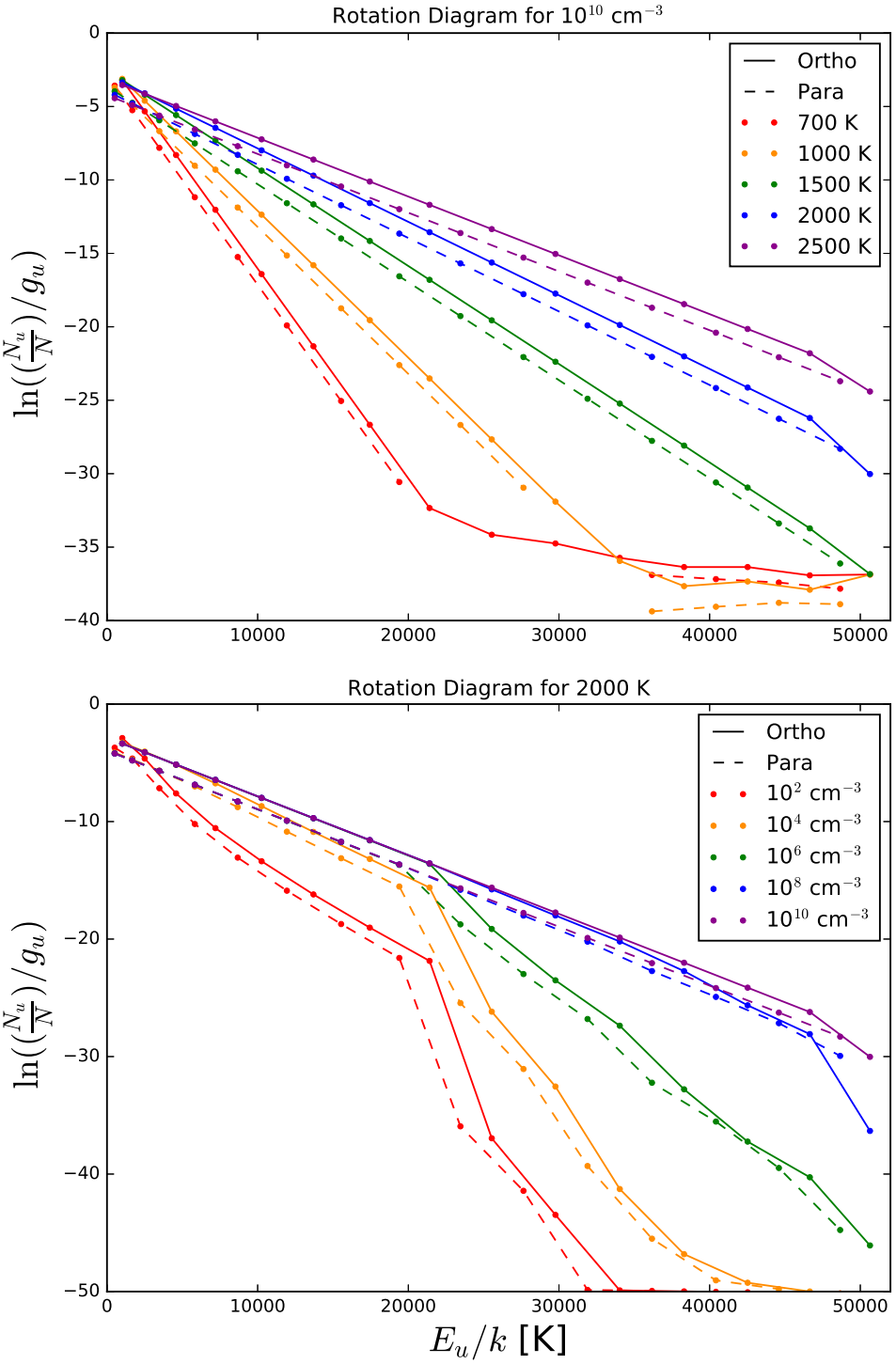

Figure 4.2: Rotation Diagrams for H_2 in the Vibrational Ground State ($v = 0$).

Rotation diagrams for H_2 in the vibrational ground state ($v = 0$), simulated with comprehensive LAMDA data from Table.4.1, with multiple colliders (H_2, H, and He) and high rovibrational transitions. Ortho-H_2 (solid), para-H_2 (dash). Top: variation of level populations with temperature at constant collider density (10^{10} cm^{-3}). A few para-H_2 levels are not shown on the graph, due to low population. Bottom: variation of level populations with density at constant kinetic temperature (2000 K). Note that the degeneracy g_u here does not include the ortho-para ratio.

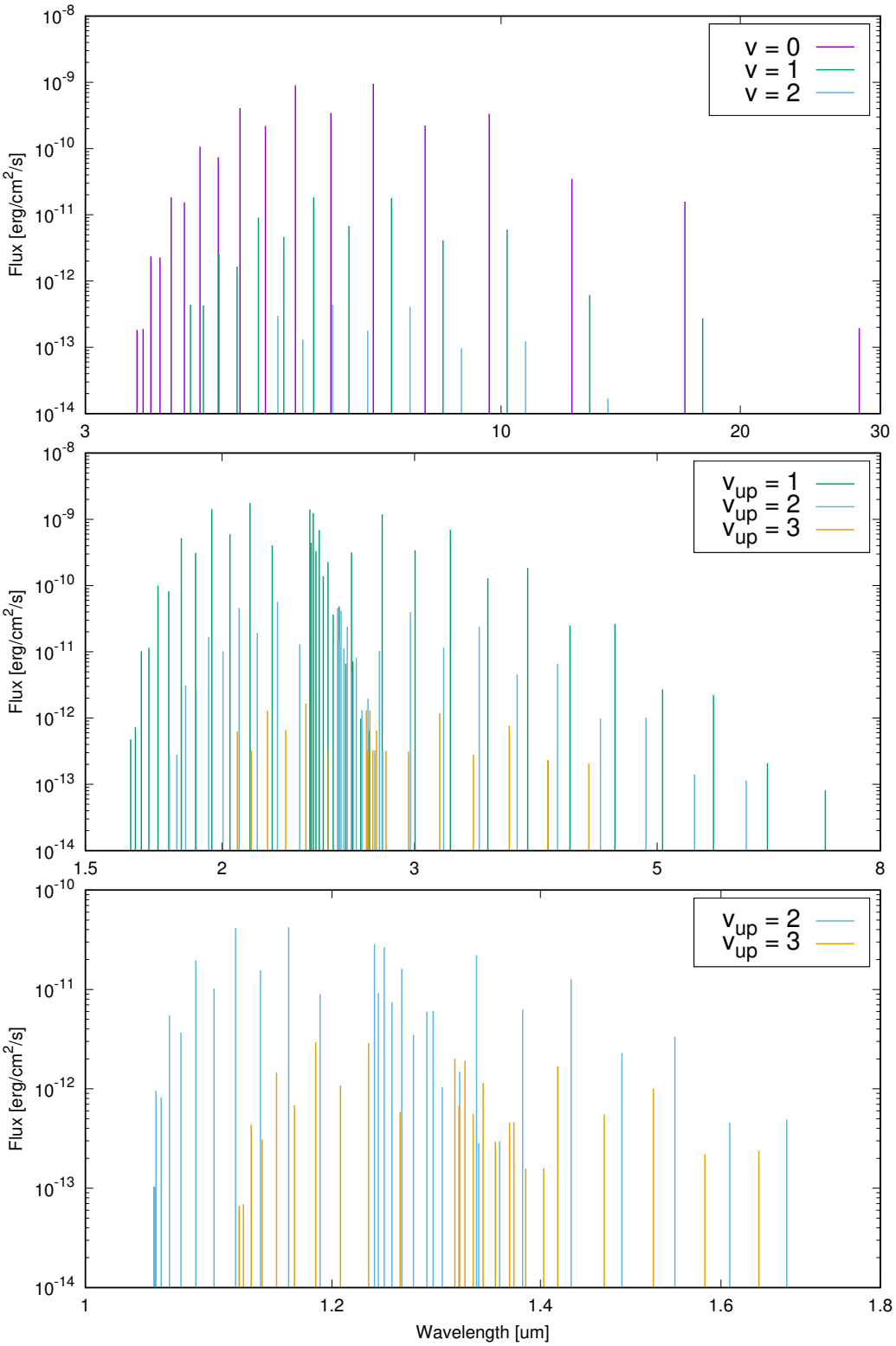

Figure 4.3: Zoomed-in Rovibrational Line Spectra of H_2.

Zoomed-in rovibrational line spectra of H_2 at 1500 K, with multiple colliders (H_2, H, and He) and a total density of 10^8 cm^{-3}. Top: pure rotational transitions, $\Delta v = 0$; middle: vibrational transitions, $\Delta v = 1$; bottom: vibrational transitions, $\Delta v = 2$.

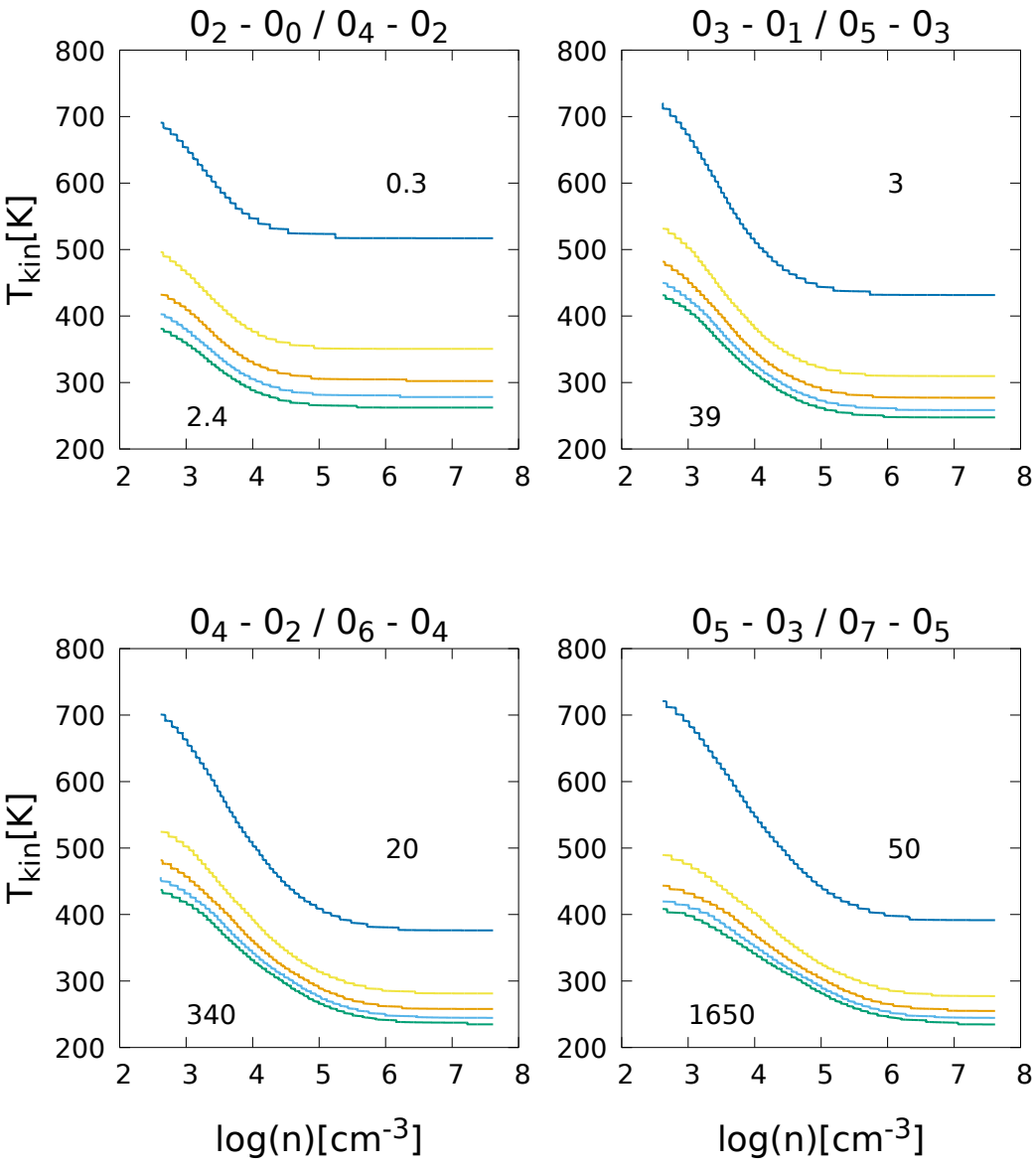

Figure 4.4: H_2 Diagnostic Line Ratios.

H_2 diagnostic line ratios between rotational transitions as a function of density and kinetic temperature. (Notation: v_J.) Line ratios are as labeled with linear spacing.

4.4 H_2 Excitation in PDRs

PDRs produce most of the non-stellar infrared emission in the galaxy and have been an important topic in many fields, e.g., star-formation, CSEs of evolved stars, and PPDs (Hollenbach & Tielens 1999; Kaufman et al. 1999; Williams & Cieza 2011). UV radiation highly excites molecules, resulting in intense infrared emission from such regions. H_2 is one of the primary emitters in the near to mid-infrared in PDRs, with high (both rotational and vibrational) exitation emission (Tielens et al. 1993; Thi et al. 2009; Kaplan 2017).

With the updated high rotational H_2 - H_2 collisional rates, we look into H_2 excitation properties in PDRs with Cloudy (Ferland et al. 2017). Radiative transfer, including collisional de-excitation, radiative pumping, etc, is included to simulate molecular emission and cooling. Detailed treatment of H_2 excitation in Cloudy, including the g-bar approximation, is discussed in Shaw et al. (2005).

4.4.1 PDR Density - Radiation Grid

Cloudy offers test suites related to various astrophysical conditions, including the Leiden PDR benchmark models. We constructed a density - radiation grid based on the PDR conditions that are assumed in such benchmark models (details listed in Table 4.3) with previous and updated rotational H_2 - H_2 rates, to look into these environments regarding H_2 emission.

Figure 4.5 shows representative H_2 rotational emission intensity ratios between models with updated and previous H_2 - H_2 rotational collision rates (Table 1.2 and 4.2). Line emission intensity could be affected as much as $\sim 150\%$ for 0-0 S(2) and 0-0 S(4), and main effects are at lower J transitions ($J < 9$). Higher J energies overlap with vibrationally excited states and rovibrational coupling would suggest a more pronounced effect on vibrationally excited states, though only g-bar approximation rates are available. For a given UV field (10 Draine), dominant effect shifts from 0-0 S(0) to 0-0 S(4) with increasing density. While for a fixed density ($10^{5.5}$ cm^{-3}), dominant effect remains at 0-0 S(2) and grows from $\sim 30\%$ to

$\sim 150\%$ with increasing UV field. These significant changes in H_2 line emission predictions suggest the importance of accurate collision rates in theoretical modelling for general PDR environments, especially with high density and radiation.

Table 4.3: PDR Density - Radiation Grids. [a]

Parameter	Value
n: Density (cm^{-3})	$10^{3.5} - 10^{7.5}$
FUV Field (χ)[b]	$10 - 10^5$
Geometry	semi-infinite (plane - parallel)
T_{gas} T_{grain}	Variable, self - consistent
Abundances (PAH & Elemental)	Leiden PDR [a]
Stopping A_V	10 mag
Turbulence	1 km s^{-1}

[a] For more details, see Röllig et al. (2007) and Ferland et al. (2017)
[b] In units of FUV Draine field, $\chi = 1.71 G_0$, (Draine 1978; Habing 1968).

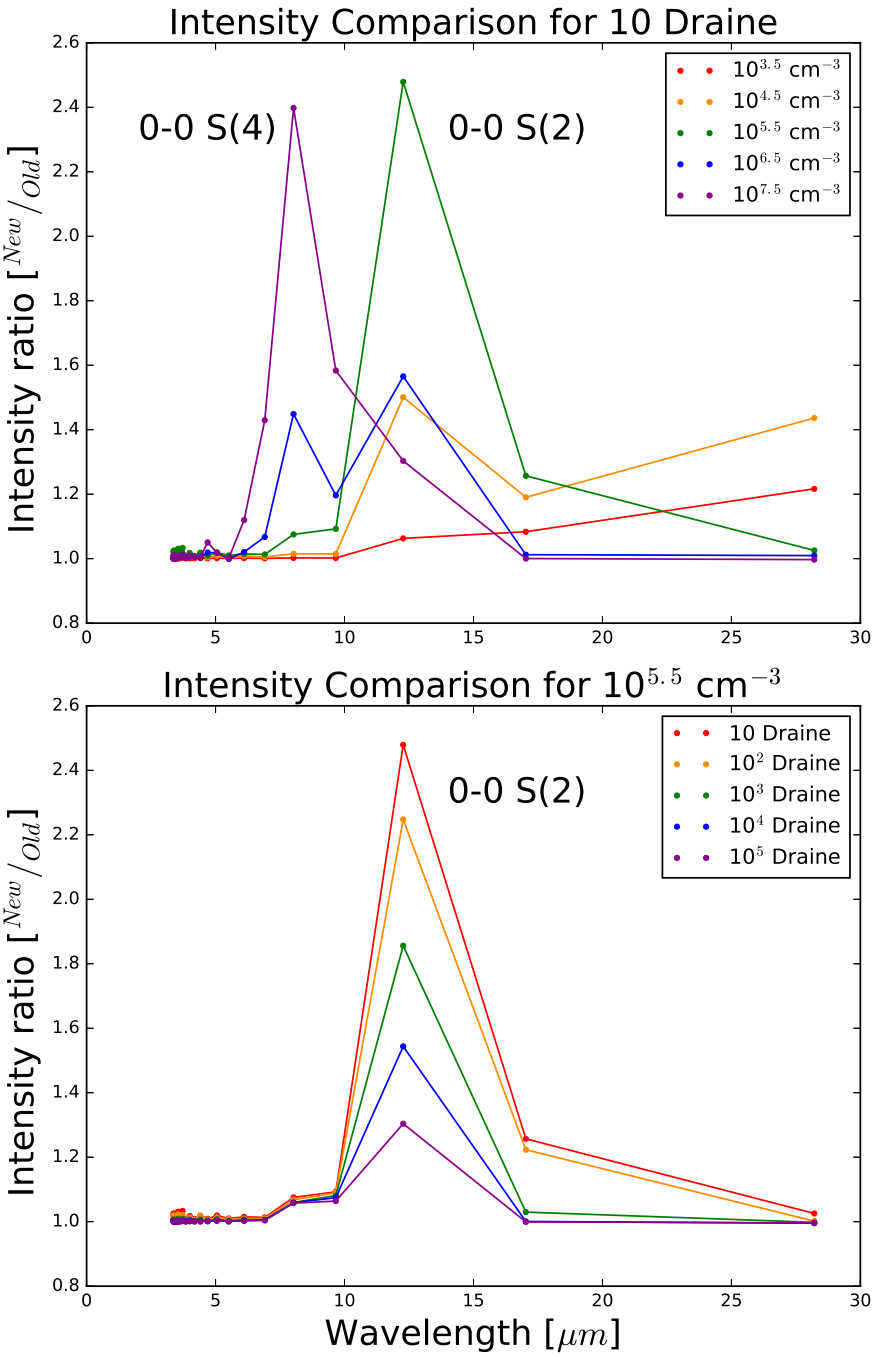

Figure 4.5: The Effect of High Rotational H_2 - H_2 Collision Data Update.

The effect of high rotational H_2 - H_2 collision data update on H_2 rotational emission ($v = 0$) prediction in PDR Density - Radiation Grids (Table 4.3). Top: intensity prediction ratios of models with $\frac{new}{old}$ data at 10 Draine field, densities indicated with colors and highest ratios are marked (0-0 S(2) and 0-0 S(4)). Bottom: intensity prediction ratios of models with $\frac{new}{old}$ data at $10^{5.5}$ cm^{-3}, radiation indicated with colors and highest ratio is marked (0-0 S(2)).

4.4.2 Orion Bar Model

For a more realistic case, we adapt a constant parameter Orion Bar model. Table 4.4 lists the best-fit model parameters from Kaplan et al. (2017), which they deduced from a density - temperature grid. (For more details regarding physical conditions, see Pellegrini et al. (2009); Shaw et al. (2009); Ferland et al. (2017); Kaplan et al. (2017).) The model has been utilized for analyzing the near-infrared spectrum (for vibrational excited H_2, $v = 1 - 10$) and the results are in good agreement with observations. We investigate H_2 excitation and demonstrate the effect of simulated results due to updated collision rates (Table 4.2).

In Figure 4.6, we demonstrate the excitation prediction for the given model. The vibrational ground state shows two temperature components: $\sim$ 380 K for cooler molecular gas and $\sim$ 5200 K closer to the ionization front (excitation temperature, not kinetic temperature) (Goicoechea et al. 2018). Such a rotation diagram with high rovibrational excitation shows strong evidence of radiative pumping.

For vibrationally excited H_2, we compare the simulated level populations with infrared observational data. In general, the model with updated collision data gives under prediction for $v = 1 - 2$ and over prediction for higher excitation levels. Simulated populations using previous and updated collision rates are compared and they present significant differences (as much as a factor of $\sim$ 6). Such substantial changes could considerably influence the interpretations of simulated results (including column density, emission, etc.), hence affecting the evaluation of physical conditions of the gas (in this particular case, gas density and temperature).

Table 4.4: Best-fit Cloudy Model Parameters from Kaplan et al. (2017).

Parameter	Value
Constant Temperature	625 K
Constant Density (n_H)	5×10^3 cm^{-3}
Abundances	Orion[b]
Grains	
Radiation Field	O7V star θ^1 Ori C[a]
Ionizing Photons	
Distance from Cloud	
Turbulence	2 km s^{-1}
Stopping A_V	14 mag
Background Cosmic Flux	Galactic [b]

[a]Parameters from Cloudy models of Orion Bar by Pellegrini et al. (2009); Shaw et al. (2009).
[b]Default in Cloudy, see more in Ferland et al. (2017).

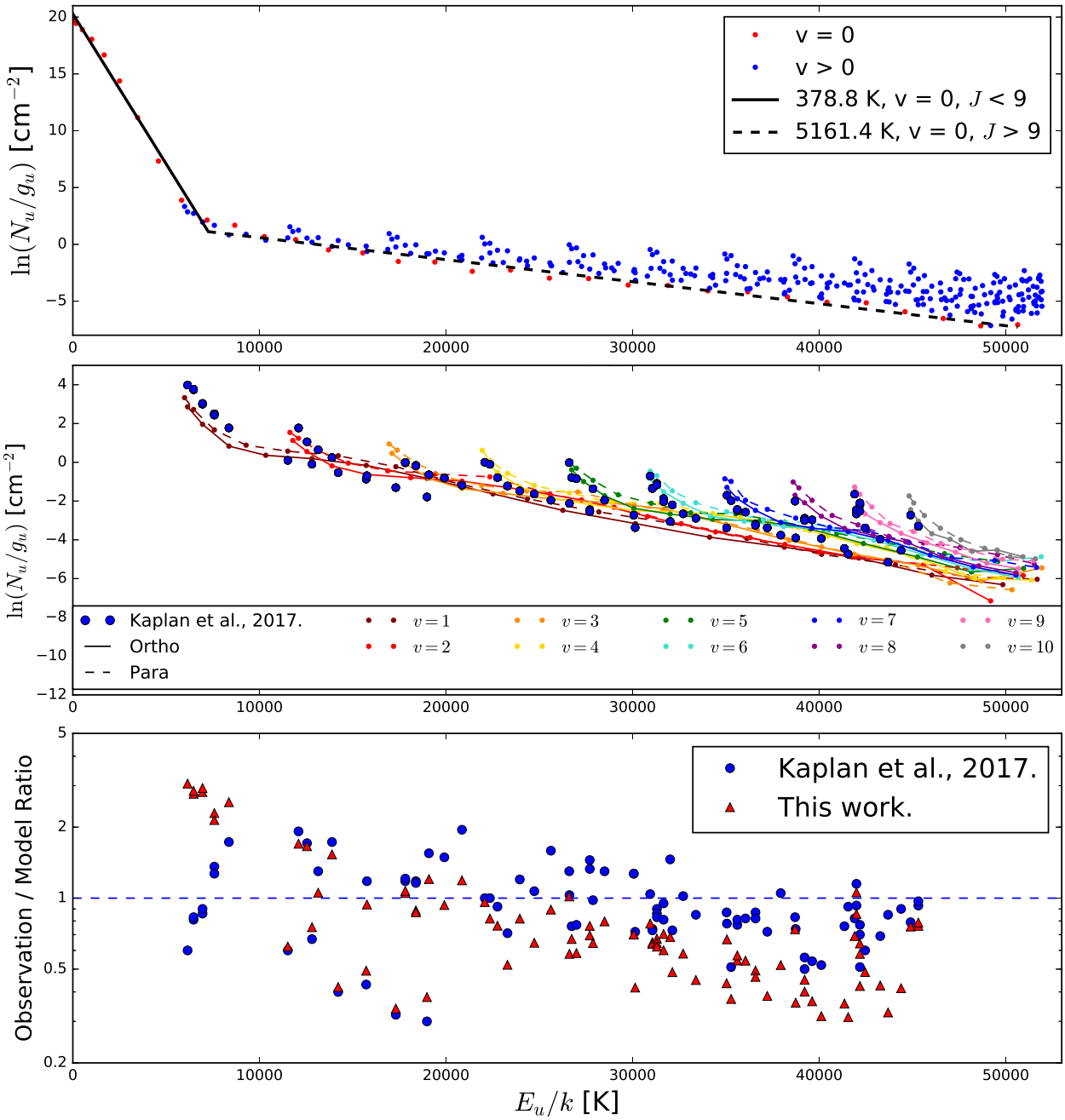

Figure 4.6: Orion Bar Figures.

Top: Rotation diagram for Orion Bar model including v up to 14, $v = 0$ is highlighted with red and fitted with two excitation temperatures. Middle: zoom-in view of H_2 rotation diagram for $v = 1 - 10$, Cloudy model in lines and observation from Kaplan et al. (2017) in blue dots. Bottom: observation/model level population ratio. Original data ($v = 0, J = 0 - 8$ & g-bar approximation from Shaw et al. (2005)) in blue and updated data ($v = 0, J = 0 - 31$ from Wan et al. (2018) & g-bar approximation) in red.

4.5 Summary

We investigate the excitation properties of H_2 in PDR-related environments with NLTE simulations, while applying new high rotational H_2 - H_2 collisional rate coefficient data. Uniform conditions, general PDRs and the Orion Bar are considered and the preliminary results include:

- H_2 collisional rate coefficients data was updated with new high rotational calculations (up to $J = 31$) and applied in NLTE simulations for various astrophysical environments.

- Population diagrams with varied temperature and density suggest high rotational excitations are more sensitive to density, attributed to the high excitation energy for H_2 (i.e., large rotational constant).

- H_2 emission is intense in typical PDR environments and could be utilized as a diagnostic of physical conditions. Rotational line emission ratios are shown as probes for density and temperature.

- In general PDR environments, rotational H_2 emission could be affected by as much as $\sim 150\%$ by updated high rotational collision rates, with the stronger effect in dense and highly-irradiated conditions.

- We examined the effect of the new collisional data in a realistic model of the Orion Bar, which was previously used to fit infrared observations. The influence on excitation prediction of H_2 is substantial and suggests modification of the deduced physical parameters.

- The LAMDA dataset is available at the UGA Molecular Excitation Database[2], and Cloudy data update will be included in the future release of the package.

[2] www.physast.uga.edu/amdbs/excitation/

Chapter 5

Conclusion and Outlook

5.1 Conclusion

Molecules have long provided us valuable information about the physical and chemical conditions of the ISM. In many energetic environments, such as star-forming regions and CSEs, molecules are highly excited both rotationally and vibrationally. In this thesis, we investigate the molecular probes in highly irradiated astrophysical environments with NLTE simulations.

For NLTE simulations, accurate molecular data, such as Einstein A coefficients and collisional rates, are essential. High excitation molecular data were previously unavailable, due to the theoretical or experimental limitations. The demand for these fundamental parameters has been growing in recent decades, due to the rapid developments in infrared observations (e.g., Herschel, Spitzer, SOFIA and the soon-to-be-launched JWST).

Here we focus on three diatomic molecules (SiO, CO and H_2) and constructed comprehensive high excitation collisional rate coefficient data sets, with state-of-the-art theoretical calculations and scaling methods. These data include high rovibrational excitation states and multiple collision partners. For SiO and CO, we updated the collisional rates up to $v = 5$ and $J = 40$, with three colliders: H_2, H, and He. While for H_2, high rotational H_2-H_2 collisional rates (up to $J = 31$) are implemented. Utilizing these data, we are able to study the excitation properties of these molecules in warm environments where molecules are radiatively pumped.

In spectral analysis for single-species homogeneous models, we obtained full molecular line spectra from the infrared to the radio. High excitation emission, both rotational and vibrational, at near- to mid-infrared is intense and comparable to low-lying rotational lines.

Emission intensity evolves with gas properties (such as density and temperature), and approaches LTE in dense and warm environments. Line intensity ratios between different rovibrational states for temperture and density are constructed, offering additional diagnostics of physical conditions.

We analyzed molecular emission and population in typical PDR environments. Molecules are rovibrationally pumped by UV radiation, resulting in intense emission. In PDRs, H_2 is the dominant infrared emitter, CO has been a traditional probe, and SiO is commonly observed in hot regions. Meanwhile, CO and SiO are also the main gas-phase carriers for carbon and silicon. In constant temperature models, molecules show quasi-LTE behaviours (near the given temperatures). While in models with self-consistent temperature profiles (obtained by solving for the thermal balance), population diagrams show multiple components, probing regions from near-source (a few hundred Kelvins) to deeper into the cloud (a few tens of Kelvins). With temperature, density, and radiation grid PDR models, we further investigated molecular excitation and show radiation-related rovibrational line ratios. Overall, molecular level populations are evidently radiatively pumped, presenting strong NLTE effects, and line ratios show versatile diagnostic properties. The effect of the updated H_2 high rotational collisional data is examined in PDR grids and a realistic model of the Orion Bar, the most well-studied PDR. H_2 emission prediction is influenced substantially by the data update. In the tested Orion Bar model, level populations are affected significantly as well, suggesting modification of the deduced physical parameters. Due to its large rotational constant, H_2 shows high rotation temperatures up to ~ 400 K and ~ 5000 K (excitation temperature, not kinetic temperature) in the Orion Bar.

CSEs for AGB stars are complex both in structure and composition. They experience intense stellar radiation and on-going vigorous chemistry, therefore molecules within are highly excited. We constructed detailed NLTE models for CSEs and examined rovibrational molecular excitation with them. For O-rich star VY Canis Majoris, we focus on SiO excitation analysis, while CO analysis is performed for the C-rich star IRC +10216 model. These

models include a self-consistent treatment of gas and dust temperature, chemistry, radiative transfer, dust opacity, etc. A broad range of physical conditions, such as species abundances and dust distribution, are taken into consideration. Modelling results suggest rovibrational levels are exceptionally populated and excited throughout the envelope. Our predicted SED fits previous observations (ISO and Herchel) well and vibrationally excited line emission is identified. Rotation and vibration temperatures are derived with population diagrams and showing near-LTE trends, consistent with the dense and highly-irradiated environments.

The molecular data sets are made available in various formats, including LAMDA and BASECOL, from the UGA Molecular Excitation Database[1] and in future Cloudy releases.

5.2 Outlook

Our simulations show promising applications for future NLTE astrophysical modelling and other related aspects. Working with the frontier knowledge of many fields, we hope to improve theoretical studies of UV-irradiated environments.

The ground-based radio observatories, such as ALMA, has detected rotational transitions of vibrationally excited molecules. While high rovibrational molecular emission observation at near- to mid-infrared has been previously limited. Major improvements in mid-infrared have been made with instruments such as SOFIA-EXES (airborne) and TEXES (ground-based), while JWST is expected to open the near-infrared window. These high resolution observation will continue to enhance our view of energetic environments, hence providing crucial physical and chemical information for astrophysical events of interest. For instance, rovibrationally excited CO (at $2 - 5\mu$m) could be used to probe the rocky inner zone of PPDs at a few AU, where planets are formed.

More detailed and realistic models are needed to reveal the precise structure, composition and micro-processes in these active astrophysical objects. Particularly, in order to better understand the molecular excitation properties in radiatively pumped gas, more advanced

[1] www.physast.uga.edu/amdbs/excitation/

NLTE modelling is required. Accurate and comprehensive molecular excitation data are essential for the reliability for such modelling. Laboratory astrophysicists have been and will continue to study more molecules of interest, assisting the theoretical study of NLTE environments. Inclusive chemical networks and complex molecules, such as PAHs, are also important for building a robust model.

Bibliography

Agúndez, M., Fonfría, J. P., Cernicharo, J., et al. 2012, A&A, 543, A48

Alcolea, J., Bujarrabal, V., Planesas, P., et al. 2013, A&A, 559, A93

Andrews, D. G. 2010, An Introduction to Atmospheric Physics, 2nd edn. (Cambridge University Press)

Ansdell, M., Williams, J. P., Trapman, L., et al. 2018, ArXiv e-prints, arXiv:1803.05923

Arce, H. G., Shepherd, D., Gueth, F., et al. 2007, Protostars and Planets V, 245

Balanca, C., & Dayou, F. 2017, MNRAS, 469, 1673

Barenfeld, S. A., Carpenter, J. M., Sargent, A. I., Isella, A., & Ricci, L. 2017, ArXiv e-prints, arXiv:1711.04045

Barton, E. J., Yurchenko, S. N., & Tennyson, J. 2013, MNRAS, 434, 1469

Beichman, C. A., Neugebauer, G., Habing, H. J., Clegg, P. E., & Chester, T. J., eds. 1988, Infrared astronomical satellite (IRAS) catalogs and atlases. Volume 1: Explanatory supplement, Vol. 1

Beuther, H., Zhang, Q., Greenhill, L. J., et al. 2005, ApJ, 632, 355

Blake, G. A., Sutton, E. C., Masson, C. R., & Phillips, T. G. 1987, ApJ, 315, 621

Bruderer, S., Harsono, Daniel, & van Dishoeck, Ewine F. 2015, A&A, 575, A94

Burton, M. G. 1992, Australian Journal of Physics, 45, 463

Carruthers, G. R. 1970, Space Sci. Rev., 10, 459

Castro, C., Doan, K., Klemka, M., et al. 2017, Molecular Astrophysics, 6, 47

Cecchi-Pestellini, C., Bodo, E., Balakrishnan, N., & Dalgarno, A. 2002, ApJ, 571, 1015

Cernicharo, J., Yamamura, I., González-Alfonso, E., et al. 1999, ApJ, 526, L41

Cernicharo, J., Teyssier, D., Quintana-Lacaci, G., et al. 2014, ApJ, 796, L21

da Silva Santos, J. M., Ramos-Medina, J., Sánchez Contreras, C., & García-Lario, P. 2018, arXiv e-prints, arXiv:1812.07815

Danilovich, T., Teyssier, D., Justtanont, K., et al. 2015, A&A, 581, A60

Dayou, F., & Balanca, C. 2006, A&A, 459, 297

De Beck, E., Decin, L., de Koter, A., et al. 2010, A&A, 523, A18

De Beck, E., Boyer, M. L., Bujarrabal, V., et al. 2019, arXiv e-prints, arXiv:1903.12025

Decin, L. 2012, Advances in Space Research, 50, 843

Decin, L., Justtanont, K., De Beck, E., et al. 2010, A&A, 521, L4

Del Zanna, G., Dere, K. P., Young, P. R., Landi, E., & Mason, H. E. 2015, A&A, 582, A56

Doan, L., Ramstedt, S., Vlemmings, W. H. T., et al. 2017, A&A, 605, A28

Draine, B. T. 1978, ApJ, 36, 595

Dubernet, M. L., Alexander, M. H., Ba, Y. A., et al. 2013, A&A, 553, A50

Enokiya, R., Sano, H., Hayashi, K., et al. 2017, ArXiv e-prints, arXiv:1711.00722

Evans, Neal J., I. 1999, ARA&A, 37, 311

Ferland, G. J., Chatzikos, M., Guzmán, F., et al. 2017, Rev. Mexicana Astron. Astrofis., 53, 385

Field, G. B., Somerville, W. B., & Dressler, K. 1966, Annual Review of Astronomy and Astrophysics, 4, 207

Flower, D. 2007, Molecular Collisions in the Interstellar Medium, 2nd edn., Cambridge Astrophysics (Cambridge University Press)

Fonfría, Fernández-López, M., Pardo, J. R., et al. 2018a, ApJ, 860, 162

Fonfría, J. P., Agúndez, M., Cernicharo, J., Richter, M. J., & Lacy, J. H. 2018b, ApJ, 852, 80

Fonfría, J. P., Cernicharo, J., Richter, M. J., & Lacy, J. H. 2008, ApJ, 673, 445

Fonfría, J. P., Hinkle, K. H., Cernicharo, J., et al. 2017, ApJ, 835, 196

Gerlich, D. 1990, J. Chem. Phys., 92, 2377

Glassgold, A. E., Mamon, G. A., & Huggins, P. J. 1989, ApJ, 336, L29

Gobrecht, D., Cherchneff, I., Sarangi, A., Plane, J. M. C., & Bromley, S. T. 2016, A&A, 585, A6

Goicoechea, J. R., Cuadrado, S., Pety, J., et al. 2018, in IAU Symposium, Vol. 332, IAU Symposium, ed. M. Cunningham, T. Millar, & Y. Aikawa, 210–217

Goldsmith, P. F., & Langer, W. D. 1999, ApJ, 517, 209

González-Alfonso, E., Wright, C. M., Cernicharo, J., et al. 2002, A&A, 386, 1074

Gueth, F., Guilloteau, S., & Bachiller, R. 1998, A&A, 333, 287

Habing, H. J. 1968, Bull. Astron. Inst. Netherlands, 19, 421

Harsono, D., Visser, R., Bruderer, S., van Dishoeck, E. F., & Kristensen, L. E. 2013, A&A, 555, A45

Herbst, E., Millar, T. J., Wlodek, S., & Bohme, D. K. 1989, A&A, 222, 205

Höfner, S., & Olofsson, H. 2018, The Astronomy and Astrophysics Review, 26, 1

Hollenbach, D. J., & Tielens, A. G. G. M. 1997, ARA&A, 35, 179

Hollenbach, D. J., & Tielens, A. G. G. M. 1999, Rev. Mod. Phys., 71, 173

Hony, S., Waters, L. B. F. M., & Tielens, A. G. G. M. 2002, A&A, 390, 533

Jimeno, e. a. 1999, J. Chem. Phys., 111, 4966

Justtanont, K., Khouri, T., Maercker, M., et al. 2012, A&A, 537, A144

Kamp, I., Antonellini, S., Carmona, A., Ilee, J., & Rab, C. 2018, in The Cosmic Wheel and the Legacy of the AKARI Archive: From Galaxies and Stars to Planets and Life, ed. T. Ootsubo, I. Yamamura, K. Murata, & T. Onaka, 89–96

Kamp, I., Woitke, P., Pinte, C., et al. 2011, A&A, 532, A85

Kaplan, K. F. 2017, PhD thesis, The University of Texas at Austin

Kaplan, K. F., Dinerstein, H. L., Oh, H., et al. 2017, ApJ, 838, 152

Karska, A., Kaufman, M. J., Kristensen, L. E., & van Dishoeck, E. F. 2017, ArXiv e-prints, arXiv:1711.02858

Kaufman, M. J., Wolfire, M. G., Hollenbach, D. J., & Luhman, M. L. 1999, ApJ, 527, 795

Kervella, P., Decin, Leen, Richards, Anita M. S., et al. 2018, A&A, 609, A67

Khouri, T., Vlemmings, W. H. T., Olofsson, H., et al. 2018, A&A, 620, A75

Khouri, T., Vlemmings, W. H. T., Ramstedt, S., et al. 2016, MNRAS, 463, L74

Langer, W. D., & Glassgold, A. E. 1990, ApJ, 352, 123

Leão, I. C., de Laverny, P., Mékarnia, D., de Medeiros, J. R., & Vandame, B. 2006, A&A, 455, 187

Lee, T.-G. 2007, in Prep.

Lee, T.-G., Balakrishnan, N., Forrey, R. C., et al. 2008, ApJ, 689, 1105

Lepp, S., Stancil, P. C., & Dalgarno, A. 2002, Journal of Physics B: Atomic, Molecular and Optical Physics, 35, R57

Leurini, S., Codella, C., Gusdorf, A., et al. 2013, A&A, 554, A35

Li, X., Millar, Tom J., Walsh, Catherine, Heays, Alan N., & van Dishoeck, Ewine F. 2014, A&A, 568, A111

Lique, F. 2015, MNRAS, 453, 810

López-Sepulcre, A., Watanabe, Y., Sakai, N., et al. 2016, ApJ, 822, 85

Lykins, M. L., Ferland, G. J., Kisielius, R., et al. 2015, ApJ, 807, 118

Lyo, A.-R., Kim, J., Lee, J.-J., et al. 2017, ApJ, 844, 4

Martin, P. G., & Rouleau, F. 1991, in Extreme Ultraviolet Astronomy, ed. R. F. Malina & S. Bowyer, 341

Matsuura, M., Yates, J. A., Barlow, M. J., et al. 2013, MNRAS, 437, 532

McKee, C. F., & Ostriker, E. C. 2007, ARA&A, 45, 565

Messenger, S. J., Speck, A., & Volk, K. 2013, ApJ, 764, 142

Millar, T. J. 2016, in Journal of Physics Conference Series, Vol. 728, Journal of Physics Conference Series, 052001

Molyarova, T., Akimkin, V., Semenov, D., et al. 2017, ApJ, 849, 130

Neufeld, D. A. 2012, ApJ, 749, 125

Nguyen-Lu'o'ng, Q., Motte, F., Carlhoff, P., et al. 2013, ApJ, 775, 88

Nisini, B., Codella, C., Giannini, T., et al. 2007, A&A, 462, 163

O'dell, C. R. 2001, ARA&A, 39, 99

Onaka, T., Mori, T., Sakon, I., & Ardaseva, A. 2016, ApJ, 829, 106

Palov, A. P., Gray, M. D., Field, D., & Balint-Kurti, G. G. 2006, , 639, 204

Palov, A. P., Jimeno, P., Gray, M. D., Field, D., & Balint-Kurti, G. G. 2002, J. Chem. Phys., 116, 1388

Patel, N. A., Young, K. H., Brünken, S., et al. 2009, ApJ, 691, L55

Pellegrini, E. W., Baldwin, J. A., Ferland, G. J., Shaw, G., & Heathcote, S. 2009, ApJ, 693, 285

Polehampton, E. T., Menten, K. M., van der Tak, F. F. S., & White, G. J. 2010, A&A, 510, A80

Ramos-Medina, J., Sánchez Contreras, C., García-Lario, P., & da Silva Santos, J. M. 2018, A&A, 618, A171

Richter, L., Kemball, A., & Jonas, J. 2013, MNRAS, 436, 1708

—. 2016, MNRAS, 461, 2309

Röllig, M., Abel, N. P., Bell, T., et al. 2007, A&A, 467, 187

Rybicki, G. B., & Lightman, A. P. 1979, Radiative processes in astrophysics

Schilke, P., Pineau des Forêts, G., Walmsley, C. M., & Martín-Pintado, J. 2001, A&A, 372, 291

Schöier, F. L., van der Tak, F. F. S., van Dishoeck, E. F., & Black, J. H. 2005, A&A, 432, 369

Schwarz, K. R., Bergin, E. A., Cleeves, L. I., et al. 2018, ApJ, 856, 85

Shang, H., Li, Z.-Y., & Hirano, N. 2007, Protostars and Planets V, 261

Shaw, G., Ferland, G. J., Abel, N. P., Stancil, P. C., & van Hoof, P. A. M. 2005, ApJ, 624, 794

Shaw, G., Ferland, G. J., Henney, W. J., et al. 2009, ApJ, 701, 677

Shenoy, D. P., Jones, T. J., Humphreys, R. M., et al. 2013, AJ, 146, 90

Shull, J. M., & Beckwith, S. 1982, Annual Review of Astronomy and Astrophysics, 20, 163

Sloan, G. C., Kraemer, K. E., Price, S. D., & Shipman, R. F. 2003, ApJS, 147, 379

Song, L., Balakrishnan, N., Walker, K. M., et al. 2015, ApJ, 813, 96

Sternberg, A., & Dalgarno, A. 1995, ApJS, 99, 565

Tan, J. C., Beltrán, M. T., Caselli, P., et al. 2014, Protostars and Planets VI, 149

Thi, W. F., Kamp, I., Woitke, P., et al. 2013, A&A, 551, A49

Thi, W. F., van Dishoeck, E. F., Bell, T., Viti, S., & Black, J. 2009, MNRAS, 400, 622

Tielens, A. G. G. M. 2005, The Physics and Chemistry of the Interstellar Medium

Tielens, A. G. G. M. 2013, Rev. Mod. Phys., 85, 1021

Tielens, A. G. G. M., Meixner, M. M., van der Werf, P. P., et al. 1993, Science, 262, 86

Tiwari, M., Menten, K. M., Wyrowski, F., et al. 2018, ArXiv e-prints, arXiv:1803.10164

Turner, E. B., Chan, K.-W., Green, S., & Lubowich, A. D. 1992, 399, 114

Van de Sande, M., Decin, L., Lombaert, R., et al. 2017, ArXiv e-prints, arXiv:1708.09190

Van de Sande, M., Decin, L., Lombaert, R., et al. 2015, in EAS Publications Series, Vol. 71, EAS Publications Series, 255–257

van der Tak, F. F. S., Black, J. H., Schöier, F. L., Jansen, D. J., & van Dishoeck, E. F. 2007, A&A, 468, 627

van Dishoeck, E. F. 2017, ArXiv e-prints, arXiv:1710.05940

van Dishoeck, E. F., & Blake, G. A. 1998, ARA&A, 36, 317

Van Hoof, P. A. M., Weingartner, J. C., Martin, P. G., Volk, K., & Ferland, G. J. 2004, MNRAS, 350, 1330

van Regemorter, H. 1962, ApJ, 136, 906

Vlemmings, W., Khouri, T., O'Gorman, E., et al. 2017, ArXiv e-prints, arXiv:1711.01153

Walker, K. M., B. H. Yang, & P. C. Stancil. 2014, ApJ, 790,96

Walker, K. M., Song, L., Yang, B. H., et al. 2015, ApJ, 811, 27

Wan, Y., Yang, B. H., Stancil, P. C., et al. 2018, The Astrophysical Journal, 862, 132

Williams, J. P., & Cieza, L. A. 2011, Annual Review of Astronomy and Astrophysics, 49, 67

Wilson, R. W., Penzias, A. A., Jefferts, K. B., Kutner, M., & Thaddeus, P. 1971, ApJ, 167, L97

Wittkowski, M., Hauschildt, P. H., Arroyo-Torres, B., & Marcaide, J. M. 2012, A&A, 540, L12

Wong, K. T., Kamiński, T., Menten, K. M., & Wyrowski, F. 2016, A&A, 590, A127

Yang, B., Stancil, P. C., Balakrishnan, N., & Forrey, R. C. 2010, ApJ, 718, 1062

Yang, B., Zhang, P., Wang, X., et al. 2015, Nature Communications, 6, 6629

Yang, B., Zhang, P., Qu, C., et al. 2018, The Journal of Physical Chemistry A, 122, 1511

Yang, X., Chen, Peisheng, & He, Jinhua. 2004, A&A, 414, 1049

Zhang, Z. E., Cumbee, R. S., Stancil, P. C., & Ferland, G. J. 2018, Molecular Astrophysics, 13, 6

Ziurys, L. M., Friberg, P., & Irvine, W. M. 1989, ApJ, 343, 201